Dissertation
submitted to the
Combined Faculties for Natural Sciences and for Mathematics
of the Ruperto-Carola University of Heidelberg, Germany
for the degree of
Doctor of Natural Sciences

presented by

**Dipl.-Phys. Johannes Haller**
born in Münster, Germany

Oral examination: December 3rd, 2003

# Search for Squark Production in R-Parity Violating Supersymmetry at HERA

Referees: Prof. Dr. Peter Schleper
Prof. Dr. Karlheinz Meier

# Zusammenfassung

**Suche nach Squark Produktion in R-Paritätsverletzender Supersymmetry bei HERA**
In dieser Arbeit wird eine Suche nach Squarks in supersymmetrischen Modellen mit $R$-Paritätsverletzung vorgestellt. Es werden Daten von $e^{\pm}p$ Kollisionen bei HERA untersucht, die vom H1 Detektor bei einer Schwerpunktsenergie von 320 GeV aufgenommen wurden. Diese Daten entsprechen einer integrierten Luminosität von 64.3 $\mathrm{pb}^{-1}$ für $e^{+}p$ Kollisionen und 13.5 $\mathrm{pb}^{-1}$ für $e^{-}p$ Kollisionen. In der Analyse werden $R$-paritätsverletzende und $R$-paritätserhaltende Zerfälle von Squarks aller 6 Flavours berücksichtigt, die über eine $R$-paritätsverletzende Yukawa–Wechselwirkung resonant erzeugt werden. In keinem Zerfallskanal wurde eine signifikante Abweichung vom Standard Modell gefunden. Es werden Ausschlussgrenzen an das minimale Supersymmetrische Standard Modell und an das minimale Supergravity Modell ermittelt. Für einen großen Bereich des supersymmetrischen Parameterraumes können Squark–Massen unter 275 GeV ausgeschlossen werden, wenn die Stärke der Yukawa–Wechselwirkung gleich der elektroschwachen Wechselwirkung gesetzt wird.

# Abstract

**Search for Squark Production in R-Parity Violating Supersymmetry at HERA**
This thesis describes a search for squarks in supersymmetric models which allow $R$-parity violation. Electron-proton and positron-proton collisions taken at a centre of mass energy of 320 GeV have been investigated using the H1 detector at HERA. The data correspond to an integrated luminosity of 64.3 $\mathrm{pb}^{-1}$ for $e^{+}p$ collisions and 13.5 $\mathrm{pb}^{-1}$ for $e^{-}p$ collisions. The resonant production of squarks of all 6 flavours via a $R$-parity violating Yukawa coupling $\lambda'$ has been considered, taking into account $R$-parity violating and conserving decays of squarks. No significant deviation from the Standard Model has been found in any of the squark decay topologies investigated. The results are interpreted in terms of exclusion limits within the Minimal Supersymmetric Standard Model and the Minimal Supergravity Model. Squark masses below 275 GeV are excluded at 95 % confidence level in a large part of the supersymmetric parameter space for a Yukawa coupling of electromagnetic strength.

*For my parents and my grandmother*

# Table of Contents

# Chapter 1

# Introduction

The Standard Model (SM) of particle physics [1] is a theoretical framework which describes the elementary particles and their weak, electromagnetic and strong interactions. Although this model describes up to now all experimentally measured processes extremely successfully it is believed to be an effective theory of a more fundamental theory since the gravitational interaction is not included. Among the various extensions of the SM, Supersymmetry (SUSY) [2, 3] seems most promising. This symmetry establishes a very fundamental connection between bosons and fermions by predicting new supersymmetric partners to all SM particles. The discovery of such particles would be the first experimental evidence of supersymmetry and would completely change our understanding of nature. Despite numerous searches for these new particles for 20 years, they have not been discovered so far – most likely because they are very heavy. This thesis presents a search for squarks, the supersymmetric partners of quarks, in particular supersymmetric models where the violation of $R$-parity ($\not{R}_p$) is allowed. $R_p$ is an important quantum number in supersymmetric models as it ensures conservation of lepton and baryon number.

Although the most general supersymmetric theory is $R_p$ violating, the bigger part of searches for supersymmetric particles at colliders of highest energy are carried out under the assumption that $R_p$ is conserved. In these searches no significant deviation from the SM has been observed, but lower limits on the mass of supersymmetric particles have been set. The most stringent limits have been derived by experiments at LEP and TeVatron. At the present time, there is little room for SUSY particles lighter than the mass of the $Z^0$ boson. For a review of the results in $R_p$ conserving models see [4].

The mounting evidence for neutrino masses and mixing [5, 6] motivates lepton number violation, making $\not{R}_p$ models even more interesting [7]. Furthermore the violation of $R$-parity opens the interesting possibility to resonantly produce supersymmetric particles at particle colliders. For instance, squarks could be produced in collisions of quarks and electrons or positrons [8]. Since protons and electrons or positrons are its colliding particles, the HERA collider at DESY is ideally suited to look for squarks produced in $\not{R}_p$ SUSY.

In this thesis data of $e^+p$ and $e^-p$ collisions taken with the H1 detector at a centre of mass energy of $\sqrt{s} = 320\,\mathrm{GeV}$ have been analysed. The two data sets correspond to an integrated luminosity of $64.3\,\mathrm{pb}^{-1}$ and $13.5\,\mathrm{pb}^{-1}$ respectively, and allow one to search for all six squark flavours with masses up to $\sqrt{s}$. In $e^+p$ collisions the scalar partners of $u$, $c$ and $t$ can be dominantly produced whereas in $e^-p$ collisions the partners of $d$, $s$ and

$b$ are accessible. $R\!\!\!/_p$ leads to a large variety of decay modes for squarks involving several intermediate supersymmetric particles. In this work eight (nine) final state topologies are studied in $e^+p$ ($e^-p$) collisions. Preliminary results of the present search have been reported in [9].

The analysis presented here extends the direct searches for $R\!\!\!/_p$ squark production in $e^+p$ and $e^-p$ collisions previously performed by H1 [10, 11] at $\sqrt{s} \approx 300\,\text{GeV}$. The integrated luminosity for $e^-p$ and $e^+p$ collisions was increased by factors of 30 and 2, respectively. The increase in $\sqrt{s}$ leads to a drastic improvement of the exclusion limits particularly in the high squark mass domain – a completely new kinematic regime has been opened. The direct results from HERA compete with indirect searches at low-energy experiments like neutrino-less double-beta decay [12], atomic parity violation [13] and charged current universality. For a review see [14]. The stringent direct limits on squark production from LEP and TeVatron obtained under the assumption of $R$-parity conservation do not hold in $R\!\!\!/_p$ models. Searches at LEP and TeVatron in $R\!\!\!/_p$ SUSY allow the testing of identical models as presented in this work [15, 16].

This thesis is organised as follows:

- Chap. 2 gives a short overview of the SM and the SM physics in $ep$ collisions. The basic concepts of supersymmetric extensions are introduced focussing on the phenomenology of resonant squark production in $ep$ collisions. The chapter concludes with a discussion of the search strategy of this analysis.

- In Chap. 3 an overview of the experimental setup is given: the HERA collider at DESY and the H1 detector are described.

- Chap. 4 explains preparatory steps of the data analysis. The description of a general data selection ensuring good data quality is followed by an explanation of the identification procedures for charged leptons and hadronic jets in the H1 detector.

- In Chap. 5 the results for the directly $R\!\!\!/_p$ squark decays leading to lepton–quark final states ($eq$ or $\nu q$) are presented.

- Chap. 6 describes the results for the gauge decays of squarks leading to final states containing an electron or positron and multiple jets.

- Chap. 7 gives the results for the gauge decay modes of squarks resulting in final states with a neutrino and multiple jets.

- In Chap. 8 the results of the selection are summarised and the method for calculating exclusion limits is introduced. The resulting exclusion limits are presented for various supersymmetric scenarios in the phenomenological MSSM and the minimal Supergravity model.

- Chap. 9 gives an summary of the results and an outlook.

# Chapter 2

# Theoretical Overview

In this chapter the current understanding in the field of particle physics is summarised by a very brief review of the Standard Model (for details see [17]). The basic interactions and fields of the SM are introduced. After an overview of the most important SM processes relevant in *ep* collisions, the problems and insufficiencies of the SM are discussed. Supersymmetric extensions of the SM, which give very elegant solutions to many of these problems, are presented. Since *ep* collisions are perfectly suited to look for supersymmetric models with $R$-parity violation, the phenomenology of these models are discussed and the possible experimental signatures of squark production via a $R_p$-violating Yukawa coupling $\lambda'$ in *ep* collisions are summarised. In a separate section the search strategy of this analysis is explained. The chapter concludes with the description of the Monte Carlo (MC) simulation of SM background processes and the SUSY signal.

## 2.1 Basic elements of the Standard Model

The SM describes the electromagnetic, weak and strong interactions of elementary particles. It is based on the gauge principle, according to which forces are mediated by the exchange of gauge fields of the corresponding local symmetry group. The symmetry group of the SM is

$$SU(3)_C \times SU(2)_L \times U(1)_Y, \tag{2.1}$$

where $C$ denotes colour, $Y$ denotes the weak hypercharge and $L$ indicates that the weak isospin current couples to left-handed fermions only.

The field content of the SM consists of three parts:

- the fermion sector – spin 1/2 particles describing matter;
- the gauge boson sector – vector particles describing the interactions;
- the Higgs sector – scalars introducing mass terms in the Langrangian by spontaneous symmetry breaking.

The SM **fermions** belong to the fundamental representation of the gauge group of Eq. 2.1. They are believed to be quarks and leptons (charged leptons and neutrinos) of

| fermions | | | $T$ | $T_3$ | $Y$ | $Q$ |
|---|---|---|---|---|---|---|
| $\nu_{eL}$ | $\nu_{\mu L}$ | $\nu_{\tau L}$ | $1/2$ | $1/2$ | $-1/2$ | $0$ |
| $e_L$ | $\mu_L$ | $\tau_L$ | $1/2$ | $-1/2$ | $-1/2$ | $-1$ |
| $e_R$ | $\mu_R$ | $\tau_R$ | $0$ | $0$ | $-1$ | $-1$ |
| $u_L$ | $c_L$ | $t_L$ | $1/2$ | $1/2$ | $1/6$ | $2/3$ |
| $d'_L$ | $s'_L$ | $b'_L$ | $1/2$ | $-1/2$ | $1/6$ | $-1/3$ |
| $u_R$ | $c_R$ | $t_R$ | $0$ | $0$ | $2/3$ | $2/3$ |
| $d_R$ | $s_R$ | $b_R$ | $0$ | $0$ | $-1/3$ | $-1/3$ |

TABLE 2.1: SM fermions and their quantum numbers. $T$ and $T_3$ denote the weak isospin and its third component respectively; $Y$ is the weak hypercharge; $Q$ is the electric charge of the fermion given by $Q = T_3 + \frac{Y}{2}$.

three generations. Since the weak interaction violates parity, the SM is left-right asymmetric. Left-handed and right-handed fermions have different quantum numbers and the left- and right-handed components of the fermion fields are treated differently in the theory: the left-handed components are arranged in weak isodoublets whereas the right-handed fermions are singlets. The fermion fields in the SM are summarised in Tab. 2.1. Assuming massless neutrinos they only have a left-handed representation. The mass eigenstates of the quarks $(d, s, b)$ are not identical to the quark eigenstates of the weak interaction $(d', s', b')$. The latter are linear combinations of the former:

$$\begin{pmatrix} d' \\ s' \\ b' \end{pmatrix} = V_{CKM} \begin{pmatrix} d \\ s \\ b \end{pmatrix} . \tag{2.2}$$

The unitary matrix $V_{CKM}$ can be parameterised by four parameters: three mixing angles and one $CP$-violating phase. By convention, the quarks with electric charge $2/3$ are not subject to mixing. A similar prescription can be used to describe $\nu$ mixing.

The **gauge bosons** belong to the adjoint representation of the SM gauge group. For $SU(3)_C$ there are eight massless gluons $g^i_\mu$ with $i = 1 \dots 8$, for $SU(2)_L$ we have three massive intermediate weak bosons $W^\pm_\mu, W^0_\mu$ and for $U(1)_Y$ the boson $B_\mu$. The forces of the SM are described by the exchange of these gauge bosons between the matter particles with coupling constants $g$, $g'$ and $g_s$. After breaking the SM symmetry for mass generation (see below) the electromagnetic coupling constant and the weak coupling constant are related by

$$g \sin\theta_W = g' \cos\theta_W, \tag{2.3}$$

where $\theta_W$ is the Weinberg angle, a free parameter of the theory, which has been determined experimentally [4] to $\sin^2\theta_W(M_Z) = 0.23113(15)$. The two neutral fields $W^0_\mu$ and $B_\mu$ mix to form the physical states (mass eigenstates) $\gamma$ and $Z^0$.

Thus, the gauge field content of the SM is:

- the massless photon $\gamma$ for the electromagnetic interaction;
- the heavy bosons $W^\pm, Z^0$ for the weak interaction;

| bosons | J | Q | mass (GeV) |
|---|---|---|---|
| gluons $g_i$ $(i = 1..8)$ | 1 | 0 | 0 |
| photon $\gamma$ | 1 | 0 | 0 |
| $W^{\pm}$ | 1 | $\pm 1$ | 80.45 |
| $Z^0$ | 1 | 0 | 91.18 |
| Higgs $H^0$ | 0 | 0 | $> 114.4$ |

Table 2.2: SM bosons and their properties. $J$ denotes the spin and $Q$ the electric charge of the particle. For the Higgs mass the 95 % CL lower limit of the direct search is given [18].

- eight massless gluons $g_\mu^i$ for the strong interaction.

The last remaining sector of the SM is the **Higgs sector**. If the symmetry of the SM were exact, the masses of the fermions and bosons would be zero since mass terms are not invariant under $SU(2)_L$. In the minimal version of the SM one complex $SU(2)$ doublet of scalar Higgs fields $(\Phi^+, \Phi^0)$ (four states) is introduced in order to give masses to quarks, leptons and intermediate weak gauge bosons. In the Lagrangian the additional term

$$V(\Phi) = \mu^2 \Phi^\dagger \Phi + \lambda(\Phi^\dagger \Phi)^2, \qquad \text{with} \quad \lambda > 0 \quad \text{and} \quad \mu^2 < 0 \tag{2.4}$$

is introduced, which leads to a non-vanishing vacuum expectation value of $v = \sqrt{-\mu^2/\lambda}$.

Breaking $SU(2)$ by a particular choice of the vacuum, which retains a massless photon, leads to only one massive neutral boson $H^0$ with spin 0 which couples to the weak gauge bosons and to fermions with coupling strength proportional to their masses. The weak gauge fields have "eaten up" the three appearing massless Goldstone bosons. The four scalar degrees of freedom (4 states) become the longitudinal polarizations of the massive vector bosons $(W^\pm, Z^0)$ and the mass of the new Higgs field. The masses of the $W^\pm$ and the $Z^0$ are related at tree-level by

$$\sin^2 \theta_W = 1 - M_{W^\pm}^2 / M_{Z^0}^2. \tag{2.5}$$

The photon remains massless.

The mass of the Higgs boson $m_H = 2\lambda v^2$ is a free parameter of the SM. It is the only particle in the SM which is not yet directly discovered in any experiment. A direct search has given a 95 % CL lower limit on the Higgs mass of 114.4 GeV [18]. An indirect upper limit is given by precision measurements in the electroweak sector: $M_H \leq 204\,\text{GeV}$ [4]. The quantum numbers and masses of the bosons in the SM are summarised in Tab. 2.2.

## 2.2 Standard Model processes in *ep* collisions

In this analysis data from the electron-proton collider HERA at DESY are investigated[1]. For this reason an overview of the most important SM processes in *ep* collisions is given in the following.

In electron–proton scattering the beam electron interacts with a parton from the proton by the exchange of a gauge boson. The process is called *Deep Inelastic Scattering* (DIS)

[1] In the following the term *electron* will be used for both electron and positron unless explicitly stated.

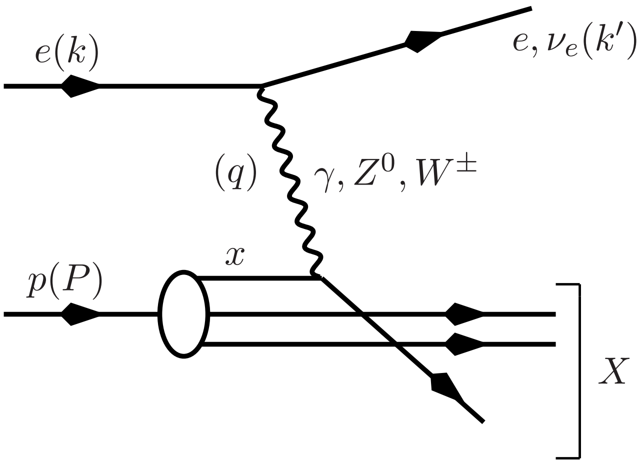


FIGURE 2.1: Feynman diagram for Deep Inelastic Scattering (DIS).

if the gauge boson has a virtuality large enough to resolve the substructure of the proton. In neutral current (NC) DIS a $\gamma$ or $Z^0$ boson is exchanged. In case of charged current (CC) DIS a $W^\pm$ is exchanged, which leads to an electron–neutrino in the final state. The corresponding Feynman diagram is shown in Fig. 2.1. If a photon is exchanged which is almost real or on mass shell, the process is usually referred to as *photoproduction* ($\gamma p$).

### Kinematic variables

The cross sections in *ep* scattering are defined in terms of Lorentz invariant variables which ensure a convenient comparison of the measurements for different experimental setups. If the four-momenta of the incident and outgoing lepton are denoted $k$ and $k'$ and $q$ is the four-vector of the exchanged boson, the negative squared momentum of the exchanged boson is given by

$$Q^2 = -q^2 = (k - k')^2. \tag{2.6}$$

This quantity is Lorentz-invariant and corresponds to the *virtuality* of the exchanged gauge boson. Following the Heisenberg uncertainty relation, $Q^2$ also represents the spatial resolving power of the interaction[2]. The size of the proton is of the order of $10^{-15}$ m, which corresponds to $Q^2 \approx 200\,\mathrm{MeV}^2$. For larger values of $Q^2$ the substructure of the proton is resolved leading to DIS. In contrast lower values lead to $\gamma p$ events.

It is convenient to introduce the two Bjorken scaling variables $x$ and $y$:

$$x = \frac{Q^2}{2Pq} \tag{2.7}$$

$$y = \frac{Pq}{Pk}, \tag{2.8}$$

[2]In this work we always set $\hbar = c = 1$.

where $P$ denotes the four-momentum of the incoming proton. $x$ and $y$ are dimensionless variables in the range $0 \geq x, y \geq 1$. The variable $y$ corresponds to the relative energy transfer to the proton in its rest frame. It is the *inelasticity* of the scattering process.

The meaning of $x$ is illustrative in the Quark-Parton-Model [19], which is based on the assumption that the hadron taking part in the scattering process is made of point-like constituents (partons or quarks) among which the hadron momentum is distributed. It is assumed that at large $Q^2$ the quarks interact as free particles inside the hadron. In this model the scaling variable $x$ is the fractional momentum of the proton carried by the struck quark.

The electron-proton centre of mass energy $\sqrt{s}$ is given by

$$\sqrt{s} = \sqrt{(k+P)^2} \approx \sqrt{4E_e E_p}. \tag{2.9}$$

At a fixed centre of mass energy only two of these four variables are independent due to energy momentum conservation. Neglecting the electron and proton masses they are related by

$$Q^2 = xys. \tag{2.10}$$

**Cross sections in DIS**

Considering only the $\gamma$ exchange, the double differential cross section for NC DIS reactions, expressed in terms of the two variables $x$ and $Q^2$, is given by

$$\frac{\mathrm{d}^2\sigma_{NC}\,(e^{\pm}p)}{\mathrm{d}x\mathrm{d}Q^2} = \frac{4\pi\alpha^2}{xQ^4}\left[y^2 xF_1 + (1-y)F_2 \mp y(1-\frac{y}{2})xF_3\right], \tag{2.11}$$

where $\alpha$ is the fine structure constant and $F_1, F_2, F_3$ denote the proton structure functions. With the same notation the CC cross section in DIS is given by

$$\frac{\mathrm{d}^2\sigma_{CC}\,(e^{\pm}p)}{\mathrm{d}x\mathrm{d}Q^2} = \frac{G_F^2}{2\pi}\left(\frac{M_W^2}{M_W^2+Q^2}\right)^2\left[y^2 xF_1 + (1-y)\,F_2 \mp y(1-\frac{y}{2})xF_3\right], \tag{2.12}$$

where $G_F$ is the Fermi constant. Within the Quark-Parton-Model $F_1$ and $F_2$ can be expressed as a sum of the quark and anti-quark densities in the proton, and $F_3$ as a difference between the quark and anti-quark densities. In addition, the model relates $F_1$ and $F_2$ by the Callan-Gross relation [20]:

$$2xF_1(x, Q^2) = F_2(x, Q^2). \tag{2.13}$$

Interactions involving the exchange of the heavy gauge bosons $Z^0$ (NC) and $W^{\pm}$ (CC) only contribute at high $Q^2$ since the cross sections are suppressed by the propagator terms. The $Z^0$ or $W^{\pm}$ exchange and the interference between $Z^0$ and photon exchange are suppressed with respect to the $\gamma$ exchange by the following ratios :

$$\frac{\sigma(Z^0, W^{\pm})}{\sigma(\gamma)} \propto \left(\frac{Q^2}{Q^2+M_{Z^0,W^{\pm}}^2}\right)^2 \tag{2.14}$$

$$\frac{\sigma(\gamma Z^0)}{\sigma(\gamma)} \propto \frac{Q^2}{Q^2+M_{Z^0,W^{\pm}}^2}. \tag{2.15}$$

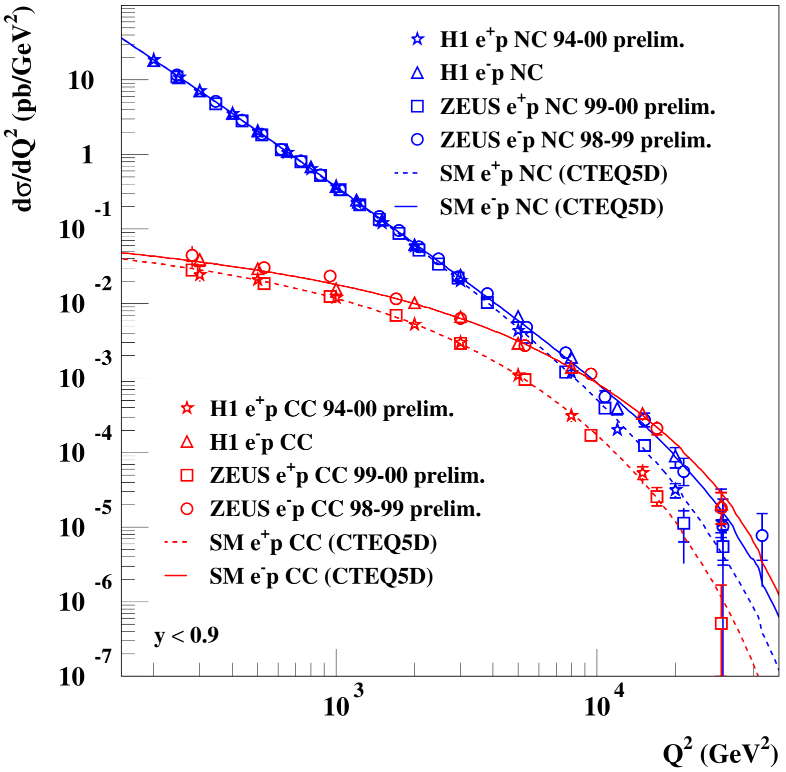


FIGURE 2.2: HERA measurements of the NC and CC DIS cross sections at high $Q^2$.

In Fig. 2.2 the measurements of the NC and CC cross sections from HERA are shown. At values of $Q^2$ which are smaller than the vector boson masses squared ($\mathcal{O}(10^4\,\mathrm{GeV}^2)$) the CC cross section is greatly suppressed with respect to the NC cross section. At high $Q^2$ the NC and CC DIS cross section are of the same order. The highest $Q^2$ domain accessible at HERA ($\sim 3 \cdot 10^4\,\mathrm{GeV}^2$) corresponds to a spatial resolution of $10^{-18}$ m. With the statistics collected at HERA by the year 2000, the measurements clearly reveal the dependence on the lepton beam charge that is predicted by the SM: an increased NC cross section for $e^-p$ collisions with respect to $e^+p$ scattering by virtue of positive instead of negative interference between $\gamma$ and $Z^0$ exchange or a decreased CC cross section for $e^+p$ reactions.

## 2.3 Motivation for theories beyond the Standard Model

The SM has been constructed as a result of numerous efforts both theoretical and experimental. At present the SM is extraordinarily successful and the confirmation of electroweak predictions of the SM is very precise – of the order of 0.1 % in some cases. Despite its great success in explaining all current experimental results the SM cannot be considered as a complete theory since it does not include gravity. The scale where gravity becomes important is the *Planck scale* given by

$$E_{Pl} = \sqrt{\hbar c/G_F} \simeq 10^{19}\,\mathrm{GeV}. \tag{2.16}$$

This scale corresponds to a *Planck length* $l_{Pl} \simeq 10^{-35}\,\mathrm{m}$. At least at such high scales or small distances the SM is not able to make any predictions. In view of the large number of free parameters and arbitrary choice of gauge groups the SM is viewed as a low-energy effective theory of some larger theory, which may be

- a grand unified theory (GUT) [21] in which the SM gauge group is unified as a part of a larger gauge group, e.g. $SU(5), SO(10)$ or $E_6$;
- a string theory which would also include gravity.

**Hierarchy problem of the Standard Model and its solution**

Independent of the fact that the SM is not the ultimate theory it suffers from a theoretical problem related to the presence of a fundamental scalar field (the Higgs field of the SM).

The masses of fundamental scalar fields show quadratic divergencies. This can be seen by considering the one-loop corrections to the Higgs mass, given by the Feynman diagram in Fig. 2.3. After regulating this divergent loop diagram by imposing a cut-off $\Lambda$, the contribution to the Higgs mass is given by

$$\delta M_{Hf}^2 = \frac{|g_f|^2}{16\pi^2}\left[-2\Lambda^2 + 6m_f^2 \ln(\Lambda/m_f)\right], \tag{2.17}$$

where terms are neglected which are finite in the limit $\Lambda \to \infty$. Here $m_f$ denotes the fermion mass and $g_f = m_f/v$ is the coupling of the fermion to the Higgs field.

The SM Higgs mass depends quadratically on the cut-off scale $\Lambda$. This is not a problem if we renormalise the theory and absorb the divergencies into a redefinition of the Higgs mass. However, regarding the SM to be an effective low-energy theory we expect $\Lambda$ to be the scale of new physics: the GUT scale or the Planck scale. This means that the natural value of the Higgs mass is $10^{14} - 10^{17}\,\mathrm{GeV}$ rather than around the electroweak scale as suggested by precise electroweak data. This problem is called the *hierarchy problem* of the SM [22].

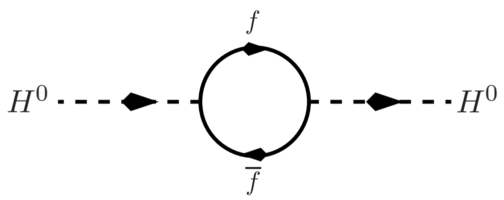


Figure 2.3: Feynman graph for the fermion one-loop correction to the Higgs mass.

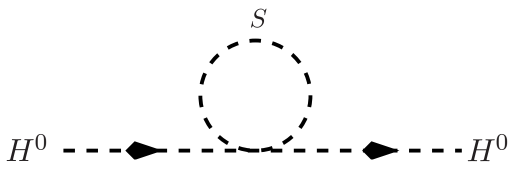


Figure 2.4: Feynman graph for the boson one-loop correction to the Higgs mass.

In order to obtain a Higgs mass of the order of the electroweak scale, the bare Higgs mass $M_{H\text{bare}}$ in the SM must be tuned:

$$M_H^2 = M_{H\text{bare}}^2 + \delta M_H^2. \tag{2.18}$$

If we require the Higgs mass $M_H$ to be around the electroweak scale the cancellation between $M_{H\text{bare}}$ and $\delta M_H$ must be roughly 1 part in $10^{12}$, which requires an enormous fine-tuning of the parameters of the bare Lagrangian, leading to the *fine-tuning* or *naturalness problem* of the SM[3].

One possible solution for the hierarchy problem is the concept of **technicolor**. In such models the scalar field responsible for $SU(2)_L \times U(1)_Y$ breaking is not fundamental, but composite of so called technifermions. Between these particles a new gauge interaction (technicolor) is introduced, which is a non-abelian force with confinement and asymptotic freedom with a scale of $\Lambda_{TC} \simeq 1\,\text{TeV}$. The problem of such models is that it is difficult to find a mechanism which gives masses to the fermions. Electroweak precision measurements strongly disfavour the technicolor concept. Some extensions (*walking technicolor*) may be still in agreement with the data, but in these models it is hard to make precise calculations. At the moment no calculable technicolor model is consistent with the electroweak data.

A very elegant way of solving the hierarchy problem is the concept of **supersymmetry**. The naturalness problem of the SM arises because the hierarchy $E_{EW} \ll E_{Pl}$ or $E_{GUT}$ is not stable under radiative corrections. The idea is to introduce another symmetry, which preserves the hierarchy and makes the SM natural.

We can see how the problem is solved by supersymmetry if we consider an additional scalar field $S$ which couples to the Higgs field by the Lagrangian $\mathcal{L} = \lambda_s H^2 S^2$. This results in an additional loop shown in Fig. 2.4 which gives an additional contribution to the Higgs mass:

$$\delta M_{HS}^2 = \frac{|\lambda_s|^2}{16\pi^2} \left[ \Lambda^2 + 2M_S^2 \ln(\Lambda/M_S) \right]. \tag{2.19}$$

If each of the quarks and leptons of the SM is accompanied by two complex scalars with $\lambda_s = |g_f|^2$, then the $\Lambda^2$ contributions of Fig. 2.3 (Eq. 2.17) and Fig. 2.4 (Eq. 2.19) cancel. In supersymmetry these states, the supersymmetric partners of quarks and leptons, are introduced. If an unbroken supersymmetry exists (i.e. the masses of the SM particle and its supersymmetric partner are the same), the quadratic contributions from fermion and boson loops cancel in all orders of perturbation theory. On the other hand, if supersymmetry is

[3] A theory is called *natural*, if its predictions at low energy are not affected by slightly changing the fundamental parameter of the theory.

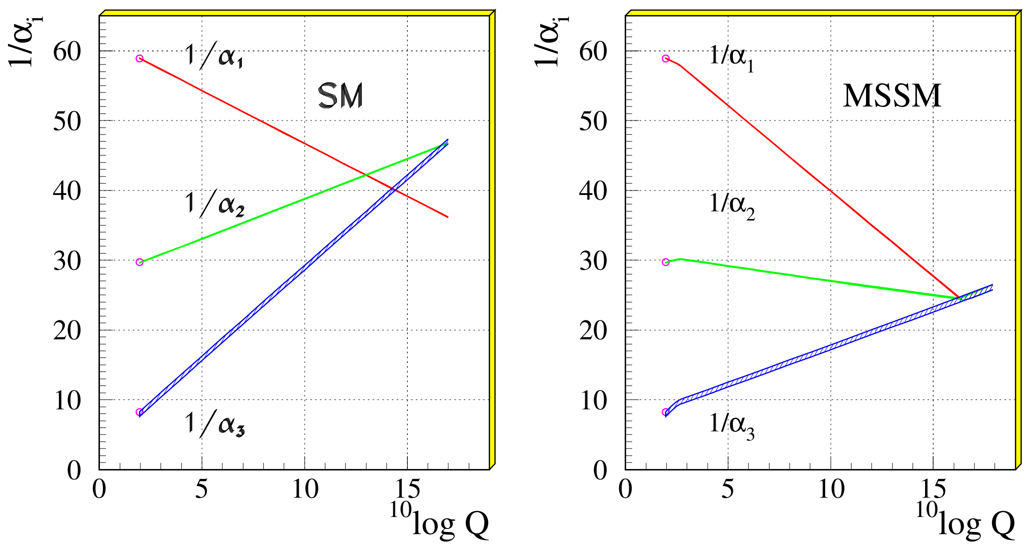


Figure 2.5: Evolution of the inverse of the three coupling constants in the Standard Model (SM) and the minimal supersymmetric extension of the SM (MSSM) [23].

broken the hierarchy problem can be solved, if the mass difference between SM particle and its superpartner is still smaller than about 1 TeV. This means that supersymmetric particles must exist with masses below 1 TeV.

### Interesting properties of supersymmetric theories

The basic idea of grand unification is to seek a simple gauge group that includes the gauge group of the SM given in Eq. 2.1. A first apparent obstacle is the fact that the coupling constants of the strong, weak and electromagnetic interaction are very different at present-day energies. However, the running of the coupling constants is given by the renormalisation group equation (RGE) and is illustrated in Fig. 2.5 for the SM and for the minimal[4] supersymmetric extension of the SM (MSSM). Only in the latter case unification is obtained at scales around $10^{16}$ GeV. The SUSY particles contribute only above the effective SUSY scale of about 1 TeV, which causes a change in the slope in the evolution of the couplings.

Besides the solution of the hierarchy problem and the unification of coupling constants further strong arguments for supersymmetry are:

- If supersymmetry is embedded in a grand unified theory and the unifications of the coupling constants is assumed, it makes a very precise prediction of the electroweak mixing parameter $\sin^2\theta_W$ which has been confirmed experimentally at LEP at the per mill level.

[4] *minimal* with respect to the particle content

- In supersymmetric models the Higgs boson corresponding to the SM Higgs field should be light as suggested by fits of the Higgs mass to electroweak precision measurements [4].
- In supersymmetric models the electroweak symmetry breaking is a natural result of renormalisation group evaluation.
- The lightest supersymmetric particle (LSP) is a good candidate to explain the density of dark matter needed in astrophysics and cosmology.
- If supersymmetry is formulated as a *local* symmetry, it naturally incorporates gravity since a field of spin 2 must be introduced, which can be identified as the graviton. Thus supersymmetry seems to be an important ingredient for an ultimate theory, which takes into account the gravitational interaction.

## 2.4 Supersymmetry

In the following the basic concepts of supersymmetry are presented, focussing on the particle content and properties of the MSSM. For a detailed description see [2, 3, 24].

A supersymmetry transformation $Q$ turns a bosonic state into a fermionic state and vice versa:

$$Q|\text{boson}\rangle = |\text{fermion}\rangle \qquad Q|\text{fermion}\rangle = |\text{boson}\rangle \tag{2.20}$$

If a theory is invariant under this transformation, it is called supersymmetric. Following the Coleman-Mandula theorem [25] the properties of the symmetry are very restricted and the operator $Q$ must satisfy the following commutation and anticommutation relations:

$$\{Q, Q^\dagger\} = \quad P^\mu \tag{2.21}$$
$$\{Q, Q\} = \{Q^\dagger, Q^\dagger\} \quad = 0 \tag{2.22}$$
$$[P^\mu, Q] = \left[P^\mu, Q^\dagger\right] \quad = 0, \tag{2.23}$$

where $P^\mu$ is the momentum generator of spacetime translations.

The irreducible representations of this *superalgebra* are called *supermultiplets*. A supermultiplet contains both fermionic and bosonic states (*superpartners*). It can be shown from first principles that in unbroken supersymmetry particles of the same supermultiplet must have the same mass, the same electric charge, the same weak isospin and the same color [24]. In addition, the number of fermionic degrees of freedom and the number of bosonic degrees of freedom in a supermultiplet must be the same.

The simplest possible supermultiplet satisfying such conditions is the combination of a two-component Weyl fermion and a complex scalar field. This multiplet is called a *matter* or *chiral* supermultiplet. The next simplest case of a supermultiplet contains a vector boson with spin 1 which is massless before spontaneous symmetry breaking (i.e. two states) and again a Weyl fermion (two states). Such a supermultiplet is called a *gauge* supermultiplet.

A supersymmetric model with only gauge and chiral multiplets is called "N=1 supersymmetry". More extended supersymmetries with other possible combinations of particles with spin have no phenomenological relevance.

### 2.4.1 The Minimal Supersymmetric Standard Model

In supersymmetric extensions of the SM each of the known particles must be arranged in either a chiral or a gauge supermultiplet. The basic concepts of the extension which is minimal with respect to the particle content are presented in the following.

#### Particle content of chiral supermultiplets in the MSSM

Since the left-handed and right-handed SM fermions (quarks and leptons) have different gauge transformations they must be members of chiral supermultiplets [24]. The left-handed and right-handed quarks and leptons are Weyl fermions and each must have its own complex scalar partner, called a *squark* (for scalar quark) or a *slepton* (for scalar lepton) respectively. They are denoted with a tilde. For instance the $\tilde{e}_L$, $\tilde{\mu}_L$ and $\tilde{\tau}_L$ are scalar partners of the left-handed leptons $e_L$, $\mu_L$ and $\tau_L$. Note that for squarks and sleptons the handedness does not refer to the helicity of the squark or slepton, which are scalar, but to the helicity of the corresponding superpartners (quarks and leptons). The particle content of all chiral supermultiplets is given in Tab. 2.3.

The scalar Higgs boson must be a member of a chiral supermultiplet since it has a spin of 0. However, only one chiral Higgs supermultiplet is not enough, otherwise the model would be inconsistent as a quantum theory since so called triangle gauge anomalies occur. One Higgs chiral supermultiplet with $Y = 1/2$, which gives masses to up-type quarks $(u, c, t)$, called $H_u$, and one Higgs chiral supermultiplet with $Y = -1/2$, which gives masses to down-type quarks $(d, s, b)$ and to charged leptons $(e, \mu, \tau)$, called $H_d$, must be introduced (see Tab. 2.3). So the scalar Higgs fields in supersymmetric extensions of the SM consist of two complex $SU(2)_L$-doublets $(H_u^+, H_u^0)$ and $(H_d^0, H_d^-)$, which have non-zero vacuum expectation values $v_u$ and $v_d$. This corresponds to eight real scalar degrees of freedom. The ratio of the two vacuum expectation values

$$\tan\beta = v_u/v_d \tag{2.24}$$

is a free parameter of the theory.

In analogy to the SM three of these degrees of freedom become the longitudinal modes of the massive weak vector bosons $(W^\pm, Z^0)$ when the electroweak symmetry is broken.

| name | | spin 0 | spin 1/2 |
|---|---|---|---|
| squarks, quarks | $Q$ | $(\tilde{u}_L \;\; \tilde{d}_L)$ | $(u_L \;\; d_L)$ |
| (× 3 generations) | $U$ | $\tilde{u}_R^\star$ | $u_R^\dagger$ |
| | $D$ | $\tilde{d}_R^\star$ | $d_R^\dagger$ |
| sleptons, leptons | $L$ | $(\tilde{\nu}_L \;\; \tilde{e}_L)$ | $(\nu \;\; e_L)$ |
| (× 3 generations) | $E$ | $\tilde{e}_R^\star$ | $e_R^\dagger$ |
| Higgs, higgsinos | $H_u$ | $(H_u^+ \;\; H_u^0)$ | $(\tilde{H}_u^+ \;\; \tilde{H}_u^0)$ |
| | $H_d$ | $(H_d^0 \;\; H_d^-)$ | $(\tilde{H}_d^0 \;\; \tilde{H}_d^-)$ |

TABLE 2.3: Chiral supermultiplets in the MSSM.

| name | spin 1/2 | spin 1 |
|---|---|---|
| gluino, gluon | $\tilde{g}$ | $g$ |
| winos, $W$ bosons | $\tilde{W}^{\pm}$ $\tilde{W}^0$ | $W^{\pm}$ $W^0$ |
| bino, $B$ boson | $\tilde{B}^0$ | $B^0$ |

Table 2.4: Gauge supermultiplets in the MSSM.

The remaining five belong to Higgs mass eigenstates: one $CP$-odd neutral scalar $A^0$, a positively charged scalar $H^+$ and its conjugate scalar $H^-$, and two $CP$-even neutral scalars $H^0$ and $h^0$. The latter corresponds to the neutral scalar Higgs boson of the SM. These states are linear combinations of $H_u^+, H_u^0, H_d^0$ and $H_d^-$.

It is a very nice feature of supersymmetric models that it is possible to break the electroweak symmetry by radiative corrections. Assuming this, at tree-level the mass of $h^0$ must be smaller than the mass of the $Z^0$ boson, which is excluded by the direct searches for the Higgs boson. However this limit is subject to significant quantum corrections leading to a weaker bound:

$$m_{h^0} \leq 150\,\text{GeV}. \tag{2.25}$$

For this reason a light Higgs boson, suggested by the mass fits to electroweak precision measurements, is a strong hint for supersymmetry.

The nomenclature for a spin 1/2 superpartner is to append "-ino" to the name of the SM particle. Thus, the superpartners of $(H_u^+, H_u^0)$ and $(H_d^0, H_d^-)$, denoted with $(\tilde{H}_u^+, \tilde{H}_u^0)$ and $(\tilde{H}_d^0, \tilde{H}_d^-)$ respectively, are called higgsinos.

Attempts to put a scalar Higgs and a neutrino in the same chiral supermultiplets, which would naively seem more economical, played a key role to connect supersymmetry to phenomenology [26], but they turned out not to work since they lead to many insoluble phenomenological problems like lepton number violation and neutrino masses not in agreement with experimental results.

### Particle content of gauge supermultiplets in the MSSM

The vector bosons of the SM are members of a gauge supermultiplet. Their superpartners are called gauginos, which are denoted by a tilde. The partner of the spin 1 $SU(3)_C$ gauge boson, the gluon ($g$), is the gluino ($\tilde{g}$) which has spin 1/2. The $SU(2)_L \times U(1)_Y$ gauge bosons of the SM are $W^{\pm}, W^0$ and $B^0$. Their spin 1/2 partners are called winos ($\tilde{W}^{\pm}, \tilde{W}^0$) and bino ($\tilde{B}^0$). The particle content of all gauge supermultiplets is given in Tab. 2.4. As in the SM the $W^0$ and $B^0$ gauge eigenstates mix to form the mass eigenstates $Z^0$ and $\gamma$. The corresponding mixtures of $\tilde{W}^0$ and $\tilde{B}^0$ are called the zino ($\tilde{Z}^0$) and the photino ($\tilde{\gamma}$).

### Neutralinos and charginos

Because of electroweak symmetry breaking effects, the superpartners listed in Tab. 2.3 and Tab. 2.4 are not necessarily the mass eigenstates of the theory. Mixing can appear between electroweak gauginos and the higgsinos, and between the various squarks and sleptons and the Higgs scalars which have the same electric charge. The neutral states, i.e. the two neutral gauginos $(\tilde{B}^0, \tilde{W}^0)$ and the two neutral higgsinos $(\tilde{H}_u^0, \tilde{H}_d^0)$, combine to form the four neutral mass eigenstates which are called *neutralinos*. Neutralinos are denoted by $\chi_i^0$ with $i = 1...4$. The charged states, i.e. the two winos $(\tilde{W}^-, \tilde{W}^+)$ and the two charged higgsinos $(\tilde{H}_u^+, \tilde{H}_d^-)$, mix to form the two mass eigenstates with charge $\pm 1$ which are called *charginos* denoted by $\chi_i^\pm$ with $i = 1, 2$. By convention the neutralinos and charginos are ordered in mass:

$$m_{\chi_1^0} < m_{\chi_2^0} < m_{\chi_3^0} < m_{\chi_4^0}; \qquad m_{\chi_1^\pm} < m_{\chi_2^\pm}. \tag{2.26}$$

In the gauge-eigenstate basis $\psi^0 = (\tilde{B}^0, \tilde{W}^0, \tilde{H}_d^0, \tilde{H}_u^0)$ the mass term for **neutralinos** in the Lagrangian is given by

$$\mathcal{L} = -\frac{1}{2}(\psi^0)^T M_N \psi^0 + c.c., \tag{2.27}$$

where $M_N$ is the neutralino mass matrix given by

$$M_N = \begin{pmatrix} M_1 & 0 & -c_\beta s_W m_Z & s_\beta s_W m_Z \\ 0 & M_2 & c_\beta c_W m_Z & -s_\beta c_W m_Z \\ -c_\beta s_W m_Z & c_\beta c_W m_Z & 0 & -\mu \\ s_\beta s_W m_Z & -s_\beta c_W m_Z & -\mu & 0 \end{pmatrix}. \tag{2.28}$$

Here the abbreviations $s_\beta = \sin\beta$, $c_\beta = \cos\beta$, $s_W = \sin\theta_W$ and $c_W = \cos\theta_W$ are used. $m_Z$ is the mass of the $Z^0$, $\theta_W$ denotes the Weinberg angle, $\beta$ is given by Eq. 2.24, $\mu$ is a mixing term between the two Higgs doublets and $M_1$ and $M_2$ are the masses of $\tilde{B}^0$ and $\tilde{W}^0$. Assuming the unification of the gauge coupling constants (see Fig. 2.5) the parameters $M_1$ and $M_2$ are related by

$$M_1 = \frac{5}{3}\tan^2\theta_W M_2. \tag{2.29}$$

Diagonalising the matrix $M_N$ gives its eigenstates and eigenvalues. The eigenvalues are the masses of the neutralinos. The eigenstates give the linear combination of $\tilde{\gamma}, \tilde{Z}, \tilde{H}_d^0$ and $\tilde{H}_u^0$, which form the neutralinos.

As in the neutralino sector the **chargino** spectrum can be calculated. In the basis $\psi^\pm = (\tilde{W}^+, \tilde{H}_u^+, \tilde{W}^-, \tilde{H}_d^-)$ the mass term in the Langrangian is given by

$$\mathcal{L} = -\frac{1}{2}(\psi^\pm)^T M_C \psi^\pm + c.c., \tag{2.30}$$

where $M_C$ is the chargino mass matrix:

$$M_C = \begin{pmatrix} 0 & X^T \\ X & 0 \end{pmatrix} \qquad \text{with} \quad X = \begin{pmatrix} M_2 & \sqrt{2}\sin\beta m_W \\ \sqrt{2}\cos\beta m_W & \mu \end{pmatrix}. \tag{2.31}$$

Again the masses and the composition of the chargino states can be calculated by diagonalising the matrix.

Thus, following the relationship of Eq. 2.29 the composition and the masses of neutralinos and charginos are completely determined for given values of $\mu, M_2$ and $\tan\beta$. The composition of the $\chi_1^0$ is illustrated in Fig. 2.6, where its dominant components are shown

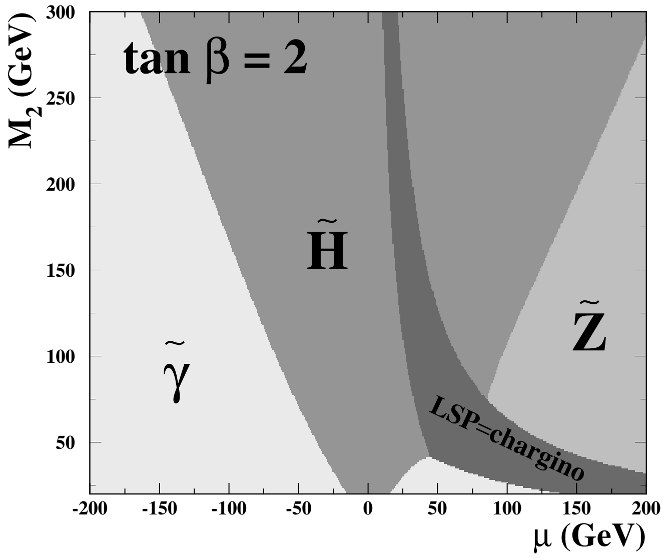


Figure 2.6: Composition of the lightest neutralino ($\chi_1^0$). For a fixed value of $\tan\beta = 2$ the regions of the SUSY phase space $(\mu, M_2)$ corresponding to a $\chi_1^0$ dominated by its photino, zino or higgsino component are shown. In a small parameter region the $\chi_1^0$ is not the LSP.

in the $(\mu, M_2)$-plane for a fixed value of $\tan\beta$. For small values of $\mu$ and $M_2$ the $\chi_1^0$ is dominated by its photino component. For intermediate values of $\mu$ and higher values of $M_2$ the higgsino component is dominant, whereas the zino component is most important for high values of $\mu$. In large parts of the parameter space the $\chi_1^0$ is the lightest supersymmetric particle (LSP) being a good candidate to solve the cold dark matter density problem in cosmology. Only in a small parameter region the LSP is not the lightest neutralino $\chi_1^0$ but the lightest chargino $\chi_1^\pm$.

To give an idea of how the masses of neutralinos and charginos depend on the supersymmetric parameters, the masses of the four neutralino states and the two chargino states are shown in Fig. 2.7 as a function of $\mu$ for one particular parameter choice $(\tan\beta = 2, M_2 = 150\,\mathrm{GeV})$. Some interesting properties of the masses can be observed for the region $|\mu| > M_2$: The mass of the lightest neutralino ($\chi_1^0$) is approximately given by $M_2/2$. The lighter chargino ($\chi_1^\pm$) is nearly degenerate with the second lightest neutralino ($\chi_2^0$) and their mass can be approximated by $M_2$. $\chi_3^0$, $\chi_4^0$ and $\chi_2^\pm$ have masses of the order of $|\mu|$. These general remarks are true for a lot of SUSY scenarios, but are not mandatory. For more details on the parameter dependence of neutralino and chargino masses see [27].

### Mixing of squark states

Mixing of weak eigenstates also occurs in the squark and slepton sector. In principle, any scalars with the same quantum numbers can mix with each other. However the general hypothesis of *flavor-blind soft parameters* [24] predicts that the corresponding mixing angles are very small if the masses of the corresponding quarks and leptons are small.

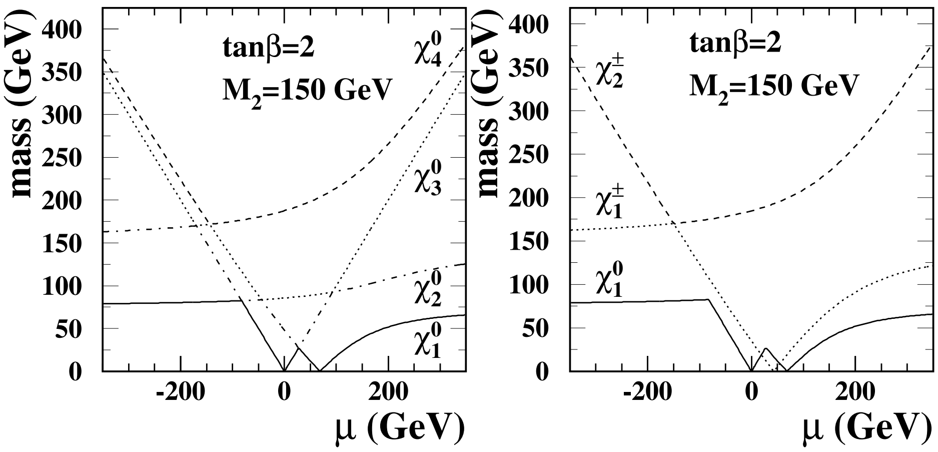


FIGURE 2.7: Masses of neutralinos and charginos for $\tan\beta = 2$ and $M_2 = 150\,\mathrm{GeV}$ as a function of $\mu$. By definition the states $\chi_1^0$, $\chi_2^0$, $\chi_3^0$, $\chi_4^0$ and $\chi_1^\pm$, $\chi_2^\pm$ are ordered in mass. In a small region the lightest chargino ($\chi_1^\pm$) is the LSP.

Thus for the first two families nearly unmixed states occur which are degenerate in mass.

In contrast the third-family squarks and sleptons can have very different masses compared to their first- and second-family counterparts. In particular in the case of the stop one expects a large mixing between the weak eigenstates $\tilde{t}_L$ and $\tilde{t}_R$ thus making the lighter mass eigenstate[5] $\tilde{t}_1$ presumably lighter than the squark states of the first two generations. As a result, the $t_1$ is the lightest squark in large parts of the supersymmetric parameter space.

The mixing is usually described by a matrix which depends on the value of $\tan\beta$. This matrix can be diagonalized leading to the mixing angle $\theta_t$:

$$\begin{pmatrix} \tilde{t}_1 \\ \tilde{t}_2 \end{pmatrix} = \begin{pmatrix} \cos\theta_t & \sin\theta_t \\ -\sin\theta_t & \cos\theta_t \end{pmatrix} \begin{pmatrix} \tilde{t}_L \\ \tilde{t}_R \end{pmatrix}. \tag{2.32}$$

Similarly to the stop states the weak states in the sbottom and stau sector mix: e.g. the sbottom states $\tilde{b}_L$ and $\tilde{b}_R$ mix to form the mass eigenstates $\tilde{b}_1 = \cos\theta_b\tilde{b}_L + \sin\theta_b\tilde{b}_R$ and $\tilde{b}_2 = -\sin\theta_b\tilde{b}_L + \cos\theta_b\tilde{b}_R$. The magnitude and importance of mixing in the sbottom and stau sector depends on $\tan\beta$. If $\tan\beta$ is small (less than $\sim 10$) the sbottoms and staus do not get a large effect from mixing, whereas for large values the mixing is quite significant.

### *R*-parity

In the literature supersymmetric models are described using the notation in *superspace*. In this notation *superfields* are single objects containing as components all the bosonic, fermionic (and auxiliary) fields within the corresponding supermultiplets of Tab. 2.3 and Tab. 2.4. *Superpotentials* describe the interactions and masses of all particles. Given the

[5]By convention the light and heavy mass eigenstates are denoted by $\tilde{t}_1$ and $\tilde{t}_2$ respectively.

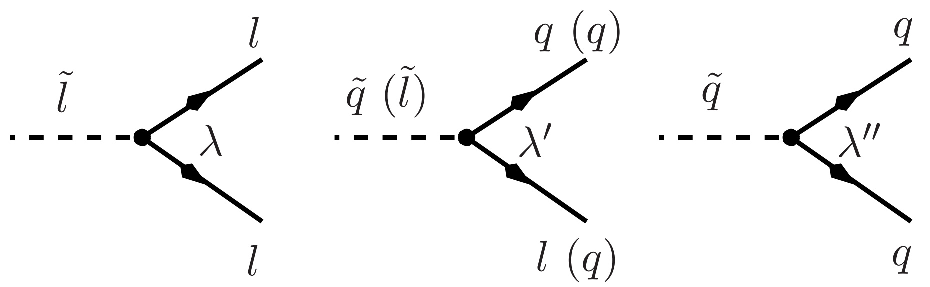


FIGURE 2.8: Diagrams corresponding to $\underline{R_p}$ violating terms described by Eq. 2.33. $\lambda_{ijk}L_iL_j\overline{E}_k$ (left); $\lambda'_{ijk}L_iQ_j\overline{D}_k$ (middle); $\lambda''_{ijk}\overline{U}_i\overline{D}_j\overline{D}_k$ (right). The process in the middle is of particular interest in *ep* collisions.

supermultiplet content of the theory, the form of the superpotential is restricted by gauge invariance. For more details of this notation see for example [2].

The most general gauge invariant and renormalisable supersymmetric theory allows for terms that violate either lepton number or baryon number conservation. The corresponding part of the superpotential in superfield notation is given by

$$W_{\not{R}} = \frac{1}{2}\lambda_{ijk}L_iL_j\overline{E}_k + \lambda'_{ijk}L_iQ_j\overline{D}_k + \frac{1}{2}\lambda''_{ijk}\overline{U}_i\overline{D}_j\overline{D}_k, \tag{2.33}$$

where $L, Q, D$ and $E$ denote the superfields corresponding to the chiral supermultiplets of Tab. 2.3. $\lambda_{ijk}$, $\lambda'_{ijk}$ and $\lambda''_{ijk}$ are dimensionless Yukawa couplings and $i, j, k = 1, 2, 3$ are family indices. The new couplings introduced by these terms are shown in Fig. 2.8. They allow the coupling of two ordinary SM fermions and a supersymmetric particle. The second term ($\lambda'_{ijk}L_iQ_j\overline{D}_k$) is of special interest for *ep* collisions since it introduces a quark-lepton-squark vertex.

Violation of lepton number or baryon number conservation has never been seen experimentally. The strongest experimental result comes from the non-observation of proton decay: the current lower limit for its lifetime is $\tau_p > 10^{32}$ years. If both $\lambda'$ and $\lambda''$ were non-zero the proton would decay via the diagram shown in Fig. 2.9. If the two couplings are of the order of one, the lifetime of the proton would be of the order of minutes.

The standard way to avoid this kind of problems is to completely cancel the terms in Eq. 2.33. This can be achieved by introducing a new multiplicative conserved quantum number, which is called $R$-parity $R_p$. Its definition is

$$R_p = (-1)^{3B+L+2S}, \tag{2.34}$$

where $B$ is the baryon number, $L$ is the lepton number and $S$ denotes the spin of a particle. With this definition ordinary SM particles have $R_p = +1$, whereas their SUSY partners carry $R_p = -1$.

$R_p$ conservation has important consequences for phenomenology: The lightest supersymmetric particle is absolutely stable[6]. In contrast, each sparticle (other than the LSP)

[6]If the LSP is the lightest neutralino $\chi_0^1$ it is only weakly interacting in large parts of the parameter space. Thus, a stable LSP gives rise to the *golden signature* of missing energy in collider experiments.

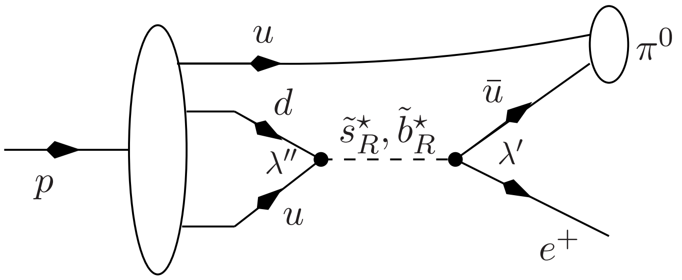


FIGURE 2.9: Feynman diagram of the $\not{R}_p$ proton decay, $p \rightarrow \pi^0 e^+$.

decays to a state including an odd number of LSPs. Since the initial state in any collider experiment contains only SM particles, SUSY particles must be produced in pairs.

In the MSSM $R_p$ is a conserved quantum number, but $R_p$ conservation has no strong theoretical justification. In particular there is no experimental evidence for $R_p$ conservation or violation. Even with the $\not{R}_p$ terms of Eq. 2.33 present in the theory it is possible to construct models which do not contradict the experimental results. The limit on the lifetime of the proton can be translated into a bound on the product of the couplings at the two vertices in Fig. 2.9 as a function of the mass of the exchanged squark [14]:

$$\lambda'_{11k}\lambda''_{11k} < 2 \cdot 10^{-27} \left( \frac{m_{\tilde{d}_k}}{100\,\mathrm{GeV}} \right)^2 . \tag{2.35}$$

This bound is so strict that the only natural explanation is that at least one of the couplings vanishes. For this reason in $\not{R}_p$ models it is usually assumed that only one term in Eq. 2.33 has a coupling constant with a non-zero value. In the analysis presented here this common assumption is made as well.

In such models $\not{R}_p$ changes the SUSY phenomenology drastically. The most important consequences are:

- The lightest supersymmetric particle decays to SM particles: the typical missing energy signature in the $R_p$ conserving MSSM is replaced by multi-lepton and/or multi-jet final states.
- Two known SM fermions can couple to form a squark or a slepton by the processes shown in Fig. 2.8. Thus it is possible to produce single SUSY particles resonantly at collider experiments.

There are two ways of searching for experimental signatures of $\not{R}_p$ models: The first is the study of the production of sparticle pairs by $R_p$ conserving processes followed by $\not{R}_p$ decays. The second way is to study the possibility of single sparticle production (see Sec. 2.5). The latter approach is used in this analysis.

### $R_p$-conserving sparticle decays

In this section an overview of the decay pattern of supersymmetric particles in the MSSM, i.e. with $R_p$ conservation, is given. If the $\chi_1^0$ is the LSP then all decay chains will end up

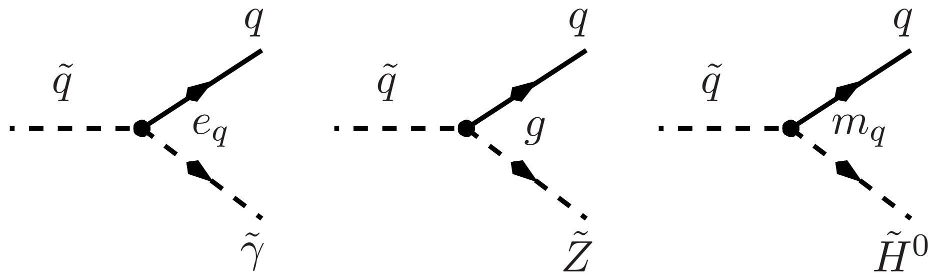


FIGURE 2.10: Feynman diagrams for $R_p$ conserving squark decays to neutralinos.

in final states containing it.

Of special interest for this analysis are **squarks**. In the MSSM they decay to a quark and a gaugino:

$$\tilde{q} \to q\tilde{g}, \quad \tilde{q} \to q\chi_i^0, \quad \tilde{q} \to q'\chi_i^{\pm}. \tag{2.36}$$

If kinematically allowed the decay to a gluino will always dominate since it has strong coupling strength. The diagrams for the squark decay to neutralinos are shown componentwise in Fig. 2.10 – coupling strengths are indicated. The decays to charginos are illustrated in Fig. 2.11.

It is important to note that the couplings of a squark to charginos depend drastically on the handedness of its SM partner. The supersymmetric partners of right-handed quarks ("right" squarks) do not couple to winos since the weak interaction couples only to the left component. These squarks couple to charginos only via their higgsino component with couplings proportional to the mass of the quark. Thus the couplings of a "right" squark $\tilde{q}_R$ to charginos are suppressed. In contrast a "left" squark has couplings to both neutralinos and charginos. If the decay to a gluino is kinematically forbidden but the decay to charginos and neutralinos is accessible, a "left" squark never decays dominantly to $\chi_1^0$ – the decay to a chargino ($\chi_1^{\pm}$) will dominate [28]. If the secondary gaugino in the squark decay is not the LSP (usually the $\chi_1^0$), it will in turn decay until the LSP ($\chi_1^0$) is reached. This leads to complicated cascade squark decays among which the process $\tilde{q}_L \to \chi_1^{\pm} \to \chi_1^0$ usually has the highest branching fraction.

Since the **neutralinos and charginos** are mixtures of $\tilde{\gamma}, \tilde{Z}, \tilde{W}$ and $\tilde{H}$, they inherit the couplings of their components. Hence the following decay modes into fermion + sfermion are open, if the decay products are light enough:

$$\chi_i^0 \to l\tilde{l}, \nu\tilde{\nu}, q\tilde{q} \quad \text{and} \quad \chi_i^{\pm} \to l\tilde{\nu}, \nu\tilde{l}, q\tilde{q}'. \tag{2.37}$$

In addition, neutralinos and charginos get a gaugino-higgsino-Higgs and gaugino-gaugino-vector boson couplings of their components [24]. This results in decays of $\chi_i^0$ and $\chi_i^{\pm}$ into a lighter $\chi_j^0$ or $\chi_j^{\pm}$ and a Higgs scalar or an electroweak gauge boson:

$$\chi_i^0 \to Z^0\chi_j^0,\, W^{\mp}\chi_j^{\pm},\, h^0\chi_j^0, \quad (A^0\chi_j^0,\, H^0\chi_j^0,\, H^{\mp}\chi_j^{\pm}) \tag{2.38}$$

$$\chi_i^{\pm} \to W^{\pm}\chi_j^0,\, Z^0\chi_1^{\pm},\, h^0\chi_j^{\pm}, \quad (A^0\chi_1^{\pm},\, H^0\chi_1^{\pm},\, H^{\pm}\chi_j^0) \tag{2.39}$$

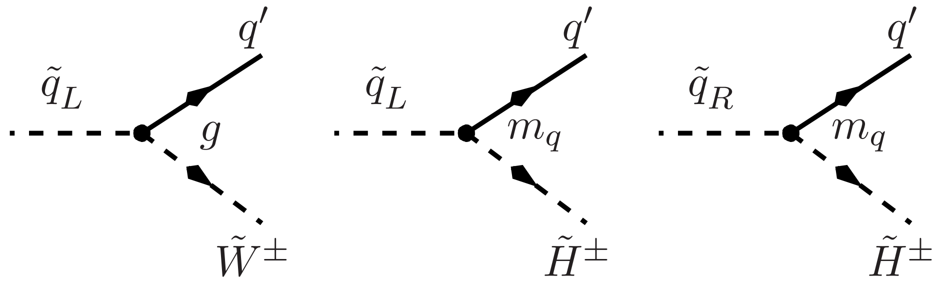


Figure 2.11: Feynman diagrams for $R_p$ conserving squark decays to charginos.

The decay in brackets are kinematically suppressed since usually $h^0$ is the lightest Higgs boson. If the two body decay modes in Eq. 2.38 and Eq. 2.39 are kinematically not allowed, three body decays via off-shell intermediate particles open up:

$$\chi_i^0 \to ff\chi_j^0, \quad \chi_i^0 \to ff'\chi_j^{\pm}, \quad \chi_i^{\pm} \to ff'\chi_j^0, \quad \chi_2^{\pm} \to ff'\chi_1^{\pm}. \tag{2.40}$$

In Fig. 2.12 the decays of charginos to the lightest neutralino are summarised.

Because of the gaugino mixture of charginos and neutralinos, **sleptons** decay with electroweak strength to leptons and neutralinos or charginos:

$$\tilde{l} \to l\chi_i^0, \quad \tilde{l} \to \nu\chi_i^{\pm}, \quad \tilde{\nu} \to \nu\chi_i^0, \quad \tilde{\nu} \to l\chi_i^{\pm}. \tag{2.41}$$

Decays of **gluinos** $\tilde{g} \to q\tilde{q}$ proceed via the strong coupling. If this two-body decay is kinematically allowed it will dominate. Otherwise, i.e. if all squarks are heavier than the gluino, the latter decays in three-body reactions via off-shell squarks: $\tilde{g} \to qq'\chi_i^0$ and $\tilde{g} \to qq'\chi_i^{\pm}$. The gluino mass parameter is called $M_3$.

### Free parameters of the MSSM

One weakness of the MSSM is the large number of free parameters in the theory. In addition to the 19 parameters of the SM[7], its minimal supersymmetric extension possesses 105 free parameters which are independent: There are 21 squark and slepton masses, 36 real mixing angles, 40 $CP$-violating phases that can appear in squark and slepton interactions, five real parameters in the gaugino/higgsino sector and three $CP$-violating phases in this sector. The most general supersymmetric extension of the SM which conserves $R_p$ is therefore called MSSM-124. This theory is viable only at very special *exceptional* points of the full parameter space – in the MSSM-124 there are unsuppressed FCNC, no conservation of the separate lepton numbers and new sources of $CP$ violation that are inconsistent with experimental data. As a result almost the entire MSSM-124 parameter space is ruled out.

[7]If neutrino masses and mixing are taken into account in the SM this number is increased to 26.

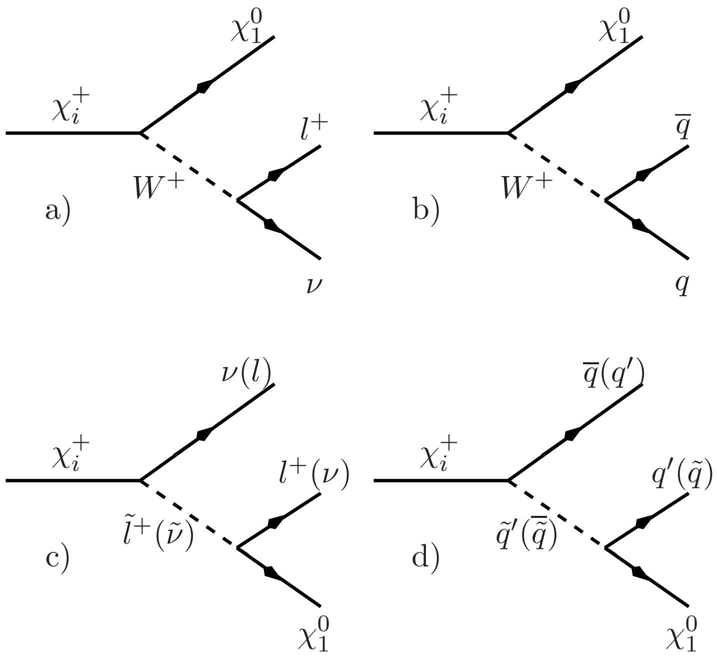


FIGURE 2.12: $R_p$ conserving decay modes of charginos to the lightest neutralino.

**HERA results in the MSSM**

At HERA the dominant MSSM process in which $R_p$ conservation is not violated is the production of a selectron and a squark via a t-channel exchange of a neutralino $eq \rightarrow \tilde{e}\tilde{q}$ and the subsequent decays: $\tilde{e} \rightarrow e\chi, \tilde{q} \rightarrow q\chi$. Thus the signature of this process is an electron with high transverse momentum, a jet and missing energy.

The HERA collaborations have searched for this signature [29, 30], but no deviation from the SM expectation was found. The analyses have set limits on the sum of the selectron and squark masses: $(m_{\tilde{e}} + m_{\tilde{q}})/2 > 77\,\mathrm{GeV}$, an interesting result at the time. Today this limit is no longer competitive with new results from LEP and TeVatron.

### 2.4.2 Breaking of supersymmetry

Members of the same supermultiplet must have the same masses. Since no supersymmetric particle has yet been seen experimentally, supersymmetry must be a broken symmetry in the vacuum state chosen by nature. By introducing certain models for SUSY breaking the number of free parameters in the MSSM can be drastically reduced.

To solve the hierarchy problem breaking of SUSY must be spontaneous. Since none of the fields in the MSSM can develop non-zero vacuum expectation value without spoiling the gauge invariance, it is believed that the breaking of supersymmetry takes place via some other field in a *hidden* sector. The hidden sector and the ordinary (visible) sector interact by *messenger* fields.

Today basically three mechanisms are known which can mediate the SUSY breaking from the hidden sector to the visible sector. In *gauge mediated* models (GMSB) [31], supersymmetry breaking is transmitted to the MSSM via gauge forces. The messengers are the gauge bosons and the matter fields of the SM. In this scenario the gravitino, the supersymmetric partner of the graviton, has a mass which is typically in the eV to keV range and it is therefore the LSP. The phenomenology of such models strongly depends on the nature of the next-to-lightest supersymmetric particle (NLSP).

In *Anomaly Mediated* Symmetry Breaking models (AMSB) the SUSY breaking is not directly communicated from the hidden to the visible sector. The gauginos masses are generated at one loop and scalar masses at two loops.

The most attractive scenario is *gravity mediated* supersymmetry breaking, which leads to the minimal Supergravity Model (mSUGRA) [32]. In the following only the very basic ideas and the parameters of this model are introduced.

**The minimal Supergravity Model (mSUGRA)**

If supersymmetry is a local symmetry, then the theory must incorporate gravity. The resulting theory is called supergravity. In models of spontaneously broken supergravity (via the *Super Higgs mechanism*), the spin 3/2 partner of the graviton, the gravitino ($\tilde{g}_{3/2}$) with a mass $m_{3/2}$ occurs. The breaking is transmitted to the visible sector by gravitational interactions. In this scenario the gravitino mass is of the order of the electroweak-symmetry-breaking scale, while its couplings have roughly gravitational strength. Such a gravitino plays no phenomenological role at collider experiments.

In the more specific minimal supergravity (mSUGRA) model all scalar particles (sfermions and Higgs bosons) have a common mass $m_0$ at the unification scale $M_{GUT} \approx 10^{16}$ GeV. The gaugino masses $M_1, M_2, M_3$ (corresponding to $U(1), SU(2)$ and $SU(3)$) unify at $M_{\mathrm{GUT}}$ to a common gaugino mass $m_{1/2}$ and all trilinear couplings $A_{ijk}$ that describe the Higgs-squark-squark and Higgs-slepton-slepton vertex have the same value $A_0$. Also the electroweak and strong coupling constants unify at the GUT scale. The evolution of the parameters towards low scales is given by the Renormalisation Group Equations.

By requiring in addition Radiative Electroweak Symmetry Breaking (REWSB) the number of free parameters is further reduced since the modulus of $\mu$ is related to the other parameters. As a result the mSUGRA model is completely determined by only a few parameters:

$$m_0, \quad m_{1/2}, \quad A_0, \quad \tan\beta \quad \text{and the sign of } \mu. \tag{2.42}$$

The full supersymmetric mass spectrum and all couplings at lower scales can be calculated by making use of the RGE. In mSUGRA the gluino mass parameter $M_3$ is related to the bino and wino mass parameters $M_1$ and $M_2$ by

$$M_3 = \frac{\alpha_s}{\alpha} \sin^2\theta_W M_2 = \frac{3}{5}\frac{\alpha_s}{\alpha} \cos^2\theta_W M_1 \tag{2.43}$$

at any RG scale. This leads to the appropriate prediction

$$M_3 : M_2 : M_1 \quad \approx \quad 7 : 2 : 1. \tag{2.44}$$

Therefore we expect that the gluino is much heavier than the lighter neutralinos and charginos.

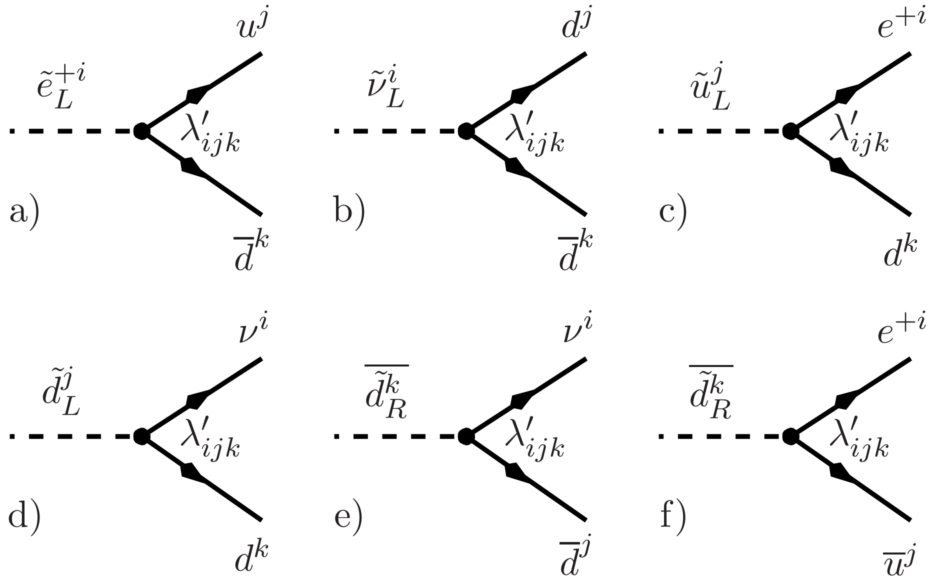


FIGURE 2.13: $\not{R}_p$ interaction vertices with $\lambda'_{ijk} \neq 0$. Each vertex corresponds to a term in Eq. 2.45.

## 2.5 Phenomenology of $\not{R}_p$ SUSY in *ep* collisions

### 2.5.1 Resonant squark production at HERA

The initial state of electrons and protons at HERA gives a unique chance to look for new particles with couplings to an electron and a quark. In supersymmetric models, where the violation of $R_p$ is allowed by presence of $\lambda' LQ\overline{D}$ in the superpotential (see Eq. 2.33), a lepton–quark–squark vertex occurs (see Fig. 2.8). This vertex makes it possible to look for the resonant production of squarks in *ep* collisions.

If we expand the superfields of the $\lambda' LQ\overline{D}$ term in their components, the corresponding part of the Lagrangian is

$$\begin{aligned} \mathcal{L}_{L_iQ_j\overline{D}_k} &= \lambda'_{ijk}\Big[-\tilde{e}_L^i u_L^j \bar{d}_R^k - e_L^i \tilde{u}_L^j \bar{d}_R^k - (\bar{e}_L^i)^c u_L^j \tilde{d}_R^{k*} \\ &\quad + \tilde{\nu}_L^i d_L^j \bar{d}_R^k + \nu_L \tilde{d}_L^j \bar{d}_R^k + (\bar{\nu}_L^i)^c d_L^j \tilde{d}_R^{k*}\Big] + \text{c.c.}. \end{aligned} \tag{2.45}$$

Each of the six terms corresponds to a different interaction vertex, which are shown in Fig. 2.13. With such vertices the resonant production of squarks becomes possible in *ep* collisions since the fusion of the initial electron and a quark from the proton allows for the formation of a squark [8].

For the nine possible $\lambda'_{1jk}$ couplings the corresponding squark production processes in $e^{\pm}p$ reactions are listed in Tab. 2.5. Given that antiquarks are less frequent than quarks in the proton, with an initial $e^+$ beam HERA is most sensitive to the couplings $\lambda'_{1j1}$ $(j = 1, 2, 3)$, where mainly $\tilde{u}_L^j$ squarks $(\tilde{u}_L, \tilde{c}_L, \tilde{t}_L)$ are being produced. In contrast, with

| $\lambda'_{1jk}$ | $\boldsymbol{e^+p}$ | | $\boldsymbol{e^-p}$ | |
|---|---|---|---|---|
| 111 | $e^+ + d \to \tilde{u}_L$ | $e^+ + \overline{u} \to \overline{\tilde{d}_R}$ | $e^- + u \to \tilde{d}_R$ | $e^- + \overline{d} \to \overline{\tilde{u}_L}$ |
| 112 | $e^+ + s \to \tilde{u}_L$ | $e^+ + \overline{u} \to \overline{\tilde{s}_R}$ | $e^- + u \to \tilde{s}_R$ | $e^- + \overline{s} \to \overline{\tilde{u}_L}$ |
| 113 | $e^+ + b \to \tilde{u}_L$ | $e^+ + \overline{u} \to \overline{\tilde{b}_R}$ | $e^- + u \to \tilde{b}_R$ | $e^- + \overline{b} \to \overline{\tilde{u}_L}$ |
| 121 | $e^+ + d \to \tilde{c}_L$ | $e^+ + \overline{c} \to \overline{\tilde{d}_R}$ | $e^- + c \to \tilde{d}_R$ | $e^- + \overline{d} \to \overline{\tilde{c}_L}$ |
| 122 | $e^+ + s \to \tilde{c}_L$ | $e^+ + \overline{c} \to \overline{\tilde{s}_R}$ | $e^- + c \to \tilde{s}_R$ | $e^- + \overline{s} \to \overline{\tilde{c}_L}$ |
| 123 | $e^+ + b \to \tilde{c}_L$ | $e^+ + \overline{c} \to \overline{\tilde{b}_R}$ | $e^- + c \to \tilde{b}_R$ | $e^- + \overline{b} \to \overline{\tilde{c}_L}$ |
| 131 | $e^+ + d \to \tilde{t}_L$ | $e^+ + \overline{t} \to \overline{\tilde{d}_R}$ | $e^- + t \to \tilde{d}_R$ | $e^- + \overline{d} \to \overline{\tilde{t}_L}$ |
| 132 | $e^+ + s \to \tilde{t}_L$ | $e^+ + \overline{t} \to \overline{\tilde{s}_R}$ | $e^- + t \to \tilde{s}_R$ | $e^- + \overline{s} \to \overline{\tilde{t}_L}$ |
| 133 | $e^+ + b \to \tilde{t}_L$ | $e^+ + \overline{t} \to \overline{\tilde{b}_R}$ | $e^- + t \to \tilde{b}_R$ | $e^- + \overline{b} \to \overline{\tilde{t}_L}$ |

TABLE 2.5: Squark production processes in $e^{\pm}p$ collisions.

an initial $e^-$ beam HERA is most sensitive to the couplings $\lambda'_{11k}$ ($k = 1, 2, 3$) and can mainly produce $\tilde{d}^k_R$ squarks ($\tilde{d}_R, \tilde{s}_R, \tilde{b}_R$). Thus the analysis of both $e^+p$ and $e^-p$ data gives sensitivity to all six squark flavors.

If $x$ denotes the momentum fraction of the proton carried by the interacting quark the invariant mass of the squark produced in $ep$ collisions is given by

$$m = \sqrt{xs}, \tag{2.46}$$

where $\sqrt{s}$ is the center of mass energy given in Eq. 2.9. Hence resonant squark production events will lead to a resonance peak in the $x$ distribution at $x = m^2/s$.

### Squark production cross section

The cross section for resonant squark production at HERA depends quadratically on the square of the Yukawa coupling $\lambda'_{ijk}$. For sufficiently small values of $\lambda'$ the cross section can be approximated by the Narrow Width Approximation (NWA) which leads to a $s$-channel production cross section for a scalar resonance in $e^+p$ and $e^-p$ collisions [33] of

$$\sigma(e^+p \to \tilde{u}^j_L + X) \propto \lambda'^2_{1jk} \cdot d^k \left( x = \frac{M^2_{\tilde{q}}}{s} \right) \tag{2.47}$$

$$\sigma(e^-p \to \tilde{d}^k_R + X) \propto \lambda'^2_{1jk} \cdot u^j \left( x = \frac{M^2_{\tilde{q}}}{s} \right). \tag{2.48}$$

Here $u^j(x)$ and $d^k(x)$ are the probabilities to find an up-type or down-type quark with momentum fraction $x$ in the proton. In the present analysis the production cross sections are obtained from the leading order amplitudes given in [33], corrected by multiplicative $K$-factors [34] to account for next-to-leading order QCD corrections. These $K$-factors increase the production cross section by $\mathcal{O}(10\,\%)$. $M^2_{\tilde{q}}$ is chosen as the hard scale at which

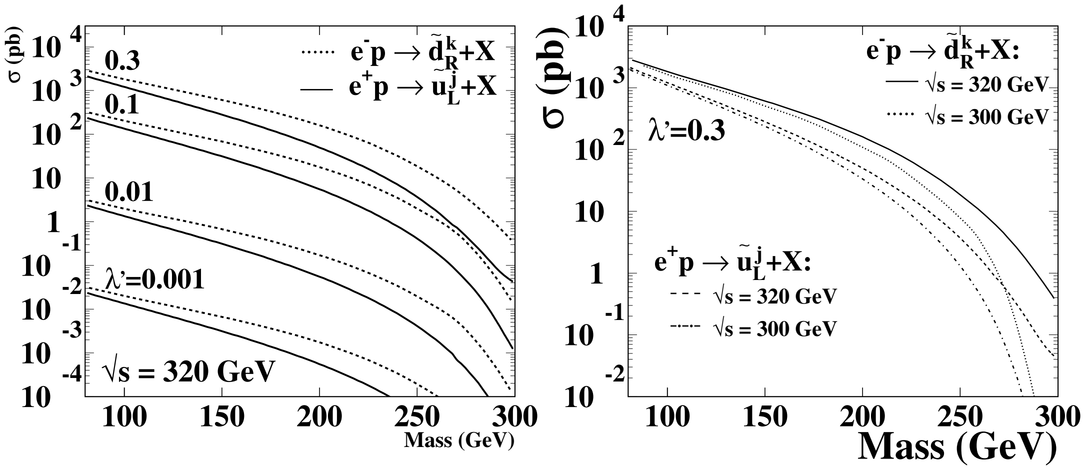


Figure 2.14: Cross section for resonant squark production in $e^{\pm}p$ collisions. Shown are the cross sections as a function of the squark mass for various values of the $\not R_p$ coupling $\lambda'$ (left) and for the two centre of mass energies of HERA (right).

the parton distributions are estimated. The systematic uncertainties on the signal cross section are discussed in Sec. 5.1.3.

The production cross sections for both $\tilde{d}_R^k$ and $\tilde{u}_L^j$ are illustrated in Fig. 2.14 (left) as a function of the squark mass for $\sqrt{s} = 320\,\mathrm{GeV}$. The cross sections are shown for various values of the $\not R_p$ coupling $\lambda'$. Since a $u$ quark from the proton is needed in $e^-p$, compared to the $d$ quark in $e^+p$, the cross section for squark production in $e^-p$ collisions is potentially larger than in $e^+p$ collisions. The difference between the two is approximately a factor of two for low masses, as naively expected. For higher masses the difference increases since the $u$ density in the proton is "harder". Both probabilities $u^j(x)$ and $d^k(x)$ are steeply falling at high $x$. For this reason the production cross section decreases drastically towards high squark masses for both $e^+p$ and $e^-p$ collisions. Due to this reduced cross section HERA is only sensitive to rather high values for the $\not R_p$ Yukawa coupling $\lambda'$ at high squark masses.

In the right panel of Fig. 2.14 the squark production cross section in $e^+p$ and $e^-p$ collisions is shown as a function of the squark mass for the two centre of mass energies of HERA. The cross section strongly depends on the centre of mass energies. For higher beam energies it is increased, particularly at high masses. Thus, with the increase of the centre of mass energy in $ep$ collisions at HERA in 1998 a new kinematic domain for squark production has been opened.

In general the intrinsic squark width is far below $1\,\mathrm{GeV}$ and the NWA is a good approximation. However, at high squark masses ($M_{\tilde{q}} \gtrsim 270\,\mathrm{GeV}$) the increased value of the Yukawa coupling leads to squark widths up to $5\,\mathrm{GeV}$. Here a correction of the NWA is applied since the steeply falling parton densities of the proton lead to kinematic effects which cannot be neglected. A discussion of the effects at high squark masses and their treatment is given in Sec. 8.3. The correction can be applied for squarks masses up

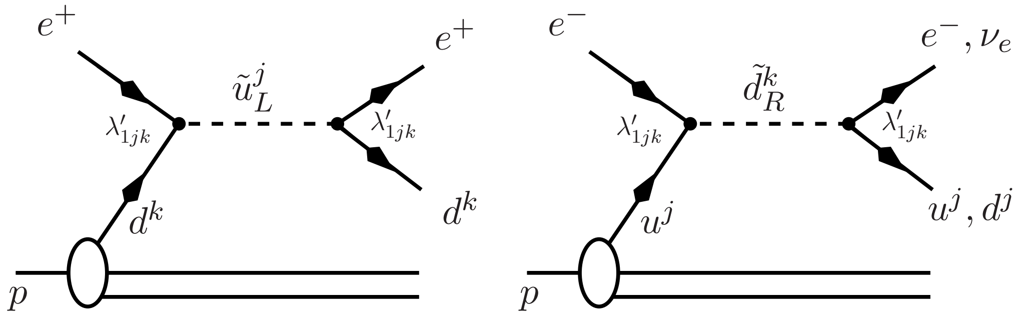


FIGURE 2.15: Feynman diagrams for $\not{R}_p$ squark production at HERA followed by $\not{R}_p$ squark decays for $\lambda'_{1jk} \neq 0$.

to 290 GeV. For even higher masses the correction is not adequate since interference effects of the directly $\not{R}_p$ squark decay modes with the SM processes cannot be neglected. In addition, the $u$ channel gets relatively more important. For this reason the analysis presented here considers masses below 290 GeV only.

If a non-vanishing $\lambda'_{131}$ is considered (leading to stop production in $e^+p$) and the mixing of the squark states is taken into account, the squark production cross section of Eq. 2.47 must be modified since in the Lagrangian of Eq. 2.45 only the "left" weak eigenstate $\tilde{u}^j_L$ occurs. Following from Eq. 2.32 the production cross sections of the two mass eigenstates $\tilde{t}_1$ and $\tilde{t}_2$ scale as $(\lambda'^2_{131} \cos^2\theta_t)$ and $(\lambda'^2_{131} \sin^2\theta_t)$, respectively.

In the case of sbottom production, the cross section must be modified in a similar way as for the stop. A non-vanishing $\lambda'_{113}$ could lead to sbottom production in $e^-p$ collisions. Eq. 2.48 gives the cross section for the "right" weak eigenstate. The production cross sections for the mass eigenstates $\tilde{b}_1$ and $\tilde{b}_2$ scale as $(\lambda'^2_{113} \sin^2\theta_b)$ and $(\lambda'^2_{113} \cos^2\theta_b)$ respectively.

### 2.5.2 $R_p$ violating squark decays

In addition to the squark decays of the MSSM (given in Eq. 2.36) additional modes occur if $R_p$ is violated by the $\lambda' LQ\overline{D}$ term. As can be seen from Eq. 2.45, the $\tilde{d}^k_R$, potentially produced in $e^-p$ collisions, can decay either into $e^- + u^j$ or $\nu_e + d^j$, while the $\tilde{u}^j_L$ which could be produced in $e^+p$ collisions decays into $e^+ + d^k$ only. The corresponding Feynman diagrams of production and decay are shown in figure 2.15. The final state consists of a jet and either an electron with high transverse momentum ($p_T$) or missing $p_T$.

The partial decay width for the $R_p$ violating squark decay modes is given by [33]

$$\Gamma_{\not{R}_p} = \frac{1}{16\pi} \lambda'^2_{1jk} M_{\tilde{q}}. \tag{2.49}$$

Compared to the squark mass this width is very small, e.g. for a squark mass of 250 GeV and a coupling of $\lambda'_{1jk} = 0.1$ it is $\Gamma_{\not{R}_p} = 50\,\mathrm{MeV}$.

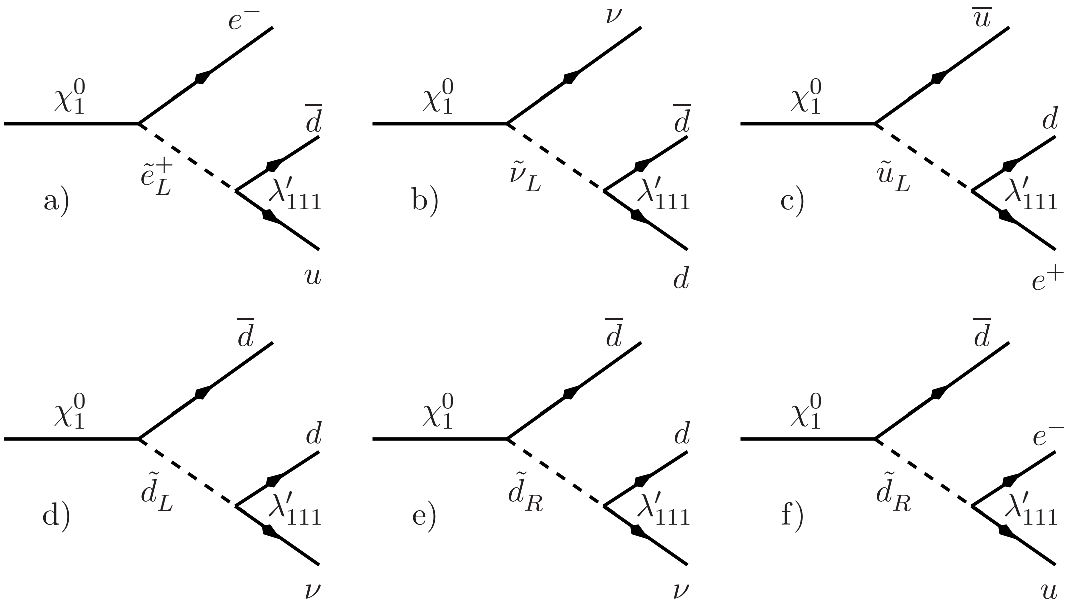


FIGURE 2.16: $\not{R}_p$ decay modes of the lightest neutralino $\chi_1^0$ for $\lambda'_{111} \neq 0$. The charge conjugate diagrams are not shown.

### 2.5.3 $R_p$ violating decays of neutralinos and charginos

New decay modes open up also for neutralinos and charginos if $R_p$ is violated by $\lambda'$ terms. In particular the $\chi_1^0$ (usually the LSP) is no longer stable, but decays to SM particles. The new $\chi_1^0$ decay modes for $\lambda_{111} \neq 0$ are shown in Fig. 2.16. The same decay modes exist for the heavier neutralino states.

The final states in the $\not{R}_p$ **neutralino** decay can be classified in three experimentally distinguishable groups: $\chi_i^0 \to \nu\bar{q}q$, $\chi_i^0 \to e^+\bar{q}q$ and $\chi_i^0 \to e^-\bar{q}q$. The probability for an $e^+$ and for an $e^-$ in the final state are the same[8]. This leads to very striking final states with a lepton of 'wrong'[9] charge which are free of SM background. The branching ratios (BR) of the $\chi_1^0$ strongly depend on its composition. The decay to charged leptons dominates if the neutralino is photino-like, whereas the decay to $\nu\bar{q}q$ is dominant for zino-like neutralinos.

In addition to the $R_p$ conserving gauge decays of **charginos**, charginos can decay to SM particles if $R_p$ is violated. The decays of the lightest chargino ($\chi_1^+$) involving one intermediate supersymmetric particle are shown in Fig. 2.17. The charginos can decay to $\nu_e\bar{q}q$ and $e\bar{q}q$ for which the electron/positron has the charge of the initial chargino. For charginos in a gauge decay of squarks produced in $ep$ collisions the electron/positron in the $\not{R}_p$ decay has always the same charge as the initial beam.

Heavy neutralinos $\chi_i^0$ with $i \geq 2$ as well as charginos (gluinos) usually undergo gauge decays conserving $R_p$ through a real or virtual boson or sfermion (squark) into a lighter

[8]The number of possible Feynman diagrams in Fig. 2.16 for $e^+\bar{q}q$ [diagram c) and charge conjugate of a) and f)] and $e^-\bar{q}q$ [diagram a) and f) and charge conjugate of diagram c)] are the same.

[9]'Wrong' means different with respect to the initial electron or positron beam.

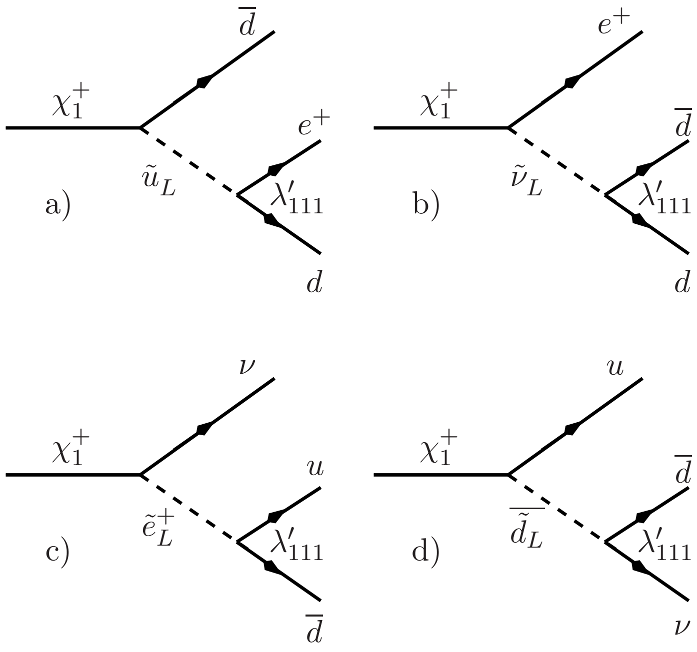


FIGURE 2.17: $R\!\!\!/_p$ decay modes of $\chi_1^+$ for $\lambda'_{111} \neq 0$.

gaugino (usually the LSP, $\chi_1^0$) and two fermions following Eq. 2.38, Eq. 2.39 and Eq. 2.40.

### 2.5.4 Possible final states

Considering the $R\!\!\!/_p$ decays and the gauge decays of squarks and taking into account the possible decay modes of the gauginos, we can classify the decay chains of $\tilde{u}_L^j$ and $\tilde{d}_R^k$ accessible in $e^-p$ and $e^+p$ collisions into nine event topologies which are shown in Tab. 2.6. This classification relies on the number of charged leptons and/or jets in the final state and on the presence of missing energy.

Selection channels labelled with $eq$ and $\nu q$ are the so called *lepton–quark decay* modes of the squark, proceeding directly via $R\!\!\!/_p$. The lepton–quark channels are most relevant at high Yukawa couplings $\lambda'$ as can be seen from Eq. 2.49. They contribute mostly at high squark masses, since here a large value of $\lambda'$ is required to obtain a measurable cross section (see Fig. 2.14).

The remaining selection channels cover the *gauge decays* of the squark where the $\tilde{u}_L^j$ ($\tilde{d}_R^k$) undergoes a gauge decay into $\chi^0$, $\chi^+$ or $\tilde{g}$ ($\chi^0$ or $\tilde{g}$). The final state will depend on their subsequent decays. The decay chain ends with the $R\!\!\!/_p$ decay of one sparticle, usually that of the LSP leading to a lepton of the first family and two quarks. Thus gauge decays are characterized by multijet (MJ) final states. Gauge decays involving one or two SUSY fermions are called *direct* or *cascade* gauge decays, respectively. Gauge decay channels leading to the final states labelled with $e^+MJ$, $e^-MJ$ and $\nu MJ$ in Tab. 2.6 can involve

| Channel | Decay processes | Signature |
|---|---|---|
| $\boldsymbol{eq}$ | $\tilde{q} \xrightarrow{\lambda'} e \quad q$ | high $p_T$ $e$ + 1 jet |
| $\boldsymbol{\nu q}$ | $\tilde{d}^k_R \xrightarrow{\lambda'} \nu_e \quad d$ | missing $p_T$ + 1 jet |
| $\boldsymbol{e^{\pm}MJ}$ | $\tilde{q} \longrightarrow q \quad X$<br>$\overset{\lambda'}{\hookrightarrow} e^{\pm}\bar{q}q$<br>$\tilde{q} \longrightarrow q \quad X$<br>$\hookrightarrow q\bar{q} \quad Y$<br>$\overset{\lambda'}{\hookrightarrow} e^{\pm}\bar{q}q$ | $e^{\pm}$ (both charges)<br>+ multiple jets |
| $\boldsymbol{\nu MJ}$ | $\tilde{q} \longrightarrow q \quad X$<br>$\overset{\lambda'}{\hookrightarrow} \nu\bar{q}q$<br>$\tilde{q} \longrightarrow q \quad X$<br>$\hookrightarrow q\bar{q} \quad Y$<br>$\overset{\lambda'}{\hookrightarrow} \nu\bar{q}q$<br>$\tilde{q} \longrightarrow q \quad X$<br>$\hookrightarrow \nu\bar{\nu} \quad Y$<br>$\overset{\lambda'}{\hookrightarrow} \nu\bar{q}q$ | missing $p_T$<br>+ multiple jets |
| $\boldsymbol{e\ell MJ}$ | $\tilde{q} \longrightarrow q \quad X$<br>$\hookrightarrow \ell\nu_{\ell} \quad Y$<br>$\overset{\lambda'}{\hookrightarrow} e^{\pm}\bar{q}q$<br>$\tilde{q} \longrightarrow q \quad X$<br>$\hookrightarrow \ell^{+}\ell^{-} \quad Y$<br>$\overset{\lambda'}{\hookrightarrow} e^{\pm}\bar{q}q$<br>$\tilde{q} \longrightarrow q \quad X$<br>$\hookrightarrow e^{+}e^{-} \quad Y$<br>$\overset{\lambda'}{\hookrightarrow} \nu\bar{q}q$ | $e$<br>+ $\ell$ ($e$ or $\mu$)<br>+ multiple jets |
| $\boldsymbol{\nu\ell MJ}$ | $\tilde{q} \longrightarrow q \quad X$<br>$\hookrightarrow \ell\nu_{\ell} \quad Y$<br>$\overset{\lambda'}{\hookrightarrow} \nu\bar{q}q$<br>$\tilde{q} \longrightarrow q \quad X$<br>$\hookrightarrow \nu\bar{\nu} \quad Y$<br>$\overset{\lambda'}{\hookrightarrow} e\bar{q}q$<br>$\tilde{q} \longrightarrow q \quad X$<br>$\hookrightarrow \mu^{+}\mu^{-} \quad Y$<br>$\overset{\lambda'}{\hookrightarrow} \nu\bar{q}q$ | $\ell$ ($e$ or $\mu$)<br>+ missing $p_T$<br>+ multiple jets |

Table 2.6: Squark decay channels in $\not{R}_p$ SUSY classified by distinguishable event topologies. $X$ and $Y$ denote a neutralino, a chargino or a gluino.

one or two SUSY fermions ($\chi$ or $\tilde{g}$) denoted by $X$ and $Y$ in Tab. 2.6. The final states $e\ell MJ$ and $\nu\ell MJ$ are necessarily cascade decays and involve two SUSY fermions.

In most of the parameter space a "left" squark[10] decays in a cascade gauge decay to the lightest chargino $\chi_1^\pm$ conserving $R_p$ (see Sec. 2.4.1). This in turn decays to lighter gauginos states and leads to cascade gauge decays which could contribute significantly in $e^+p$ collisions. The cascade decay chains involving $\chi_1^\pm$ and $\chi_1^0$ have usually the highest branching ratios (BR). However, all combinations of gauginos in the cascade decay chain are possible, if they are kinematically allowed and not forbidden from e.g. charge conservation. In contrast the couplings of a "right" squark[11] to charginos are suppressed. Thus the cascade decays of squarks in $e^-p$ collisions can only proceed via two neutralinos and usually have small BRs.

Decay patterns involving more than two $\chi$ or $\tilde{g}$ are kinematically suppressed and are therefore not explicitly searched for. Decay channels involving taus are also not explicitly analysed. In the mass range considered here the sum of BRs of the considered channels is close to 100 % for almost all SUSY scenarios as is demonstrated in Chap. 8. Cases where the $\chi_1^0$ has such a long lifetime that displaced decay vertices are expected have not been considered since the region of parameter space that allows a $\chi^0$ to escape detection for a finite value of the $\not{R}_p$ coupling is very strongly constrained by the searches for charginos carried out at LEP [15]. Decays of $\chi$'s into a Higgs boson (see Eq. 2.38 and 2.39) are taken into account in the calculation of the BRs of the cascade decays of $eMJ$ and $\nu MJ$, when the Higgs decays into hadrons. The contribution of these decays is however very small.

## 2.6 Analysis strategy

To fully exploit the sensitivity of HERA for resonant squark production in $\not{R}_p$ supersymmetric models, all final state topologies of Tab. 2.6 must be investigated. In Chap. 5, Chap. 6 and Chap. 7 the event selection of the different topologies are described. The lepton–quark final states ($eq$ and $\nu q$) are investigated separately. For final states with an electron or positron and multiple jets ($e^+MJ$, $e^-MJ$, $eeMJ$, $e\mu MJ$, $e\nu MJ$) a common preselection has been carried out and the subchannels are then analyzed sparately. The same is true for final states with a neutrino and multiple jets ($\nu MJ$ and $\nu\mu MJ$). For all final state topologies the selection is performed in such a way that signal-like events are separated from the SM background; events hypothetically coming from squark decays are selected while the SM background is reduced. To evaluate the background expectation in all selection channels predicted by the SM, a large number of Monte Carlo (MC) events has been simulated for all relevant SM processes (Sec. 2.7). Experimental as well as theoretical uncertainties (Sec. 4.7) lead to an error on the SM expectation.

For the limit derivation (see below) an exclusive selection is needed: One event (data, background and signal) is allowed to be selected in one selection channel only. Otherwise the calculation of exclusion limits is not correct since e.g. a hypothetical signal is counted twice. For this reason a possible overlap between the event samples of different selection channels is forbidden. This has been assured by the selection cuts of the different final state topologies.

[10] e.g. the $\tilde{u}_L, \tilde{c}_L, \tilde{t}_L$, which could be produced violating $R_p$ in $e^+p$ collisions

[11] e.g. the $\tilde{d}_R, \tilde{s}_R, \tilde{b}_R$ potentially produced in $e^-p$ collisions

The results of the data selection are then compared to the SM prediction. For topologies where the number of selected events is considerable the mass of the hypothetical squark is reconstructed and the mass spectra of data and SM MC are differentially compared. For selection channels with low statistics the total event numbers are compared to the SM expectation. If no significant deviation from the SM is found, the results of the selection can be used to set exclusion limits on the parameters of various SUSY models (Chap. 8).

To derive exclusion limits the efficiencies to select events from the squark signal must be determined. To avoid the simulation of signal events at many points in the supersymmetric parameter space, the efficiencies have been determined for each decay mode separately as a function of the particle masses involved in the decay chain (see Sec. 2.7). This mass dependent parameterisation of the signal efficiencies allows an interpretation in a large parameter range for various SUSY models with a finite, however still very large number of signal events to be simulated.

For a given set of SUSY parameters in a certain model the branching ratios of the decay modes and the masses of the supersymmetric particles are calculated. The selection efficiencies for each decay mode are retrieved from the mass spectrum. The number of observed and expected events, the branching ratios of the squark decay modes and the selection efficiencies are used to calculate an upper limit on the number of events coming from squark production. This limit is translated into a limit on the production cross section. In a given supersymmetric model, parameter space points are excluded which lead to a production cross section higher than the calculated limit. Since always several SUSY parameters are relevant, a multi-dimensional scan of the SUSY parameter space is carried out.

## 2.7 Simulation of SM processes and SUSY signal

### SM background processes

To determine the expectation of SM background processes in the selection of the various squark decay channels, for each possible SM background source a sample of Monte Carlo events is used corresponding to a luminosity of more than 10 times that of the data.

The determination of the background contribution coming from NC DIS is performed using two Monte Carlo samples which employ different models of QCD radiation. The first was produced with the DJANGO [35] event generator which includes QED first order radiative corrections. QCD radiation is implemented using ARIADNE [36] based on the Colour Dipole Model (CDM) [37]. This sample is chosen to estimate the NC DIS contribution in the $eq$ channel of Tab. 2.6. The second sample was generated with the program RAPGAP [38], in which QED first order radiative corrections are implemented as described above. RAPGAP includes leading order QCD matrix elements. Higher order radiative corrections are modelled by leading-log parton showers (matrix elements and parton shower model, MEPS) [39]. This sample is used to determine NC DIS background in the final states with electron and multiple jets, as RAPGAP better describes this particular final state configuration at high $Q^2$ (see Sec. 6.1.2 for details). For both samples the parton densities functions (PDF) in the proton are taken from the CTEQ5L [40] parameterisation. Hadronisation is performed in the Lund string fragmentation scheme using JETSET [41].

The modelling of the CC DIS process is performed using the DJANGO program with CTEQ5L structure functions. Direct and resolved photoproduction processes ($\gamma p$) of light and heavy quark flavours including prompt photon production are generated with the PYTHIA [42] event generator which relies on first order matrix elements and uses leading-log parton showers and string fragmentation [41]. The photon PDF are taken from [43]. The SM prediction for the production of heavy gauge bosons via $ep \rightarrow eW^{\pm}X$ and $ep \rightarrow eZX$ is calculated with EPVEC [44].

### SUSY signal

For the simulation of the SUSY signal we use two different event generators: for the lepton–quark channels ($eq$ and $\nu q$), proceeding directly via $\not{R}_p$, the event generator LEGO [45] is used, whereas the gauge decays of squarks are simulated using SUSYGEN [46, 47]. LEGO takes into account initial QED radiation in the collinear approximation. In both LEGO and SUSYGEN, initial and final state parton showers are simulated according to the DGLAP [39] evolution equations. String fragmentation [41] is used for the non-perturbative part of the hadronisation. The squark mass is chosen for the maximum virtuality of parton showers initiated by a quark coming from the squark decay. Moreover, in the SUSYGEN generator, the parton showers modelling QCD radiation off quarks emerging from a $\chi$ or $\tilde{g}$ decay are started at a scale given by the mass of this sparticle.

To allow a model independent interpretation of the results, the signal efficiencies are parameterised for each decay chain separately as a function of the masses of the supersymmetric particles involved in the squark decay chain. For the lepton–quark decay channels the only supersymmetric particle involved is the squark. Thus, the efficiencies of these decay modes have been determined by simulating several event samples of 10 000 events from lepton–quark decays for various squark masses. The efficiency is then parameterized as a function of the squark mass.

For direct gauge decays the mass of the squark and one gaugino are relevant. Direct gauge decays can proceed via all gaugino states. However, the kinematics of the final state depend predominantly on the mass of the gaugino and only weakly on its type since all gauginos have the same spin ($\frac{1}{2}$). Therefore the efficiencies of all direct gauge decays are determined by only investigating the direct decay chain with the lightest neutralino $\chi_1^0$ being the intermediate gaugino. In a dense grid of squark and $\chi_1^0$ masses covering the large SUSY parameter space considered in this analysis the selection efficiencies are determined. A mass dependent parameterisation of the efficiency is then obtained which is valid for all gaugino types in direct gauge decays.

The same simplification can be used in the case of cascade gauge decays where the squark mass and two gaugino masses are relevant. Here the efficiencies are determined for the particular decay chain involving the lightest chargino $\chi_1^{\pm}$ and the lightest neutralino $\chi_1^0$ which usually has the highest BR compared to the other cascade gauge decays. In a dense grid of the three masses ($\tilde{q}$, $\chi_1^{\pm}$, $\chi_1^0$) the efficiencies are determined. Again, the derived efficiency can be used for all gaugino combinations in the decay chain. For cascade decay modes where the chargino-neutralino combination is not possible due to e.g. charge conservation, the decay chain involving the $\chi_2^0$ and the $\chi_1^0$ is used. The small grid size of the two (direct) or three (cascade) masses involved in the gauge decay process requires to simulate a huge number of signal events. For this reason the number of simulated events of each mass configuration is restricted to 1 000 for all gauge decay processes.

The efficiencies have been explicitly determined for the production process $e^+ + p \rightarrow \tilde{u}_L + X$ followed by a certain squark decay mode. However, the efficiencies of this decay mode can also be used for the reaction $e^- + p \rightarrow \tilde{d}_R + X$ followed by the same decay mode since it is expected that the selection efficiencies dominantly depend on the mass configuration as far as the charges of the final state particles are not considered. For the $e^+MJ$ and $e^-MJ$ channels where the charge of the electron/positron is relevant this aspect has been properly taken into account.

The intrinsic width of the squark, which could in principle have an effect on the efficiencies, is in general negligible compared to the experimental resolution. In most of the SUSY parameter space the squark width is far below 1 GeV. For this reason in the event generation of all squark decay channels the squark width is set to values which do not affect the selection efficiencies. However, very high Yukawa couplings $\lambda'$ could lead to a deviation from this assumption. These cases are important at very high squark masses near to the kinematic border given by the centre of mass energy. Here the efficiencies must be corrected (cf. Sec. 8.3) and the corrections are taken into account in the limit calculation.

# Chapter 3

# The H1 Experiment at HERA

In this chapter the electron-proton collider HERA[1] at DESY [2] in Hamburg and the H1 experiment are introduced. After a brief description of the HERA storage rings, an overview of the H1 detector is given, concentrating on the components which are most relevant to this analysis. For a detailed description see [48].

## 3.1 The HERA collider

The HERA collider is located at the DESY laboratory in Hamburg, Germany. It has been operational since 1992. This accelerator is the first to store and collide different particle species (electrons and protons). The two storage rings, one for electrons and one for protons, have a circumference of 6.3 km and are situated in a tunnel about $10 - 15$ m below the surface.

The two beams are collided at two interaction regions (north and south). Around these points the experiments H1 and ZEUS are constructed to study *ep* collisions. In addition, there are two fixed target experiments HERMES (east) and HERA-B (west) which make use of the HERA beams. The HERMES experiment, operating since 1995, studies interactions of polarised beam electrons with polarised gas targets ($H_2$, D, He) in order to investigate the spin structure of nucleons. The HERA-B experiment was commissioned in 2000. It is a forward spectrometer which studies the production of heavy flavour quarks in interactions between protons from the halo of the HERA proton beam and nucleons of an internal wire target.

The location of the four experiments are shown in Fig. 3.1 together with the complete HERA collider complex and its pre-accelerator system. After several accumulation and acceleration steps the electrons and protons are injected into the HERA rings. They are stored in up to 220 bunches of $10^{10}$ to $10^{11}$ particles each circulating in opposite directions in the ring where they are accelerated to their final energy. The time interval between two consecutive bunches is 96 ns.

In 1994–97 HERA ran with positrons ($e^+$) of final beam energy $E_e^0 = 27.5\,\mathrm{GeV}$ and protons of final energy $E_P = 820\,\mathrm{GeV}$. In 1998 the proton beam energy was increased to $E_P = 920\,\mathrm{GeV}$ and HERA was operated with electrons ($e^-$) . Between summer 1999 and

[1] Hadron-Elektron-Ring-Anlage
[2] Deutsches Elektronen-Synchrotron

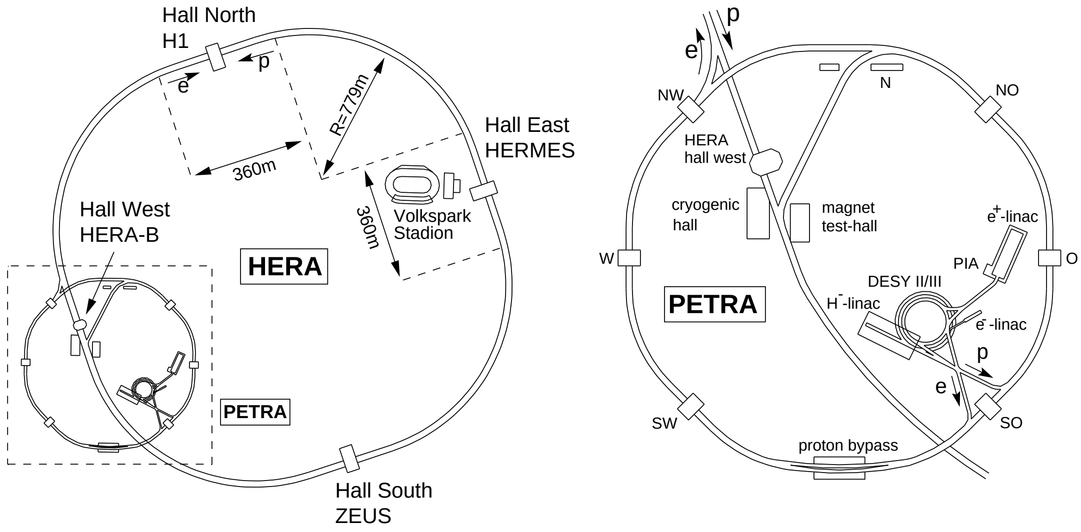


Figure 3.1: Schematic overview of the HERA accelerator complex at DESY with an enlarged view of the pre-accelerator system (left).

autumn 2000 positrons were again stored in HERA. Following from Eq. 2.9 the energy in the center-of-mass system at HERA is

$$\sqrt{s} \approx \sqrt{4E_eE_p} \approx 320 \ (300) \ \text{GeV} \quad \text{for } E_p = 920 \ (820) \ \text{GeV} \ . \tag{3.1}$$

For this analysis all data taken at $\sqrt{s} = 320\,\text{GeV}$ in 1998/1999 (with an initial $e^-$ beam) and 1999/2000 (with an initial $e^+$ beam) are used[3].

By the year 2000, the peak electron and proton currents routinely reached values up to $I_e = 50\,\text{mA}$ and $I_p = 110\,\text{mA}$, resulting in a peak luminosity of up to

$$\mathcal{L} = 1.5 \cdot 10^{31}\,\text{cm}^{-2}\,\text{s}^{-1}. \tag{3.2}$$

In September 2000, HERA operation was stopped to undertake a major upgrade of the HERA accelerator and the experiments. New super-conducting quadrupole magnets were inserted close to the H1 and ZEUS interaction regions. They enable a better focussing of the beams in the interaction region and therefore should lead to a not yet reached luminosity $4-5$ times higher than before. In addition spin rotators were inserted before and after the interaction regions to provide an longitudinally polarised electron beam.

## 3.2 The H1 detector

The H1 detector is situated in the North Hall of HERA. It is designed as a multi-purpose detector to study high-energy electron-proton collisions. It provides almost hermetic coverage in solid angle ($4\pi$) around the beam axis with some unavoidable acceptance losses

[3]Data taken up to 1997 at $\sqrt{s} = 300\,\text{GeV}$ are not considered in this work. The reasons are discussed in detail in Sec. 4.3.

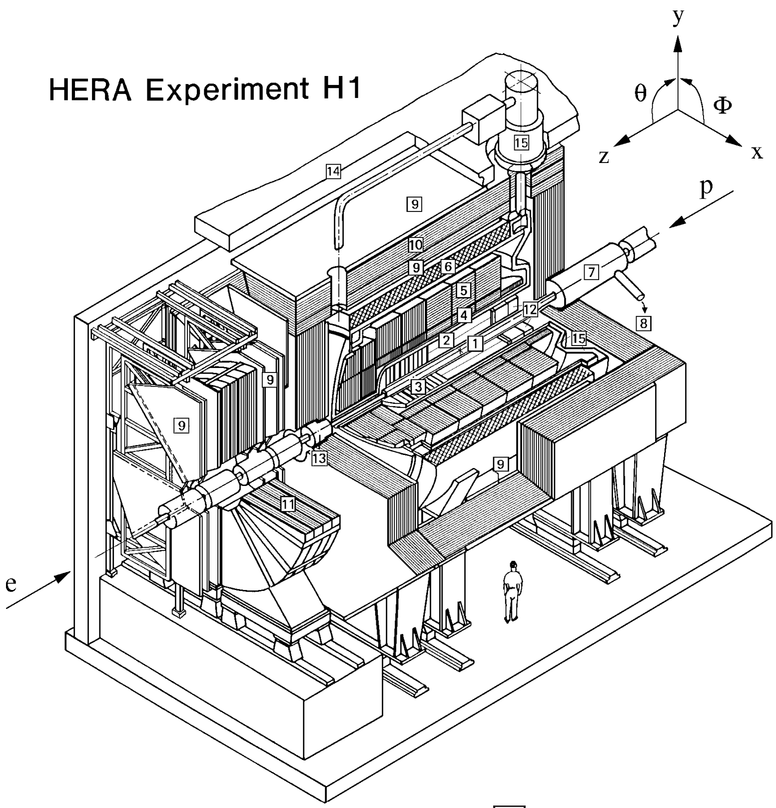


| | |
|---|---|
| 1 | beam pipe |
| 2 | central tracking chambers |
| 3 | forward tracking chambers |
| 4 | electromagnetic LAr calorimeter (lead) |
| 5 | hadronic LAr calorimeter (stainless steel) |
| 6 | superconducting solenoid |
| 7 | compensating magnet |
| 8 | He cooling |
| 9 | muon chambers |
| 10 | instrumented iron |
| 11 | muon toroidal magnet |
| 12 | warm calorimeter (SPACAL) |
| 13 | forward calorimeter |
| 14 | concrete shielding |
| 15 | cryostat |

Figure 3.2: The H1-Detector.

due to the feed through of the beam pipe. The H1 apparatus fills a volume of roughly $1\,800\,\mathrm{m}^3$ and weighs about 2 800 tonnes.

Fig. 3.2 shows an isometric view of the detector. Electrons enter from the left, protons from the right Since the centre of mass system of the *ep* collisions at HERA is boosted along the proton direction, the H1 detector is considerably more massive and highly segmented in this direction.

To measure the properties of the complete final state, the H1 detector resembles the typical layout of modern collider detectors. Starting the description outward from the interaction vertex, the detector consists of a central and a forward tracking system with drift chambers and trigger proportional chambers. They are used to measure trajectories and momenta of charged particles. The tracking system is surrounded by the liquid argon cryostat which houses the electromagnetic and hadronic calorimeters. These are used to identify electrons and hadrons and to measure the energy and the position of neutral and charged particles. A superconducting cylindrical coil with a diameter of 6 m and a length of 5.75 m provides the analysing field parallel to the beam axis. This allows the determination of the transverse momenta of charged particles by the tracking system. The iron return yoke of the magnet is laminated and filled with limited streamer tubes. They provide a measurement of hadronic energy leaking beyond the main calorimeter. In addition, muon tracks are identified and their direction is measured. Muon identification further benefits from additional chambers inside and outside of the iron and from a toroidal magnet sandwiched between drift chambers in the forward direction.

### 3.2.1 The H1 coordinate system

Points within the H1 detector are described using a cartesian coordinate system ($x$, $y$, $z$) in which the nominal interaction point of $ep$ interactions defines the origin, $x$ is the direction towards the centre of the HERA ring, $y$ is the upward direction and $z$ points in the momentum direction of the proton beam[4]. The $(x, y)$-plane is referred to as the transverse plane. The polar and azimuthal angles are defined correspondingly, so that the polar angle is $\theta = 0°$ in the proton momentum direction and $\theta = 180°$ in the electron direction. The azimuthal angle $\phi = 0°$ points along the $x$-direction.

The *pseudorapidity* $\eta$ is often used instead of the polar angle $\theta$ for ultra-relativistic particles. It is defined as

$$\eta = -\ln \tan \frac{\theta}{2}. \tag{3.3}$$

This variable has the benefit that it transforms linearly under Lorentz boosts along the $z$-axis.

### 3.2.2 Tracking

The tracking system (Fig. 3.3) of H1 simultaneously provides track triggering, reconstruction and particle identification. It covers the angular range $5° < \theta < 178°$ with full azimuthal acceptance. Because of the asymmetry between the electron and proton beam energies many particles are produced at relatively small angles $\theta$. To maintain good efficiency for triggering and reconstruction the system is divided between the central and the forward region.

The superconducting magnet solenoid, surrounding the tracking system and the Liquid Argon calorimeter (LAr), creates a homogeneous magnetic field of about 1.15 Tesla parallel to the $z$-axis. In this field charged particles are forced on curved tracks in the $(x, y)$-plane enabling a measurement of the transverse momentum $p_T$ of the particle.

#### The Central Tracking Chambers

The central tracking system covers the region $15° < \theta < 165°$ and consists of concentric drift and proportional chambers. Fig. 3.4 shows a radial view of these roughly cylindrical shaped detectors around the beam pipe:

[4]In the following the electron momentum direction is referred to as the backward direction, and the proton momentum direction as the forward direction.

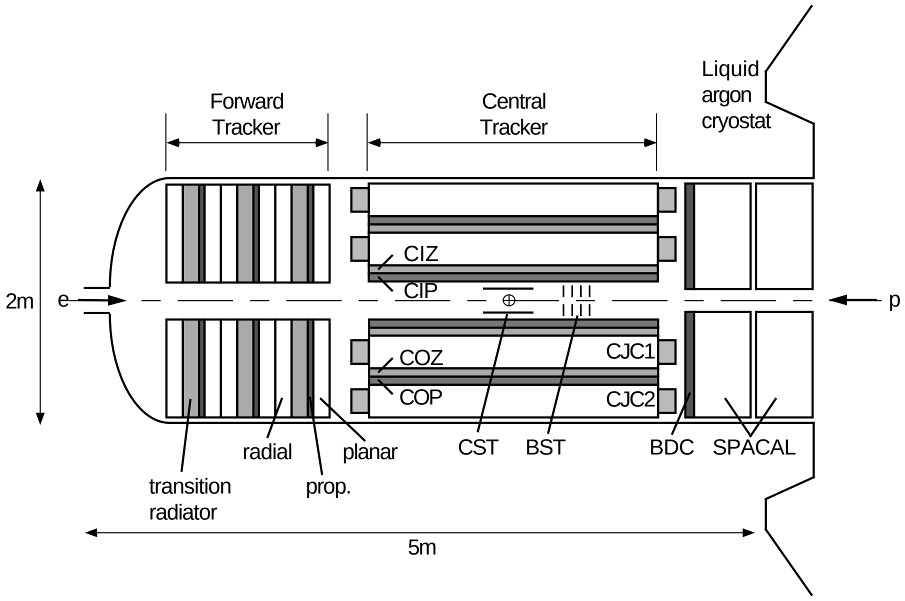


Figure 3.3: Longitudinal section of the H1 tracking system.

- The innermost part of the H1 detector, the Central Silicon Tracker (CST), consists of two layers of silicon strip detectors with radii of $r = 5.75$ cm and $r = 9.75$ cm. It measures two points of the track trajectories very accurately ($\sigma_{r\phi} = 12\,\mu$m, $\sigma_z = 22\,\mu$m). This precision is exploited to identify secondary decay vertices resulting from the decay of long-lived particles with decay lengths of a few hundred micrometers.

- The inner and outer multi wire proportional chambers (CIP and COP), each consisting of two detector layers, deliver fast timing signals with a resolution of 21 ns. They are used to trigger on tracks coming from a nominal interaction vertex.

- The two large concentric drift chambers (CJC 1 and CJC 2) have a length of 2.2 m. CJC 1 (CJC 2) consists of 30 (60) cells with 24 (32) sense wires, strung parallel to the beam axis. Its inner radius is 20.3 (53.0) cm and its outer radius 45.1 (84.4) cm, respectively. The drift cells are inclined by about 30° with respect to the radial direction so that stiff tracks pass through more than one cell, aiding the track position resolution, and eliminating reconstruction ambiguities by linking track segments from different cells. The wire signal induced by a charged particle allows the measurement of the $r - \phi$ coordinate with a resolution of $\sigma_{r\phi} \approx 140\,\mu$m, while the measurement of $z$ using a charge division method has a rather coarse precision ($\sigma_z \approx 2.2$ cm). For tracks passing through all layers of the CJC an effective momentum resolution of $\sigma(p_T)/p_T \approx 0.01 \cdot p_T(\mathrm{GeV})$ has been achieved.

- The resolution in $z$ is much improved by two thin central $z$-chambers (CIZ and COZ) surrounding the beam pipe and the inner half of the jet chambers, respectively. These chambers have an orientation of sense wires and drift field orthogonal to that of the jet chambers: their sense wires are strung in the $(r, \phi)$-plane and their drift field is

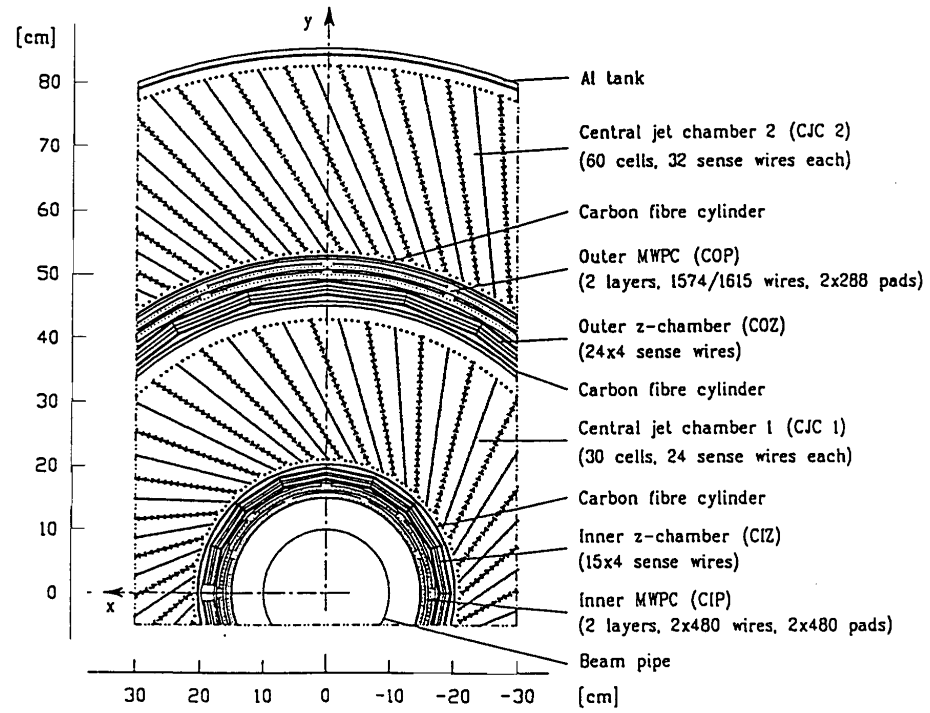


Figure 3.4: Transverse section through the tracking system.

along the $z$ direction. This allows an accurate measurement of the $z$ coordinate from drift time measurements with a typical resolution of $300\,\mu$m.

### The Forward Tracking Chambers

The Forward Track Detector (FTD) is shown in the left-hand part of Fig. 3.3. It consists of three identical *super-modules* aligned around the $z$-axis. Each super-module consists of four parts: The planar drift chambers are located closest to the central tracker since its homogenous spatial precision in $x$ and $y$ is most suitable for linking tracks in the centre. The planars are designed to provide accurate $\theta$ measurements. The forward multi wire proportional chamber (FWPC) is mounted directly behind the planars since it shares the same gas mixture. Behind the FWPC particles transverse a transition radiator of 400 polypropylene foils, producing transition radiation photons which are detected in the radial chamber of each supermodule. The radials also provide accurate $r-\phi$ information and a moderate radial measurement by charge division. To improve track position resolution the second and third radial modules are rotated by 3.75° and 2.5° relative to the first. The performance of the forward track detector is degraded due to a large amount of secondary tracks produced in the dead material in front of the system.

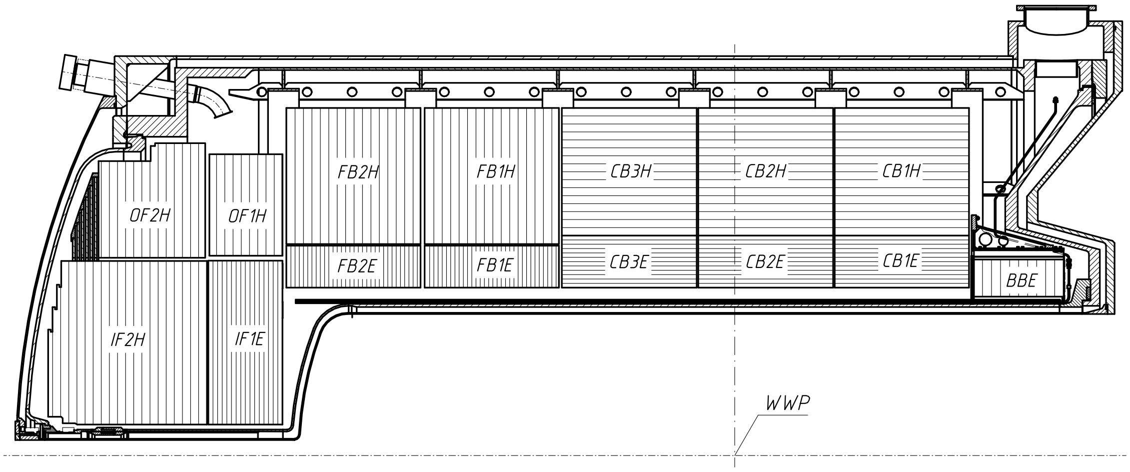


Figure 3.5: Longitudinal section of the Liquid Argon Calorimeter.

### 3.2.3 Calorimetry

The requirements of identification and precise measurement of electrons, muons, neutral particles and jets are best met by a Liquid Argon Calorimeter (LAr) inside the superconducting coil. This *large coil solution* minimizes both the amount of dead material in front of the calorimeter and the overall size and weight of the calorimeter. The LAr provides energy measurement in the polar angular range $4^\circ < \theta < 154^\circ$ with full azimuthal acceptance. The polar coverage is completed with a small calorimeter in the proton direction (PLUG) and the spaghetti calorimeter (SPACAL) in the backward region.

#### The Liquid Argon Calorimeter

The Liquid Argon Calorimeter is the most important detector for measuring the energies of the final state particles from $ep$ interactions. It is a sampling calorimeter which is located in a cryostat. The LAr is segmented along the $z$-axis into eight wheels (see Fig. 3.5), called BBE, CB1, CB2, CB3, FB1, FB2, OF and IF. Each wheel is further divided in the azimuthal direction into eight identical octants (see Fig. 3.6 for the central region) and consists of an inner electromagnetic and an outer hadronic section [5]. The small regions between octants and wheels are called $\phi$-cracks and $z$-cracks respectively.

From inside to outside, the LAr is built up of absorber plates interleaved with LAr interspaces. The electromagnetic part consists of 2.4 mm thick lead absorber plates supplemented with high voltage and readout. The 2.35 mm gaps are filled with liquid Argon as active material. Depending on the polar angle $\theta$, the depth of the electromagnetic section corresponds to $20-30$ radiation lengths. The hadronic section consists of 19 mm stainless steel absorber plates with a double gap of 2.4 mm filled with liquid Argon. This corresponds in total to 5 to 8 nuclear interaction lengths including the electromagnetic section.

[5]With exception of the BBE which has an electromagnetic section only.

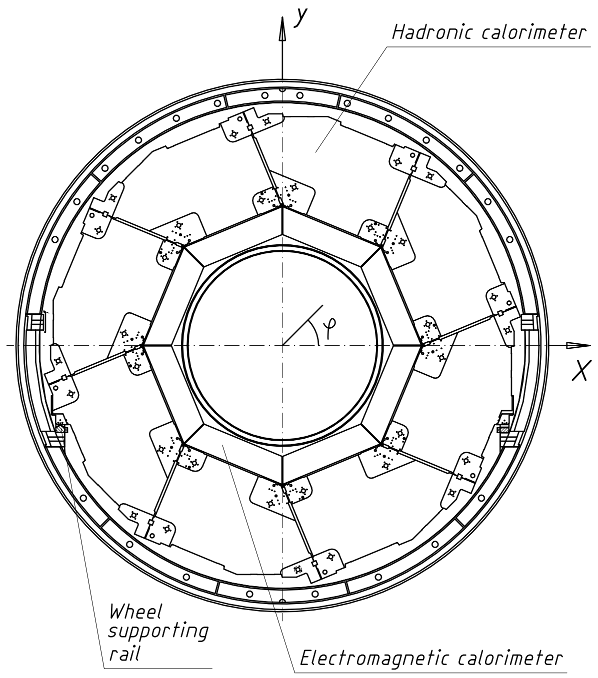


Figure 3.6: Transverse section of the Liquid Argon Calorimeter.

The orientation of the absorber plates was chosen to guarantee that the angle of incidence of particles originating from the *ep* interaction point is always larger than 45°. The basic transverse granularity of the electromagnetic readout cells is about 3 cm. In BBE, CB1 and CB2 the cell sizes are roughly doubled. Longitudinally, the number of segments increases from three for the barrel region to six in the forward region. In the hadronic part the number of segments increases from three (barrel) to six (forward). The total number of read-out channels is about 45 000. This fine granularity allows for a precise spatial measurement of electromagnetically interacting particles and an effective separation of electromagnetic and hadronic showers.

The energy resolution for electromagnetic interacting particles was determined from test beam measurements to be [49]

$$\sigma(E_{\mathrm{e.m.}})/E = 11\,\%/\sqrt{E/\mathrm{GeV}} \oplus 1\,\%. \tag{3.4}$$

The calorimeter is *non compensating*, meaning the response to hadrons is smaller than for electrons of same energy (about 30 % at 10 GeV). This effect is corrected offline using a weighting technique based on a shower shape analysis. The energy resolution for hadrons is

$$\sigma(E_{\mathrm{had.}})/E = 50\,\%/\sqrt{E/\mathrm{GeV}} \oplus 2\,\%. \tag{3.5}$$

### The SPACAL calorimeter

Calorimetric information in the backward region is provided by a scintillating fibre *spaghetti* calorimeter (SPACAL) with lead absorbers and photo-multiplier readout. The

SPACAL covers the polar angle range of $153° < \theta < 177.8°$. Its main task is to measure the energy and the position of the scattered electron in DIS events with $1 < Q^2 < 150\,\mathrm{GeV}^2$.

The SPACAL consists of an inner electromagnetic and an outer hadronic part. The electromagnetic part has a depth of 28 radiation lengths. The small transverse cell size of $(40.5\,\mathrm{mm})^2$ ensures a good position measurement. In total 1328 channels are read out with a time resolution of 1 ns. This excellent timing information is used to provide time-of-flight information for energy depositions in the SPACAL. The electromagnetic energy can be measured with a resolution of $\sigma_E/E = (7.1 \pm 0.2)\,\%/\sqrt{E/\mathrm{GeV}} \oplus (1.0 \pm 0.1)\,\%$, as obtained in test beam measurements. For the relevant energy range of the scattered electron, the absolute energy scale is known with a precision better than 1 %.

In the hadronic part of the calorimeter the transverse cell size is $(119\,\mathrm{mm})^2$ and 136 channels are read out in total. Energies are measured with a resolution of $\sigma_E/E = 30\,\%/\sqrt{E/\mathrm{GeV}}$. The total length of electromagnetic and hadronic section correspond to 2 nuclear interaction lengths.

### 3.2.4 The Muon System

The Muon System of the H1 detector consists of the Central Muon Detector and the Forward Muon Detector. The main purpose of these detectors is to identify tracks from muons and to measure their direction and momentum.

#### Central Muon Detector

The Central Muon Detector consists of a iron structure which also acts as a return yoke for the solenoid. This structure is instrumented with streamer tubes. The detector is formed by a octagonal barrel and is terminated by two flat endcaps giving an angular coverage of $5° \leq \theta \leq 171°$. The detector is built up in a sandwich structure with 10 iron plates of 7.5 cm thickness, interleaved with limited streamer tubes. To either side of the iron yoke three additional streamer tube layers are attached. These *muon boxes* improve the track measurement and cover the edges of the detector. The resolution of the position measurement perpendicular to the signal wires inside the streamer tubes varies from 3 mm to 4 mm. In the barrel region the wires are oriented along the $z$-axis, while the orientation follows the $x$-axis in the endcaps. To measure the position parallel to the signal wires, five of the layers are equipped with strip electrodes, which achieve a resolution of 10 mm to 15 mm. Efficiencies of up to 80 % are reached for single layers.

#### Forward Muon Detector

The Forward Muon Detector is located outside the main detector between 6.4 m and 9.4 m forward of the nominal interaction point. It consists of six double layers of drift chambers on both sides of a toroid magnet providing a field of 1.5 Tesla. The detector covers the polar angular range $4° \leq \theta \leq 17°$. Due to energy loss in the inner detectors and in the toroid, only muons with momenta $p > 5\,\mathrm{GeV}$ can be identified with this detector.

### 3.2.5 Luminosity Measurement and Time-of-Flight-System

An essential ingredient for any analysis in high-energy physics is the precise determination of the integrated luminosity to which the accumulated data correspond. At HERA the luminosity is measured with the Bethe-Heitler process:

$$ep \rightarrow e\gamma p. \tag{3.6}$$

The cross section of this reaction is large and well known theoretically. Since the angular distribution for both the scattered electron and the photon are strongly peaked in the direction of the electron beam, the detectors must be placed close to the beam pipe and far from the interaction region in order to cover these small angles.

The two principal components of the luminosity system are the electron tagger (ET), located close to the electron beam pipe at $z = -33.4$ m, and the photon detector (PD) at $z = -102.9$ m, in the direction of the incident electron beam. Both detectors are segmented crystal Cerenkov counters. Scattered electrons are deflected by a set of quadrupoles before they leave the beam pipe at $z = -27.3$ m through an exit window and hit the ET. The photons leave the proton beam pipe at the point where it bends upwards at $z = -92.3$ m and then reach the PD.

Two methods are used to determine the luminosity: For the coincidence method the scattered electron and the photon must be detected in coincidence. The photon method just uses the number of Bethe-Heitler events with a photon energy above a certain threshold. In the off–line analysis, the latter is used. The main background of the Bethe–Heitler process consists of the bremsstrahlung reactions between the incident leptons and the residual gas molecules ($eA \rightarrow eA\gamma$). The magnitude of this source of background can be evaluated by using *pilot bunches*, meaning bunches which do not collide with bunches from the other beam. After all corrections the systematic uncertainty in the luminosity measurements is 1.5 %.

#### The Time-of-Flight-System

The time-of-flight system rejects background originating from beam interactions with residual gas atoms or the beam pipe. Time-of-flight counters consisting of plastic scintillators are installed in the forward and background region of H1 at various places. In addition, a double wall of scintillators, the *veto wall*, is positioned at $-8.1\,\text{m} < z < -6.5\,\text{m}$. Based on a precise knowledge of the timing structure of the beams provided by the HERA clock, time windows are set corresponding to the position of the counters which reflect the amount of time a particle from an $ep$–interaction needs to reach the counters.

## 3.3 Trigger and Data Acquisition

The purpose of the trigger system is to select $ep$ interactions of physics interest and to reject background. The bunch crossing rate inside the H1 detector is 10.4 MHz whereas the data taking rate is only about 10 Hz. The rate of events with significant detector signals is about 100 kHz. The latter is completely dominated by background events such as beam-wall events, cosmic muons or halo muons. Since it is technically impossible to read out the entire detector information for each bunch crossing, a three level trigger system was designed to sequentially reduce the rate of triggered events such that the readout rate is reasonable small.

The first level trigger (L1) is a dead time free system which provides the decision to keep or reject an event within $2.3\,\mu$s. Because of the bunch crossing time of 96 ns the full event information is stored in a pipeline until all trigger information from the subdetectors (*trigger elements*) are available. The central trigger logic (CTL) combines these trigger elements into 128 *subtriggers*. An event is kept if one of these subtriggers has fired. After a positive trigger decision at level 1 the pipelines are stopped and the trigger data are submitted to the level 2 trigger systems.

The second level trigger (L2) is based on more sophisticated algorithms. The longer time available for a decision ($20\,\mu$s) allows to verify the L1 decision by the combination of signals from different subdetectors. For this purpose techniques are used which include neural networks and are sensitive to certain event topologies.

After a positive L2 decision the detector readout starts. The data are then submitted to the level 4 filter (L4). A partial reconstruction of the events is done by a processor farm with approximately 30 parallel processors. Subsequently decision algorithms decide whether an event is taken or not. The events accepted by L4 are written to tapes with a rate of approximately $10 - 20$ Hz.

The last trigger level (L5) is performed offline. The full event information is available at this stage. To obtain a further reduction of the data, the events are classified in different physical event classes. Finally the classified events are written to tape. Events not fulfilling the criteria of one physical class are rejected.

## 3.4 Detector simulation and event reconstruction

For each measurement it is of particular importance to understand the detector response in all aspects. For this purpose a detailed simulation of the H1 detector has been implemented using the GEANT [50] simulation tool. In this simulation the distribution of instrumented and uninstrumented material as well as the details of the geometrical acceptance and intrinsic resolution of the detector components are implemented.

For Monte Carlo (MC) events the tracking of the generated particles through the detector is performed in a first step. This includes tracking in the magnetic field, generation of secondary particles and shower development. The second step is the simulation of the response of the active detector components. Finally the output for a simulated event is as similar as possible to the response of the detector for a *real* event.

After the detector simulation, the Monte Carlo events are subject to the same reconstruction software as the actual data. In this step the reconstruction of charged tracks is performed as well as the clustering of cells with energy deposition in the calorimeters.

# Chapter 4

# General Data Analysis

Data from $e^+p$ and $e^-p$ collisions are investigated separately. They were recorded with the H1 detector in 1998/1999 ($e^-p$ collisions) and 1999/2000 ($e^+p$ collisions) at a centre of mass energy of 320 GeV. In order to ensure a reasonable data quality it must be assured that only events coming from electron-proton collisions are selected, for which the detector was fully operational. Background events not coming from electron-proton collisions (e.g. muons from cosmic showers or beam related background) must be rejected. The criteria of this general data selection are described in the first part of this chapter.

The event topologies of squark decay modes considered in this analysis rely on the identification of charged leptons and/or hadronic jets. After a description of the identification and measurement of electron/positron candidates and their energy calibration, the identification of muons is discussed. Then the reconstruction of hadronic jets and the calibration of hadronic energy in the LAr is presented. Finally the treatment of systematic uncertainties on the SM background is summarised.

## 4.1 Run selection and detector status

The periods of data taking at HERA are divided in luminosity fills, defined by one filling of electrons in the HERA ring. The luminosity fills are further subdivided into H1 runs, which last up to two hours. Only runs with stable detector, readout and triggering conditions, classified as *good* or *medium* quality are used in this analysis.

For a reliable measurement of the events which are of interest for this analysis, the information delivered by some H1 subdetectors is necessary. For this reason the following H1 components must be fully operational, i.e. functioning readout and operation at nominal high-voltage (HV status) are required for

- the Central Jet Chambers (CJC1 and CJC2);
- the Central Proportional Chambers (CIP and COP);
- the Liquid Argon Calorimeter (LAr);
- the Spaghetti Calorimeter (SPACAL);
- the Luminosity system;

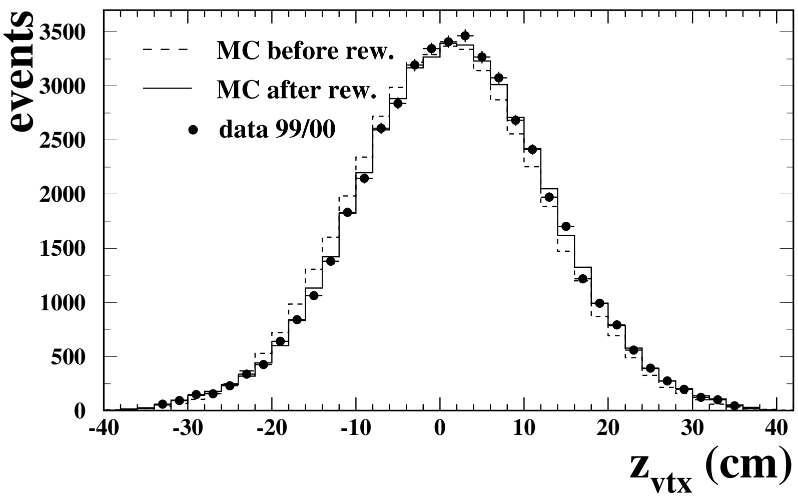


Figure 4.1: $z_{\rm vtx}$ distribution before and after the reweight for the full 1999/2000 period.

- the Time of Flight system (TOF).

The reconstruction of an electron-proton interaction vertex (primary vertex) and the measurements of charged tracks pointing to potential electron candidates rely on information coming from the Central Jet Chambers. The Central Proportional Chambers are essential for triggering of the events. The Calorimeters, in particular the LAr, are indispensable for this analysis since they are needed for the energy measurements of electrons and hadronic jets and for triggering of the events. The luminosity is determined using information from the luminosity system. Finally the TOF is necessary for the rejection of non-*ep* background.

## 4.2 Event vertex and vertex reweight

For most events not coming from *ep* collisions no primary event vertex can be found using central and forward tracks. The amount of non-*ep* background events can be significantly reduced by requiring that for each event a vertex is reconstructed. A cut on the $z$-position of the event vertex $z_{\rm vtx}$ leads to a further background reduction. Therefore it is required that

$$-35\,{\rm cm} < |z_{\rm vtx} - z_{\rm run}| < 35\,{\rm cm}\ , \tag{4.1}$$

where $z_{\rm run}$ is the nominal $z$-position of the run. This criterion additionally ensures a reliable measurement of the events within the detector acceptance.

Furthermore the variable $z_{\rm vtx}$ is important for the reconstruction of the polar angle of the scattered electron and of the jets. For a reliable description of SM background processes by the Monte Carlo an adequate simulation of the $z_{\rm vtx}$ distribution is needed. Because of instabilities related to the HERA beams the $z_{\rm vtx}$ distribution in the data is time dependent and not gaussian as assumed in the simulation.

This deficiency of the simulation must be corrected for by reweighting the $z_{\mathrm{vtx}}$ distribution in the simulation to that observed in the data. Because of changes of beam conditions, the $z_{\mathrm{vtx}}$ distributions of 1998/1999 and 1999/2000 data differ. In addition, the 1999/2000 data set must be subdivided in two parts since a small shift of the vertex position by 3.5 cm can be observed in approximately one half of the period (after H1 run 269 935). Thus the reweight has been done separately for three time periods of H1 data taking using a parameterisation of the $z_{\mathrm{vtx}}$ distribution in data and MC.

In Fig. 4.1 the $z_{\mathrm{vtx}}$ distribution of data and simulation before and after the reweight is shown for the full 1999/2000 data period (both $z_{\mathrm{vtx}}$ periods). In the plot the distribution is given for events with an electron candidate (see Sec. 4.5.1) with transverse momenta $p_{T,e} > 16\,\mathrm{GeV}$. After the reweight the simulation describes the peak position, the width and the shape of the data very accurately. Even the tails of the distribution are well modelled.

## 4.3 Data sets and luminosities

All HERA data collected with the H1 detector at a centre of mass energy of 320 GeV are exploited to search for squarks. At this energy, data from $e^-p$ and $e^+p$ collisions are available. The integrated luminosities and the H1 run ranges of the two data sets are summarised in Tab. 4.1. The luminosity values correspond to the run selection mentioned above and are corrected for the detector requirements of this analysis (HV status and readout status). In addition, an effect on the luminosity determination coming from satellite bunches in the HERA ring is taken into account[1]. The latter correction depends on the allowed $z_{\mathrm{vtx}}$ range given in Eq. 4.1.

| data set | collisions | $\int \mathcal{L}dt$ | H1 run range |
|---|---|---|---|
| 1998–1999 | $e^-p$ | $13.5\,\mathrm{pb}^{-1}$ | 218 217 – 241 649 |
| 1999–2000 | $e^+p$ | $64.3\,\mathrm{pb}^{-1}$ | 244 968 – 279 215 |

TABLE 4.1: Integrated luminosities of the data sets.

A period of $e^+p$ data taking ($4.1\,\mathrm{pb}^{-1}$) with special trigger settings (*minimum bias run*) in 1999 is included in the analysis of the 1999/2000 data sample. In contrast, data taken during the *shifted vertex run*[2] are not considered.

Data at a lower centre of mass energy ($\sqrt{s} = 300\,\mathrm{GeV}$) which were taken up to 1997 are not investigated in this analysis. In [11] it has been shown, that these data do not show a deviation from the SM with regard to squark production. An inclusion of this data set would give an increase of the total $e^+p$ luminosity of roughly 50 %. Nevertheless this would lead to a very small improvement of the exclusion limits at small squark masses only. As can be seen from Eq. 2.47, Eq. 2.48 and Fig. 2.14 the production cross sections for

[1]Satellite bunches are bunches of lower intensity, which follow the main bunches. They cause too high a measurement of the luminosities.

[2]For a small fraction of the 2000 data taking period ($0.7\,\mathrm{pb}^{-1}$) the nominal interaction vertex of positrons and protons was shifted towards the forward direction ($z_{\mathrm{vtx}} = 70\,\mathrm{cm}$) to extend the kinematic reach of H1 towards small values of $Q^2$.

squarks strongly depend on the beam energies and they are drastically smaller at lower energies. This effect is largest at high $x$ (high squark masses) resulting in basically no improvement of exclusion limits at high masses with data at $\sqrt{s} = 300\,\text{GeV}$ included.

## 4.4 Rejection of non-*ep* background

There are various sources of events coming from non-*ep* interactions which are recorded. The so called *beam-gas* and *beam-wall* events come from the interaction of protons with residual gas atoms or the beam pipe. In addition muons from cosmic rays or beam-halo muons produced in the decays of charged pions resulting from beam-gas or beam-wall events give a significant background contribution. They can give tracks in the central tracking system or produce showers in the calorimeters, which can be misidentified as electrons or hadrons.

The majority of these background events are rejected by the Time-of-Flight system described in Sec. 3.2.5. The vertex requirement described in Sec. 4.2 also removes a large part of these events. Nevertheless it is essential to reach a further suppression of non-*ep* background by requiring that the event time determined from the drift time in the Central Jet Chambers is consistent with the time of the *ep* bunch crossing.

In addition, a standard set of topological background finders is used to reject events from cosmic or halo muons[3]. By combining the information of various subdetectors these finders search for long and narrow signatures which are typical for cosmic and halo muons traversing the H1 detector.

The momentum balance with respect to the direction of the incident electron is obtained as

$$\sum (E - p_z) = \sum E_i \,(1 - \cos\theta_i)\,, \tag{4.2}$$

where the sum runs over all energy deposits $i$ in the calorimeters. In *ep* events, where either all particles are detected and well measured or only particles escaping in the proton direction remain undetected, $\sum (E - p_z)$ should peak at twice the energy of the incident electron $\sum(E - p_z) = 2E_e^0$. Smaller values can only be produced by undetected particles (e.g. neutrinos) or energy mismeasurement. On the other hand, much larger values could be a result of mismeasurement or non-*ep* background. Therefore a cut $\sum(E - p_z) < 75\,\text{GeV}$ is applied to reject the latter.

In addition Known background events are removed by hand. After these selection criteria, a visual scan of events showed that the amount of non-*ep* background events in the remaining data sample is very small. For the final selection all remaining events are visually scanned.

## 4.5 Lepton identification

Decay topologies involving charged electrons, positrons and muons are searched for. In the following the identification algorithms for these charged leptons are described. Decay channels with taus leptons in the final state are explicitly investigated.

[3]The first 10 bits of the background finder QBGFMAR [51] are used.

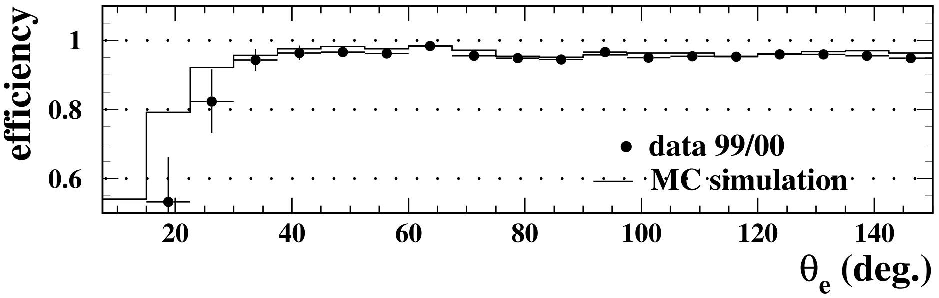


Figure 4.2: Finding efficiency of charged tracks with DCA< 12 cm to the electromagnetic cluster for 1999/2000 data and MC simulation as a function of the polar angle of the scattered electron for a clean sample of high $Q^2$ NC DIS events.

### 4.5.1 Electron candidates

The identification of electron candidates is based on the standard H1 electron finding algorithm[4]. Clusters initiated by electromagnetic interacting particles (electrons/positrons and photons) are separated from clusters initiated by hadrons by analysing the shower shape of energy deposits in the calorimeters. Isolated and compact electromagnetic clusters are selected. Since electrons coming from squark decay are mainly emitted in the forward direction, only LAr information is used here.

The polar angle of the electron $\theta_e$ is determined from the center of gravity of the electromagnetic cluster and the reconstructed primary vertex. The azimuthal angle $\phi_e$ is taken from track information if available. By minimising the spatial discrepancy between the electron track and the location of the calorimeter cluster, the alignment of the tracking detectors relative to the LAr has been established to within 1 mm in the $x$, $y$ and $z$ directions [53].

Detector regions, where the measurements of the electron candidates are not reliable, must be excluded from the analysis. It is especially problematic to measure electron candidates in the regions between active calorimeter modules. Therefore electron candidates which are located in the vicinity of a $\phi$-crack between calorimeter octants are excluded by requiring $|\phi_e - \phi_{\text{crack}}| > 2°$. In addition, electrons near to one of the two most central $z$-cracks between calorimeter wheels (CB1/CB2 and CB2/CB3) are rejected by requiring that the $z$-component of the impact point of the electron on the calorimeter surface $z_{\text{imp}}$ is not found in the regions $15\,\text{cm} > z_{\text{imp}} > 25\,\text{cm}$ or $-65\,\text{cm} > z_{\text{imp}} > -55\,\text{cm}$. The remaining $z$-cracks which are located in forward or backward direction are not excluded since the distance an electron from the event vertex can travel between the sensitive modules is not too long for a reliable position and energy measurement.

The amount of selected photons and hadrons (especially neutral pions) can be substantially reduced by requiring a charged track pointing to the electromagnetic cluster for electron candidates in the central detector region ($\theta_e > 30°$). Here the charged tracks are measured reliably by the central tracking system. The tracks must have a distance of clos-

[4]QESCAT [52]

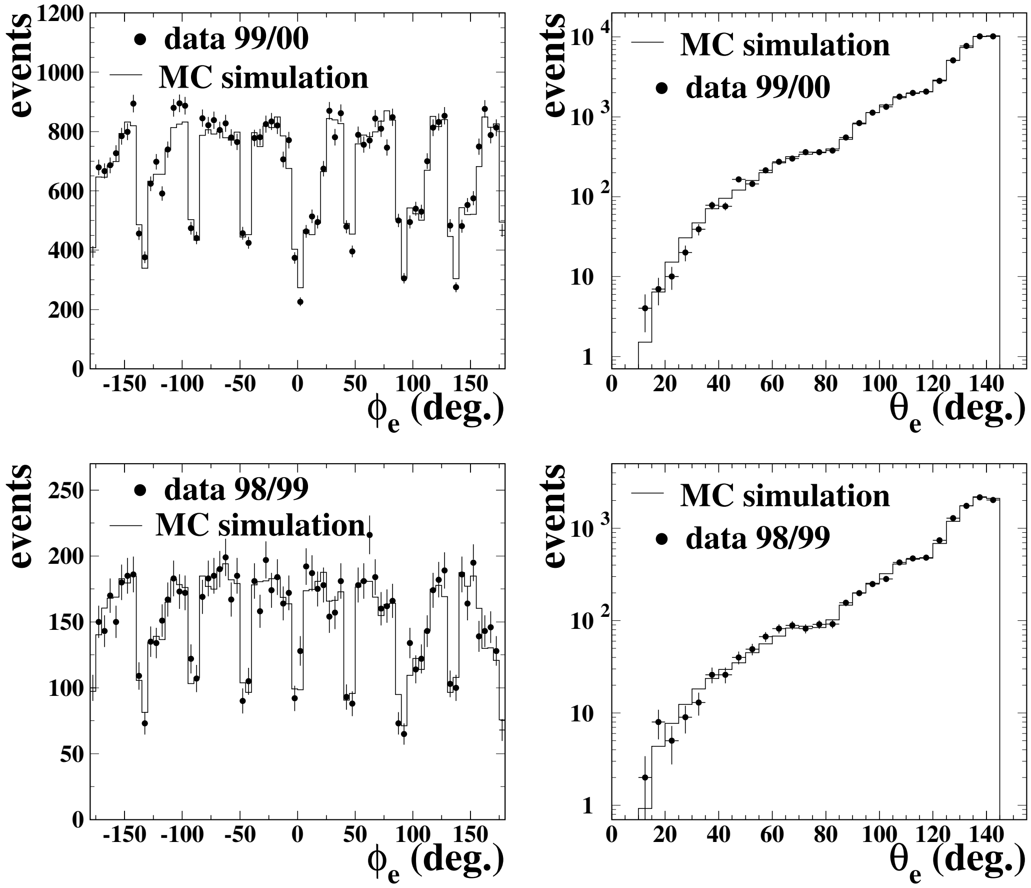


Figure 4.3: Distribution of the azimuthal (left) and polar (right) angles of electron candidates for events with an electron with $p_{T,e} > 16\,\text{GeV}$ in 1999/2000 (top) and 1998/1999 (bottom).

est approach (DCA) to the cluster of less than 12 cm. The distance of closest approach is defined as the perpendicular distance between the center of gravity of the cluster and the tangent to the extrapolated track at its impact point on front surface of the calorimeter.

The track finding efficiency for this track requirement has been checked separately for both the 1998/1999 and 1999/2000 samples in data and MC simulation using a very clean NC sample ($p_{T,e} > 16\,\text{GeV}$ with strict transverse momentum balance[5] $p_{T,\text{miss}} < 8\,\text{GeV}$ and $50\,\text{GeV} < \sum(\mathrm{E} - \mathrm{p_z}) < 60\,\text{GeV}$). The results for the 1999/2000 data period are shown in Fig. 4.2. In data and MC the efficiency for finding electron tracks is around 95 % in the

[5]The missing transverse momentum $p_{T,\text{miss}}$ is obtained as

$$p_{T,\text{miss}} \equiv \sqrt{\left(\sum_i E_i \sin\theta_i \cos\phi_i\right)^2 + \left(\sum_i E_i \sin\theta_i \sin\phi_i\right)^2}, \tag{4.3}$$

where the sum runs over all energy deposits $i$ in the calorimeters.

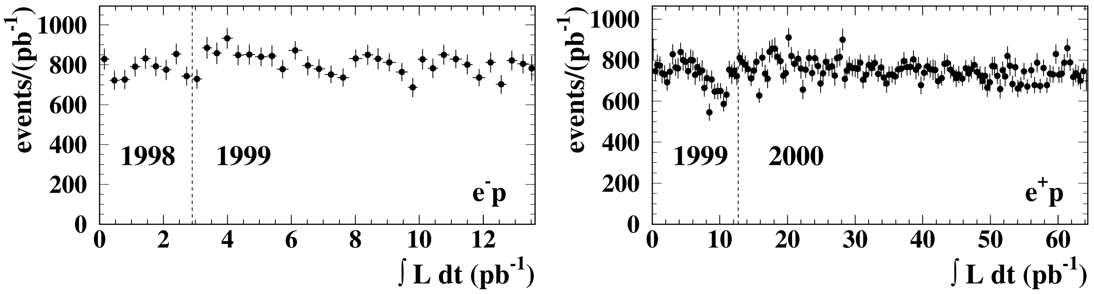


Figure 4.4: Yield of events as a function of accumulated luminosity for a high $Q^2$ NC sample. In 1999 ($e^+p$) a broken wire of CJC2 causes a lower event selection rate.

central detector region where the Central Jet Chambers provide a reliable track measurement. In this region the simulation overestimates the efficiency by roughly 1 %. These differences are corrected for by applying $\theta$ dependent event weights to the MC events. Because of multiple scattering in the forward region the efficiency is reduced for small values of $\theta_e$. The data show a significantly smaller efficiency than the simulation because of known problems of the description of the Forward Track Detector by the simulation. For this reason a track is required in the central region of the detector only. The track efficiency in 1998/1999, which is not shown explicitly, is found to be similar.

Events with a highly energetic electron are mainly triggered using information from the LAr. The finely segmented geometry of the LAr allows the trigger to select compact energy deposits in the electromagnetic section of the calorimeter. We use subtriggers[6], which are commonly used in H1 for triggering electrons with high $p_T$ [54,55]. In order to ensure that the electron trigger efficiency of the LAr trigger system [56] is high, it is required that the energy of the electron candidates exceeds 11 GeV. Regions of particularly low trigger efficiency in the LAr are rejected by applying run dependent fiducial cuts. The affected regions and run ranges are taken from [54]. The effect of these cuts has been taken into account in the treatment of the Monte Carlo by rejecting the same amount of MC events in the relevant fiducial volume as in the data. The trigger efficiency of the used subtriggers has been checked in [54,57] using independently triggered events. In the kinematic range considered in this analysis, the NC trigger efficiency was found to be consistent with 100 % within the statistical error.

The distributions of the polar angle $\theta_e$ and the azimuthal angle $\phi_e$ of identified electron candidates are shown in Fig. 4.3 for events with an electron candidate with $p_{T,e} > 16$ GeV, which are balanced in $p_T$ and $\sum(E - p_z)$. The MC simulation describes the data well throughout the complete angular range for both data sets – $e^+p$ data (top) and $e^-p$ data (bottom). The $\phi_e$ distributions clearly reveal the calorimeter $\phi$-cracks between calorimeter octants at 45° intervals. The regions in between with fewer events are relicts of the fiducial trigger requirements and dead regions in the CJC. In contrast the two rejected $z$-cracks are smeared out in the $\theta_e$ distribution because of the octagonal structure of the LAr wheels. The distributions of data and MC (DJANGO, CTEQ5L) are luminosity normalised.

[6]S67, S71, S75, and S77

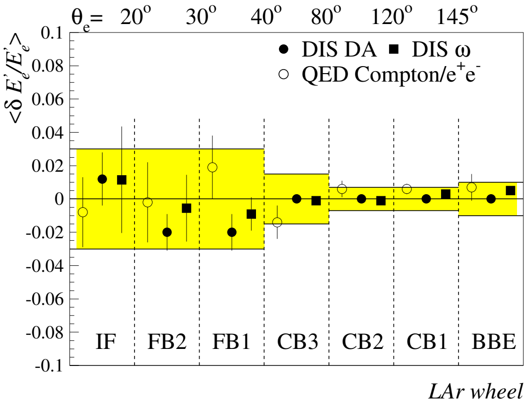


FIGURE 4.5: Comparison of the electromagnetic energy scale as determined by different calibration methods. Shown is $\langle \delta E'_e / E'_e \rangle$, the mean fractional energy shift of the different methods from the absolute energy scale. The figure is taken from [53].

For the same selection, representing the cleanest event sample with high statistics, the event yields ($\Delta N/\Delta\mathcal{L}$) as a function of accumulated luminosity (or time) are shown in Fig. 4.4 for the two data taking periods separately. The number of selected events is rather constant with time. This indicates that in this analysis all instabilities of the detector status or the data taking are taken into account properly. A slight decrease of the event yield can be observed since the number of dead trigger regions in the LAr increases with time. The reason for a smaller event rate in 1999 ($e^+p$) is a broken wire in the Central Jet Chamber (CJC2). The track requirement for central electron candidates leads to fewer selected events in this period. This inadequacy of the CJC is taken into account in the detector simulation of MC events.

**Electron energy calibration**

The electron energy $E_e$ is determined from the cluster energy and is calibrated using the standard calibration developed in [53]. This calibration makes use of the over-constrained kinematics of NC DIS events which allow the prediction of the energy of the scattered electron from the electron beam energy, the scattering angle of the electron and the effective angle of the hadronic final state with the double angle method (DA) [58]. In the barrel region NC events are used to determine calibration factors for data and MC by constraining the mean of the $E_e/E_{\mathrm{DA}}$ to 1 in finely segmented $z$ and $\phi$ regions defined by the impact position of the electron track on the LAr front face. Since the statistics of DIS events in the forward region are limited, elastic QED Compton and exclusive two photon $e^+e^-$ pair production are used here in addition. A single calibration constant is determined for the entire forward region (If, FB2, FB1).

After application of these calibration procedures, the positron energy scale is checked in [53] for each calorimeter wheel using the elastic QED-Compton and the $e^+e^-$ event sample and, separately, the $\omega$ method [59] for the DIS sample. The results from all the different methods are found to be in good agreement, as shown in Fig. 4.5. An error of

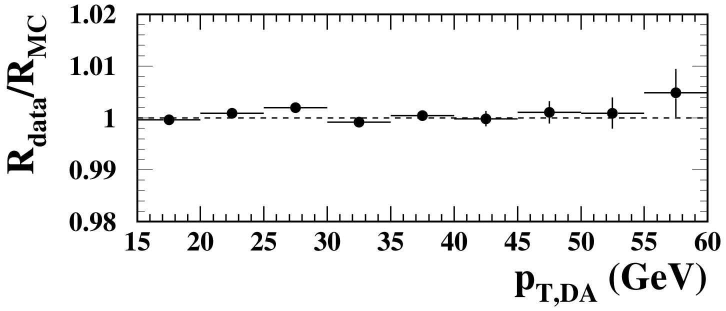


FIGURE 4.6: Dependence of the electron calibration on the transverse momentum. Shown is the ratio $R_{\rm data}/R_{\rm MC}$ with $R_{\rm data}$ and $R_{\rm MC}$ being the fitted mean of the $(p_{T,e}/p_{T,\rm DA})$ distribution in the corresponding $p_{T,\rm DA}$ range for data and MC respectively.

$\pm 0.7$ (1.0, 1.5, 3.0) % on the absolute electromagnetic energy scale of the CB1-CB2 (BBE, CB3, FB1-IF) wheels of the detector is therefore assigned. This uncertainty is indicated by the shaded error band in Fig. 4.5.

For the analysis presented here, the $p_T$ dependence of the electron calibration has been checked additionally by comparing the distributions of $p_{T,e}/p_{T,\rm DA}$ as a function of the transverse momentum determined from the double angle method $p_{T,\rm DA}$ for an event sample with an electron with high transverse momentum $p_{T,e} > 16$ GeV. In each $p_{T,\rm DA}$ bin a truncated gaussian has been fitted to the $p_{T,e}/p_{T,\rm DA}$ distribution in data and MC. The ratio of the fitted mean values are shown in Fig. 4.6. After calibration no $p_T$ dependence is observed.

### 4.5.2 Muon candidates

Some decay modes of squarks lead to final states involving muons. As minimal ionizing particles (MIPs), muons with high energy penetrate the whole detector and generally deposit little energy in the calorimeters. Depending on their polar angle $\theta_\mu$ muons leave signatures in the central and forward inner tracking system, the Liquid Argon Calorimeter, the instrumented Iron and the Forward Muon detector.

The identification of muons is based on a standard H1 track and muon selection[7]. Muon candidates are accepted if an inner track measured in the Central or in the Forward Track Detectors can be associated with a muon signature in the Instrumented Iron or in the Forward Muon Detector. Muons with transverse momenta smaller than $1.5 - 2.0$ GeV are not able to transverse the calorimeter and to reach the muon detectors. They are stopped in the LAr and leave the signature of a MIP. They are identified by an inner track which is extrapolated to the calorimeter and points to the MIP signature. The transverse momenta of the muon candidates are measured using the curvature of the associated track in the inner track detectors.

The muon finding efficiency of this standard selection has been checked in [61] and [62]

[7] QHQTRK [60]

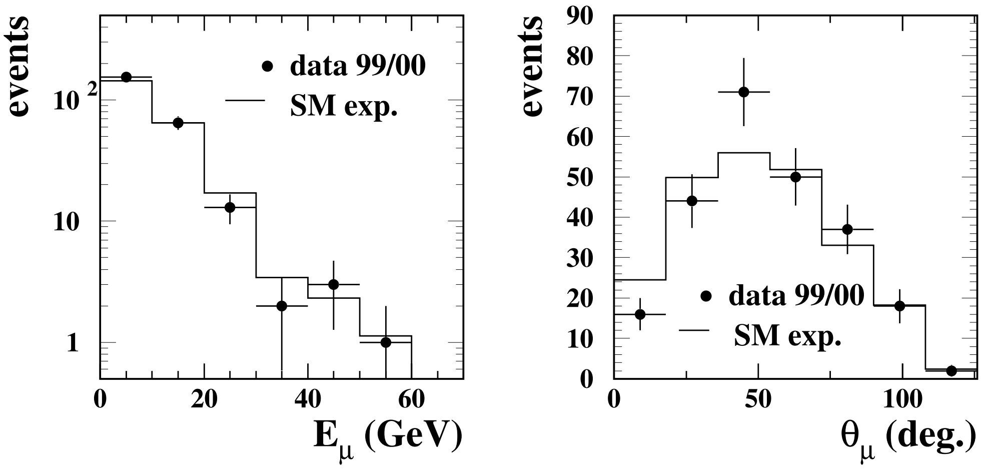


Figure 4.7: Control of muon background in events with an electron of high $p_T$. Energy spectrum (left) and polar angular distribution (right) of muon candidates are well described by the MC which is mainly NC DIS.

by studying events from elastic muon pair production and muons from cosmic showers. The latter allows a determination of the efficiency up to transverse momenta of 80 GeV. From the former the efficiencies at low momenta can be determined. The efficiency was found to be around 80 % in the central region and 70 % in the forward region. It is well modelled by the Monte Carlo simulations. It has been shown that the reconstruction efficiency is independent of the muon's momentum for muons with momenta greater than 3 GeV.

In order to test the description of background processes satisfying the muon selection criteria the energy spectrum and the polar angular distribution of muon candidates with $p_{T,\mu} > 4\,\mathrm{GeV}$, found in events with an electron with $p_T > 16\,\mathrm{GeV}$, are shown in Fig. 4.7. Both distributions are described by the MC simulation.

## 4.6 Treatment of the Hadronic Final State

All squark decay modes in $\not{R}_p$ supersymmetry lead to hadronic activity in the detector since at least one quark is involved in the final state. Gauge decays of squarks lead even to signatures with multiple hadronic jets. In dealing with the hadronic final state[8] we make use of a standard software package[9]. In the following the reconstruction algorithm of jets in the detector is introduced and the calibration of hadronic energy is presented.

### 4.6.1 Reconstruction of jets

Free quarks or free gluons can not exist because QCD, the theoretical framework which describes the strong interaction of quarks and gluons, is a non-abelian gauge theory, leading

[8] The hadronic final state is defined as all particles in the detector except the electron candidates.
[9] HFS [63]

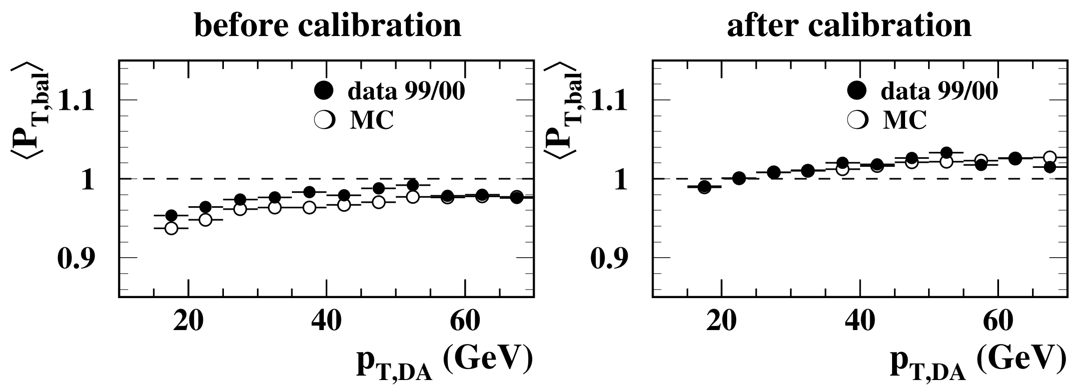


Figure 4.8: Mean of the $p_{T,\mathrm{bal}} = p_{T,\mathrm{HFS}}/p_{T,\mathrm{DA}}$ distributions as a function of $p_{T,\mathrm{DA}}$ for a sample of NC events before and after the additional calibration.

to confinement. Through fragmentation quarks and gluons transform into showers of hadrons containing many particles. Since they are mainly emitted with low transverse momenta with respect to the direction of the initial parton, collimated jets of particles are visible in the detector. A number of jet algorithms have been developed in order to identify jets and to measure the properties of the initial partons. In this analysis jets are reconstructed from energy deposits in the LAr using the cone algorithm CDFCONE in the laboratory frame. The results of the analysis presented here are found to be only weakly dependent on the choice of the jet algorithm. A detailed description of CDFCONE can be found in [64, 65]. Here the most important aspects are briefly summarised.

In this algorithm a jet is defined as the particles lying inside a cone with a radius $R$ in the $(\eta, \phi)$-plane. The cone axis is given by the direction of the total momentum of the particles belonging to the jet. The total transverse energy[10] of the particles inside the cone must be higher than a certain value $E_T^{\mathrm{cut}}$. In the present analysis the cone radius and the minimal total transverse energy are set to the commonly used values $R = 1$ and $E_T^{\mathrm{cut}} = 5\,\mathrm{GeV}$. The cone algorithm reconstructs hadronic jets which are clearly separated in $(\eta, \phi)$ [64–66]. For control plots of the jet reconstruction see Chap. 6 where the selection of events containing jets and an electron is presented, and the description of jet production by various MC models is discussed.

### 4.6.2 Calibration of hadronic energy

The energies of jets and the hadronic final state must be corrected since the hadronic energy scale is not known precisely. The hadronic energy scale can be adjusted using the known electron energy in NC DIS events. Nevertheless the calibration of hadronic energy is not of major importance for this analysis since the statistical errors or other systematic uncertainties exceed the uncertainty coming from the hadronic energy scale.

The calibration implemented in the HFS package is based on an analysis of data from

[10]The transverse energy is chosen since the center of mass energy in $ep$ collisions at HERA is boosted in the forward direction and the jet definition should be invariant under Lorentz transformations.

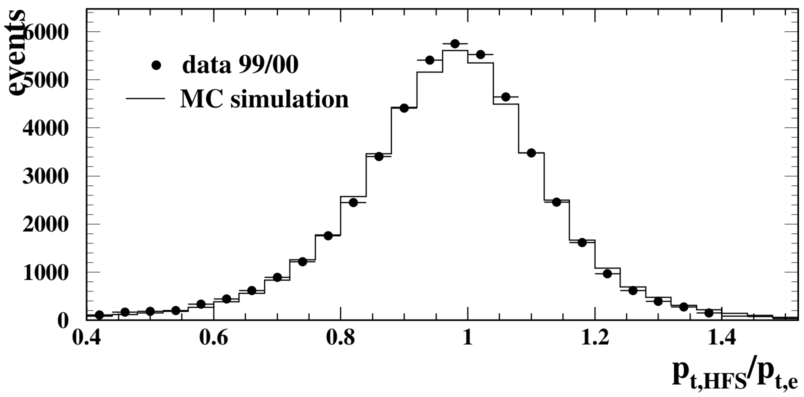


Figure 4.9: The ratio of the transverse momentum of the hadronic final state to the transverse momentum of the scattered electron for a large inclusive sample of NC events.

1994-1997 [55]. The main principle of the calibration method used in this work is to determine the transverse momentum balance $p_{T,\text{bal}} = p_{T,\text{HFS}}/p_{T,e}$ between the electron and the hadronic final state in NC events. In various detector regions the ratio of the mean values of $p_{T,\text{bal}}$ of data and MC is used to correct the hadronic energy and to shift the MC to the data. An absolute calibration is not performed.

Using this standard calibration in HFS for the 1998/1999 and 1999/2000 data some insufficiencies can still be observed. These are known effects and have been seen also by other analyses in H1 [67]. In Fig. 4.8 (left) the $p_T$ dependence of the calibration is illustrated for the 1999/2000 period. The ratio $p_{T,\text{bal}} = p_{T,\text{HFS}}/p_{T,\text{DA}}$ is shown as a function of $p_{T,\text{DA}}$ for events with an electron with $p_{T,e} > 16\,\text{GeV}$ and exactly one jet. In data and MC the mean values of $p_{T,\text{HFS}}/p_{T,\text{DA}}$ are extracted by a truncated gaussian fit to the distribution of events within a certain $p_{T,\text{DA}}$ range. In the MC a small underestimation of the order of 2 % of the hadronic energy compared to the data can be observed. For both data and MC the hadronic energy is measured to be too small compared to the electron energy – it is not an absolute calibration.

In order to correct for these insufficiencies an additional calibration on top of the HFS standard calibration has been performed. For events with an electron with $p_{T,e} > 16\,\text{GeV}$ and exactly one jet, calibration constants for data and MC have been determined by constraining the transverse momentum balance of the electron and the jet $p_{T,\text{jet}}/p_{T,e}$ in $5°$ bins of the polar angle of the jet. These calibration constants are applied to all jets found in the events and to the energy not contained in jets. For the latter a single four-vector is determined and the corresponding calibration factor is applied. No $p_T$ dependent calibration has been carried out.

The $p_T$ dependence after this additional calibration procedure is illustrated in Fig. 4.8 (right). Again the mean values of $p_{T,\text{bal}} = p_{T,\text{HFS}}/p_{T,\text{DA}}$ are shown as a function of $p_{T,\text{DA}}$. Data and MC show the same behaviour – the difference between the two is very small. For both data and MC the $p_T$ dependence of the calibration is found to be small. The

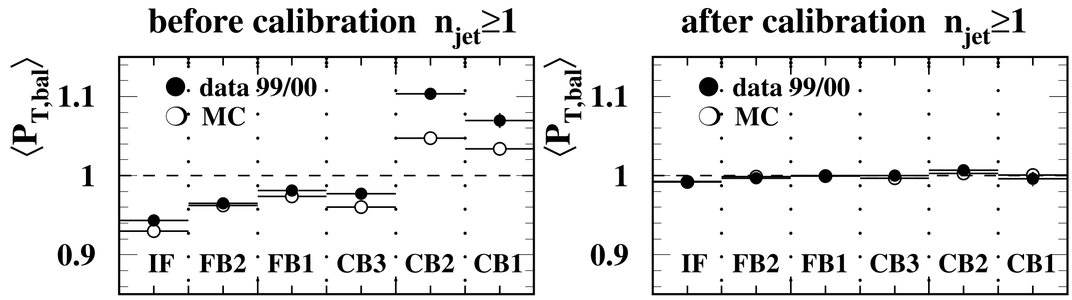


FIGURE 4.10: Mean of the weighted $p_{T,\mathrm{bal}} = p_{T,\mathrm{HFS}}/p_{T,e}$ distributions of LAr wheels before (left) and after (right) the calibration for events with at least one jet.

fitted mean values of $p_{T,\mathrm{HFS}}/p_{T,\mathrm{DA}}$ slightly increase for data and MC with increasing $p_{T,\mathrm{DA}}$. Fig. 4.9 illustrates that after the additional calibration the $p_{T,\mathrm{HFS}}/p_{T,e}$ is indeed balanced for an inclusive high $Q^2$ NC sample ($p_{T,e} > 16\,\mathrm{GeV}$) and that even the tails of the distribution are well modelled.

A new method has been developed to check the performance of the calibration for events containing jets. In this method for each jet $i$ with $p_{T,\mathrm{jet}} > 6\,\mathrm{GeV}$ the variable $p_{T,\mathrm{bal}} = p_{T,\mathrm{HFS}}/p_{T,e}$ is filled in a histogram, which corresponds to the calorimeter wheel the jet points to. Here $p_{T,\mathrm{HFS}}$ is the transverse momentum of the full hadronic final state of the event in which the jet is found. The entry in the histogram is weighted by $p_{T,i}/p_{T\mathrm{alljets}}$.

With this method all jets in the event are considered and jets with higher transverse momentum contribute more. In Fig. 4.10 the mean values of these histograms coming from truncated gaussian fits to data and MC are shown for events containing at least one jet and an electron with high $p_T$. Before the calibration (left) the energy measurement of data and MC agree within 2 % for the forward wheels and for the CB3. These forward wheels are most important since the bulk of the hadronic activity is located in this region.

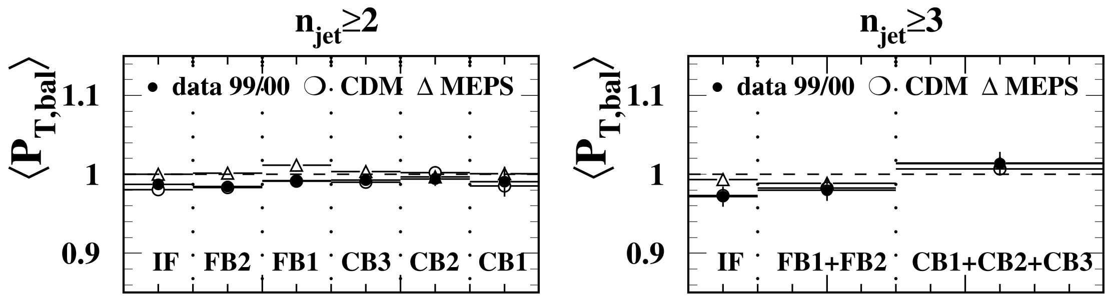


FIGURE 4.11: Mean of the weighted $p_{T,\mathrm{bal}} = p_{T,\mathrm{HFS}}/p_{T,e}$ distributions of LAr wheels for events with at least two jets (left) and with at least three jets (right). Two different models of QCD radiation are shown.

In contrast, in CB2 and CB3 the statistics are rather limited and the deviation of data and MC is of the order of 5 %. After the calibration (right) the means of the distributions agree within 1 % for all calorimeter wheels.

Additionally, these checks have been performed for events containing multiple jets. The corresponding results after the additional calibration are shown in Fig. 4.11 for events with at least two (left) and three (right) jets. For the latter the statistics are rather limited. For this reason the mean values for data and MC are not determined for each calorimeter wheel separately, but for three LAr regions only: the inner forward wheel (IF), the forward barrel region (FB1 and FB2 are combined to one region) and the central barrel region (CB1, CB2 and CB3 are combined). Two different descriptions of QCD radiation have been tested in the MC – the Colour Dipole Model (CDM) and the Matrix Element and Parton Shower model (MEPS). For a detailed discussion of these models see Sec. 6.1.2. Both samples (at least two or three jets) demonstrate that the calibration shows no dependence on the calorimeter region and is reliable within 2 % for both MC models. For events containing at least four or more jets the statistics are not sufficient for calibration checks of this kind.

All these checks indicate that the uncertainty attributed to the limited knowledge of the hadronic energy scale is of the order of 2 %.

## 4.7 Systematic uncertainties on SM background processes

For the evaluation of the systematic error on the SM expectation in the selection of all final state topologies the following sources of **experimental uncertainties** have been considered.

- The uncertainty on the electromagnetic energy scale varies from $\pm 0.7$ % to $\pm 3$ % depending on the calorimeter region as explained in more detail in Sec. 4.5.1.
- An uncertainty of $\pm 2$ % is attributed to the limited knowledge of the hadronic energy scale as outlined in Sec. 4.6.2.
- An error of $\pm 1.5$ % is assigned to the measurement of the integrated luminosity (Sec. 3.2.5).

The uncertainties on the electromagnetic and hadronic energy scale are taken into account by shifting the corresponding energies by $\pm 1\sigma$ for MC events of all SM background processes. The maximum deviation from the standard value is taken as systematic uncertainty for both sources separately. These uncertainties are then added in quadrature. Furthermore the uncertainty on the integrated luminosity is added in quadrature. The error arising from the limited statistics of SM background MC samples is treated as systematic uncertainty and is added as well.

Additional sources of errors arise from the **theoretical uncertainty** of the SM background processes.

- An error of $\pm 7$ % on the DIS expectation is attributed to the limited knowledge of the proton structure, as in [68]. At high $x$ where the uncertainty is expected to be larger the total error is dominated by the statistics.

- A model uncertainty of $\pm 10\,\%$ is assigned on the predicted cross section for multijet final states. This value is derived from comparisons of the CDM model and the MEPS model (see Sec. 6.1.2). It is of the same order of magnitude as assumed in [11] and [69].

These theoretical errors are added in quadrature to the experimental uncertainties discussed previously leading to the total systematic uncertainty on the SM expectation in each selection channel. The systematic uncertainties on the signal production cross section and the selection efficiencies are discussed in Sec. 5.1.3.

# Chapter 5

# Lepton–Quark Channels

In $R\!\!\!/_p$ supersymmetry a squark can decay directly via $R\!\!\!/_p$ into a lepton and a quark. As can be seen from Eq. 2.45, a $\tilde{d}^k_R$ produced in $e^-p$ collisions could decay either into $e^- + u^j$ or $\nu_e + d^j$, while a $\tilde{u}^j_L$, which could be produced in $e^+p$ collisions, decays into $e^+ + d^k$ only. Following from Eq. 2.49 the lepton–quark channels contribute only at high values of the Yukawa coupling $\lambda'$. For this reason they are most important at high squark masses where large $x$ values and small parton densities require a large value of $\lambda'$ in order to obtain a measurable cross section (see Fig. 2.14). In this chapter the selection and mass spectra of the two lepton–quark channels ($eq$ and $\nu q$) are presented and the signal efficiencies needed to calculate exclusion limits on model parameters are determined. Note that an exclusive selection must be ensured for both channels with respect to all other channels (esp. $eMJ$ and $\nu MJ$).

## 5.1 Electron–quark channel

### 5.1.1 Event selection

The final state of squarks decaying in the channel $eq$ is very similar to the final state of NC DIS reactions at high $Q^2$ since both consist of an electron with high transverse momentum[1] and a hadronic jet. For the selection of events coming from squark decays the Lorentz invariants $y$, $Q^2$ and $x$ characterising the kinematics of a DIS reaction, as well as the energy $M$ in the centre of mass of the hard subprocess, are determined using the measurement of the polar angle $\theta_e$, the energy $E_e$ and the transverse energy $E_{T,e}$ of the electron with the highest transverse momentum. In this *electron method* the variables are defined as

$$y_e = 1 - \frac{E_e(1-\cos\theta_e)}{2E_e^0}, \quad Q_e^2 = \frac{E_{T,e}^2}{1-y_e}, \quad x_e = \frac{Q_e^2}{y_e s}, \quad M_e = \sqrt{x_e s} \ . \qquad (5.1)$$

[1] An electron with high $p_{T,e}$ is expected in events from squark decay since the heavy squark decays to two particles ($eq$) only.

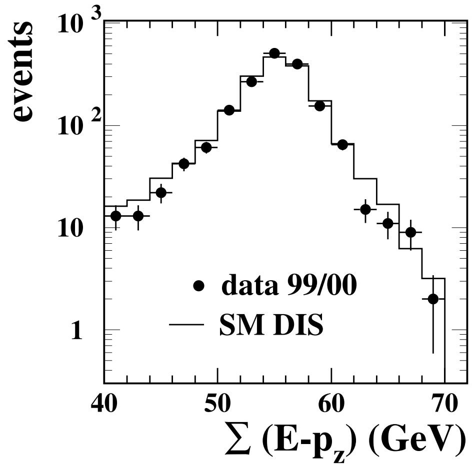


Figure 5.1: $\sum(E - p_z)$ distributions for 1999/2000 (left) and 1998/1999 (right).

**First selection steps**

The first selection criteria for the $eq$ channel are the following:

- The total transverse momentum of the events must be balanced: $p_{T,\mathrm{miss}} < 15\,\mathrm{GeV}$. Since all particles of the $eq$ final state can be detected, higher values of $p_{T,\mathrm{miss}}$ can only be produced by mismeasurement of the transverse momenta of the particles in the event or by particles escaping detection (e.g. neutrinos).

- For the same reason, the reconstructed momentum loss in the direction of the incident electron must be limited such that $40 \leq \sum(E - p_z) \leq 70\,\mathrm{GeV}$.

- To reduce the contamination from photoproduction, it is required that there be less than 5 GeV of measured energy in the backward calorimeter.

- An electron must be found in the LAr with $p_{T,e} > 16\,\mathrm{GeV}$. For electrons in the central detector region ($\theta_e > 30°$) at least one charged track pointing to the electromagnetic cluster is required. As mentioned in Sec. 4.5.1 the track must have a DCA of less than 12 cm to the electromagnetic cluster in the LAr.

- In addition, the selection is restricted to the kinematic range $Q^2_e > 2\,500\,\mathrm{GeV}^2$ and $0.1 < y_e < 0.9$. The resolution in $M_e$ degrades with decreasing $y_e$ ($\delta M_e/M_e \propto 1/y_e$) and so the low $y$ domain is excluded. Excluding the high $y_e$ values avoids the region where migration effects due to QED radiation in the initial state are largest for the kinematic reconstruction method using the electron. Furthermore background from photoproduction where a jet is misidentified as an electron is suppressed.

After these selection steps 1720 (526) events are selected in the 1999/2000 (1998/1999) sample with $1762 \pm 125$ ($502 \pm 35$) SM expectation. In Fig. 5.1 the example distributions of $\sum(E - p_z)$ are shown for the $e^+p$ (left) and the $e^-p$ (right) sample. Both data and

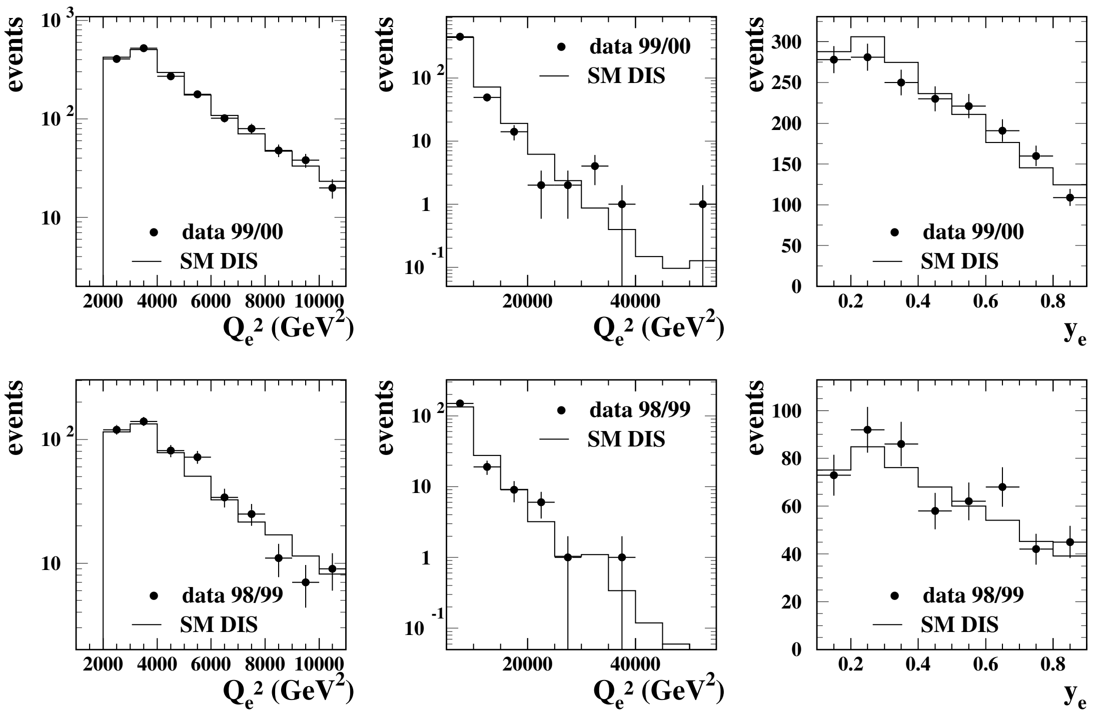


Figure 5.2: $Q_e^2$ (left and middle) and $y_e$ (right) in $e^+p$ (top) and $e^-p$ (bottom) collisions. In the left panel the $Q_e^2$ distributions are shown for lower values; the middle panel gives the distributions for highest $Q_e^2$ values.

SM background show a peak at $\sum(E - p_z) = 2E_e^0 \approx 55\,\mathrm{GeV}$ as expected for NC DIS. The distributions of the variables $Q_e^2$ and $y_e$ for data and SM expectation are shown in Fig. 5.2 for both the 1999/2000 data period (top) and the 1998/1999 data period (bottom). The SM expectation is mainly NC DIS, which is determined using the DJANGO generator with CTEQ5L structure functions. The contribution from photoproduction is negligible. The 1999/2000 data sample shows a small deficit around $Q_e^2 = 15\,000\,\mathrm{GeV}^2$ and a small excess around $Q_e^2 = 35\,000\,\mathrm{GeV}^2$. These kinds of deviations are also seen in other analyses performed in H1 [54, 70] and can be explained by statistical fluctuations. The $Q^2$ distributions of the 1998/1999 data and both $y_e$ distributions are in agreement with the SM prediction. As mentioned in Sec. 4.5.1 the trigger efficiency for electrons in this kinematic domain is compatible with 100 %.

### Exploiting the differences in angular event distributions

In order to further enhance the squark signal over the SM background, the angular distributions of the events can be exploited. In Fig. 5.3 the differences in $y_e$ and $M_e$ are illustrated for events from NC DIS (left) and from squark decay (right) fulfilling the selection criteria described above. Squarks, which are scalar particles, produced in the $s$-channel decay isotropically in their rest frame leading to a flat $d\sigma/dy$ distribution since

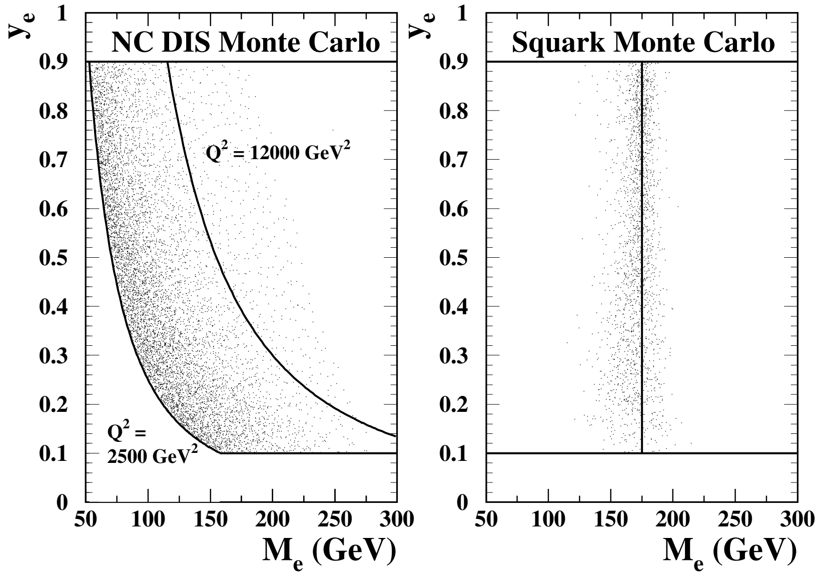


Figure 5.3: Distributions of events in the $(y_e, M_e)$-plane for NC DIS Monte Carlo (left) and Monte Carlo events from a squark of mass 175 GeV decaying into $e + q$ (right). Two isocurves at $Q^2 = 2\,500\,\mathrm{GeV}^2$ and $12\,000\,\mathrm{GeV}^2$ are plotted as full lines.

the variable $y$ (Eq. 2.8) can be written as $y = \frac{1}{2}(1 + \cos\theta^\star)$, where $\theta^\star$ is the decay polar angle of the lepton relative to the incident proton in the squark centre of mass frame. In contrast the $d\sigma/dy \propto y^{-2}$ distribution of NC DIS events[2] is markedly different.

In addition, the $M_e$ distributions of NC DIS events and events from squark decays are different. Squark decays into $eq$ proceeding directly via $\not{R}_p$ lead to a resonance peak in the $M_e$ distribution. With the electron reconstruction method the resolution in $M_e$ for scalar squarks is found to be between 4 and 8 GeV depending on the squark mass. Compared to other commonly used kinematic methods for NC DIS at HERA [55], the $e$-method used here provides the best peak resolution in mass at high $y$.

The differences between the distributions in the $(y_e, M_e)$-plane are exploited by applying an optimised lower $y_e$–cut which depends on the reconstructed squark mass. In this optimisation the expected limit[3] of the selection has been calculated as a function of the lower $y_e$–cut by considering the distributions of the SM background and the squark signal for squark masses in steps of typically 25 GeV. For a given squark mass the optimal cut value minimises the expected limit.

This procedure is illustrated in Fig. 5.4 (left) for a squark mass of 175 GeV. In this Fig.

[2] This relation can easily be derived for the dominant QED contribution from Eq. 2.10 and Eq. 2.11.

[3] The expected limit is defined as the exclusion limit at a given confidence level (CL) if data and prediction are identical. For a certain cut value it has been calculated by $(X_{\mathrm{exp}} - X_{\mathrm{bgr}})/\varepsilon$, where $\varepsilon$ denotes the selection efficiency, $X_{\mathrm{bgr}}$ is the number of background events and $X_{\mathrm{exp}}$ is calculated as $X_{\mathrm{exp}} = \sum_{n=1}^{\infty} P_{\mathrm{pois}}(X_{\mathrm{bgr}}, n) \cdot P_{\mathrm{pois}}^{\mathrm{inv}}(n)$. Here $P_{\mathrm{pois}}(X_{\mathrm{bgr}}, n)$ is the Poisson probability to find $n$ events, if $X_{\mathrm{bgr}}$ are expected. $P_{\mathrm{pois}}^{\mathrm{inv}}(n)$ gives the lower limit of a Poisson distribution with CL=0.05. $P_{\mathrm{pois}}^{\mathrm{inv}}(n)$ is calculated such that $\sum_{i=0}^{i\leq n}(P_{\mathrm{pois}}(i)) \equiv 0.05$.

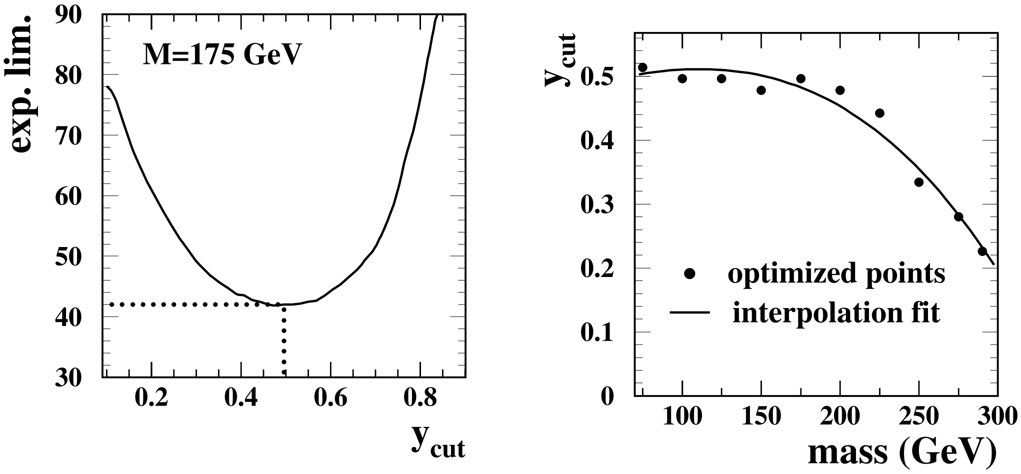


Figure 5.4: The expected limit as a function of the lower $y_e$–cut for a generated squark mass of 175 GeV (left) and the optimized lower $y$-cut for the full mass range (right).

the expected limit is shown as a function of the lower $y_e$–cut. For a certain squark mass the optimal choice of the cut value $y_{\mathrm{cut}}$ corresponds to the minimum of the expected limit. For the full mass range accessible at HERA the results of this optimisation procedure are shown in Fig. 5.4 (right). For low squark masses the optimised lower $y_e$–cut values are rather stable and decrease for higher masses. A fit function is used for the interpolation between the mass points for which the optimisation procedures has been done.

### Exclusivity with respect to $eMJ$

As explained in Sec. 2.6 an exclusive selection must be ensured for the limit derivation. For the $eq$ selection channel a possible overlap of events with the channels leading to an electron and multiple jets ($eMJ$, $elMJ$ and $e\nu MJ$) must be prevented. The selection criteria for these channels are rather complicated (cf. Chap 6). They roughly correspond to the requirement of two jets with each $p_{T,\mathrm{jet}} > 15\,\mathrm{GeV}$. All events finally accepted in one of these selection channels are not accepted in the $eq$ selection. With this additional requirement approximately 10 % of the events, accepted in the $eq$ selection channel before the cut, are rejected.

### Mass spectra

The $M_e$ spectra for data and SM background, which have been obtained after the optimized $y_e$–cut and the exclusivity cut, are shown in Fig. 5.5 (top) for $e^+p$ collisions and in Fig. 5.5 (bottom) for $e^-p$ collisions. No significant deviation from the SM expectation has been found in either data taking period. In particular no significant peak in the mass distributions, expected for the squark signal (dashed histogram), is observed in the data. 632 events are found in the $e^+p$ data set, while $628 \pm 46$ are expected from SM processes.

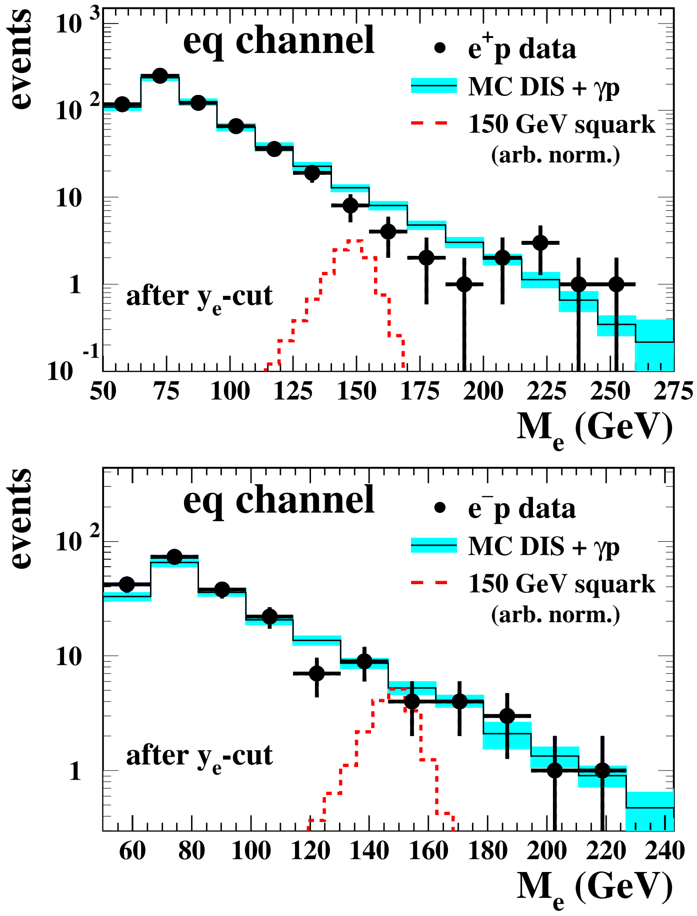


Figure 5.5: Mass spectra of the $eq$ selection in $e^+p$ collisions (top) and $e^-p$ collisions (bottom). The shaded error band indicates the systematic uncertainty on the SM background. The hypothetical signal from a squark of 150 GeV is given in arbitrary normalisation by the dashed histogram. Events selected in a selection channel with an electron and multiple jets (Chap. 6) are not included in the spectra.

In the $e^-p$ data 204 are seen, while $192 \pm 14$ is the SM prediction. To summarise, in this channel no hint for the production of $u$-type or $d$-type squarks is found.

For the evaluation of the uncertainty on the SM expectation the systematic uncertainties given in Sec. 4.7 are taken into account. For low and intermediate squark masses the error arising from the limited knowledge of the proton structure gives the biggest contribution to the total systematic uncertainty in this search channel. For higher masses the uncertainty on the electromagnetic energy scale contributes most. However, in this kinematic regime the statistics are already very limited, resulting in a statistical error which exceeds the systematic uncertainty, as can be seen in Fig. 5.5.

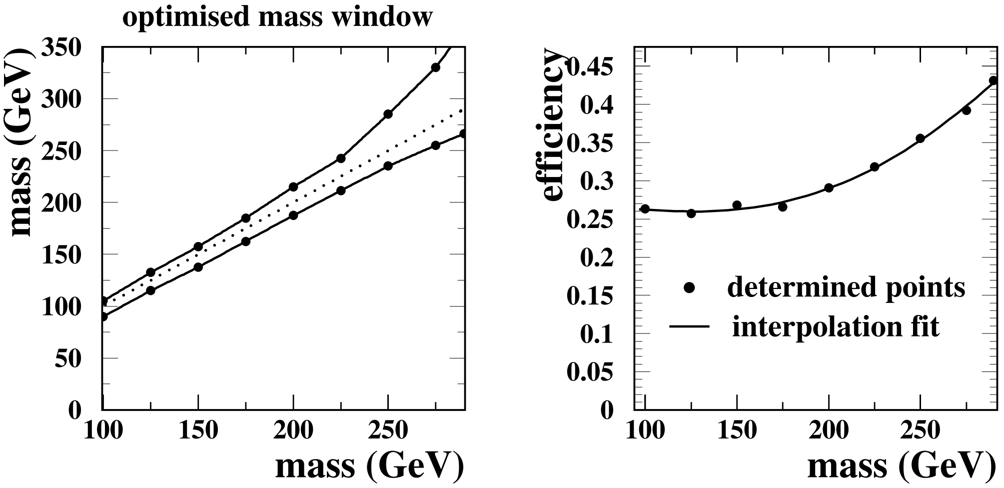


Figure 5.6: The optimal mass window for the sliding mass window method (left) and the signal efficiency of the final $eq$ selection.

### 5.1.2 Selection efficiencies

To further reduce the contribution from NC DIS background in the calculation of mass dependent limits we make use of a *sliding mass window method* where the number of observed and expected events are integrated within a mass bin which slides over the accessible mass range. For a given squark mass the mass bin has been determined by optimising the expected limit. In analogy to the procedure used for the optimized $y_e$–cut the expected limit is calculated and minimized as a function of the upper and lower mass cuts. The results of this optimisation are shown in Fig. 5.6 (left). The width of the mass window is rather small for low squark masses and increases towards higher masses where the mass resolution degrades. For the highest masses the upper mass cuts tends to higher values since the number of expected events decreases towards higher masses (see Fig. 5.5) and a better limit can be achieved by including the full squark signal peak in the mass window and accepting a small increase of the SM background. On the other hand the lower mass cut remains very restrictive since a substantial background contribution is expected at smaller masses.

For the mass dependent determination of the efficiencies in the $eq$ channel, needed in the limit calculation, event samples of directly $\not{R}_p$ squark decays into $e + q$ have been studied with squark masses ranging from 100 GeV to 290 GeV and a negligible intrinsic squark width. In the right panel of Fig. 5.6 the signal selection efficiency is presented as a function of the squark mass after the optimised lower $y_e$–cut and after the optimised mass window cut. The efficiency in this slelction channel ranges from 27% at low squark masses up to 43% at high squark masses. In particular at low squark masses the efficiency is reduced by the mass window and the rather harsh cut on $y_e$ (cf. Fig 5.4). A $5^{th}$ order polynomial is used to interpolate between the points for which the efficiency is explicitly determined.

The signal efficiencies presented in Fig. 5.6 (right) have been determined for the 1999/2000 data taking period. Because of differences in the calibration constants or potential instabilities in the data taking (e.g. dead wires in the CJC or dead trigger cells in the LAr) the efficiency could depend on the data taking period. However, it has been checked that the differences of the efficiencies between the two periods 1998/1999 and 1999/2000 is less than 1 %. This difference has been considered in the systematic uncertainty of the signal efficiencies.

### 5.1.3 Systematic uncertainties on selection efficiencies

In addition to the error arising from the limited statistics of signal MC, we assign a relative uncertainty of 10 % to the signal selection efficiencies, which is very conservative. This value includes the error coming from the interpolation procedure, the uncertainty which arises from the fact that the efficiency is determined for 1999/2000 detector conditions only and the uncertainty coming from the correction of the efficiencies for a non-negligible squark width at high masses (see Sec. 8.3).

An additional systematic error on the selection efficiencies arises from the theoretical uncertainty on the signal cross section, originating mainly from the uncertainties on the parton densities. This uncertainty is 7 % for $\tilde{d}_R^k$ squarks coupling to $e^-u$. The corresponding error for the production of $\tilde{u}_L^j$ which couples to $e^+d$ varies between 7 % at low squark masses up to 50 % around 290 GeV. Furthermore, choosing alternatively $Q^2$ or the square of the transverse momentum of the final state lepton in lepton–quark decays of squarks instead of $M_{\tilde{q}}^2$ as the hard scale at which the parton distribution are estimated yields an additional uncertainty of ±7 % on the signal cross section.

These sources of systematic errors are considered for the efficiencies of all squark decay channels. Experimental errors like the uncertainty of the luminosity measurement or the detector calibration are considered in the uncertainty of the SM background only (see Sec. 4.7).

## 5.2 Neutrino–quark channel

Squarks decaying directly via an $\not{R}_p$ coupling can lead to a neutrino and a jet in the final state. Since only the $\tilde{d}_R^k$, potentially produced in $e^-p$ collisions, can decay into $\nu_e + d^j$ (see Eq. 2.45), this selection channel is investigated in the 1998/1999 data sample ($e^-p$ collisions) only.

### 5.2.1 Event selection

Squarks undergoing a directly $\not{R}_p$ decay into $\nu q$ lead to CC DIS-like events with high missing transverse momentum since the final state consists of $\nu + q$ and the neutrino escapes detection. For the kinematic reconstruction and the selection of events in this channel we make use of the reconstruction method using the Jacquet-Blondel ansatz [71]. Here the usual kinematic variables for DIS reactions are given by

$$y_h = \frac{\sum (E - p_z)_h}{2E_e^0}, \quad Q_h^2 = \frac{p_{T,h}^2}{1 - y_h}, \quad x_h = \frac{Q_h^2}{y_h s}, \quad M_h = \sqrt{x_h s}\ , \tag{5.2}$$

where $p_{T,h}$ and $\sum (E - p_z)_h$ are calculated as in Eq. (4.3) and Eq. (4.2), but restricting the summations to all measured hadronic final state energy deposits.

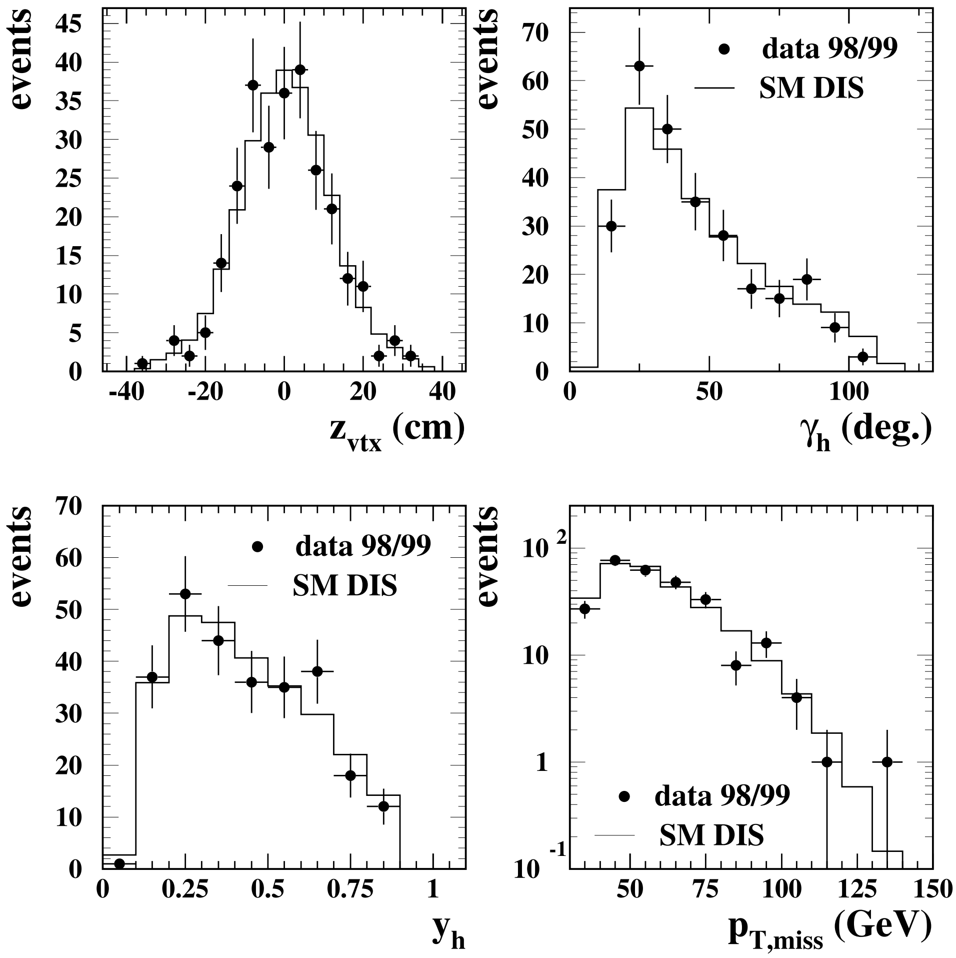


FIGURE 5.7: Distributions in the 1998/1999 data set ($e^-p$): Shown are the vertex position $z_{\text{vtx}}$ (top, left), the inclusive hadron angle $\gamma_h$ (top, right), $y_h$ (bottom, left) and $p_{T,\text{miss}}$ (bottom, right).

The selection criteria for the $\nu q$ channel are the following:

- The missing transverse momentum must be greater than 30 GeV.
- No electron must be found with $p_T > 5$ GeV.
- Again the comparison with SM expectation is restricted to the kinematic range $Q_h^2 > 2\,500\,\text{GeV}^2$ and $y_h < 0.9$. The resolution in both $M_h$ and $Q_h^2$ degrade with increasing $y$ since both $\delta M_h/M_h$ and $\delta Q_h^2/Q_h^2$ behave as $1/(1-y_h)$ for $y_h \approx 1$ [55]. For this reason the high $y_h$ domain is excluded.

This analysis makes use of the standard subtriggers[4] developed for H1 charged current analyses. Since the CC event sample is very small, the efficiency of these subtriggers has

[4]ST66, ST67, ST71 and ST77

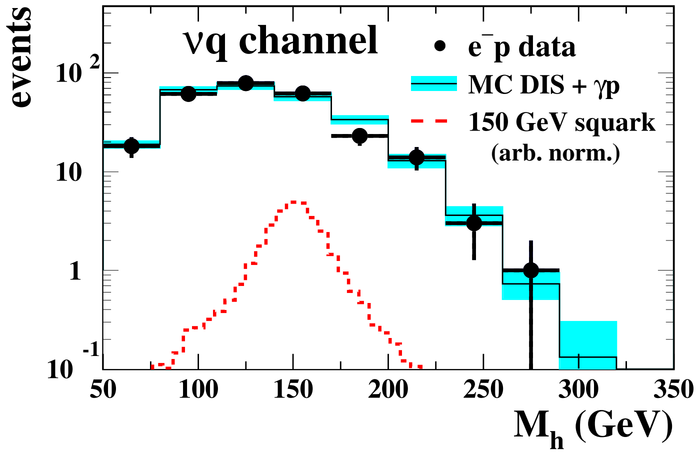


FIGURE 5.8: Mass spectrum for the $\nu q$ channel in $e^-p$ collisions. Events accepted in the selection channel $\nu MJ$ (Chap. 7) are not included. The dashed histogram indicates the signal of a squark with a mass of 150 GeV.

been checked in [55] using a so called *pseudo*–CC technique: Events from a NC sample have been converted to a pseudo CC sample by deleting all informations coming from the identified scattered electron and by reweighting the events to the CC cross section. It has been shown that the CC trigger efficiency is generally very high (around 97 %) in the kinematic range relevant for the analysis presented here. It has been corrected for by applying weights for the SM background events.

In Fig. 5.7 example distributions for selected events are shown. The upper panels show the vertex position $z_{\rm vtx}$ and the inclusive hadron angle $\gamma_h$ given by $\tan\frac{\gamma_h}{2} = \frac{\sum(E-p_z)_h}{p_{T,h}}$. In the lower panels the distributions of $y_h$ and $p_{T,\rm miss}$ are illustrated. The data are well described by the SM prediction which mainly consists of CC DIS. The contribution from photoproduction at these high values of $p_{T,\rm miss}$ is negligible.

In addition further cuts are applied to ensure an exclusive selection. With respect to the selection channel $\nu MJ$ (Chap. 7) all events with two or more jets with each $p_{T,\rm jet} > 15$ GeV in the angular range $7° < \theta_{\rm jet} < 145°$ are rejected. Events containing a muon with $p_{T,\mu} > 5$ GeV are rejected as well. The amount of events affected by these additional cuts is however small; about 3.5 % of the events are removed from the sample.

### Mass spectrum

In the $e^-p$ data set we find 261 events with $269 \pm 21$ expected from the SM. The resulting $M_h$ spectra for data and SM background are shown in Fig. 5.8. Events coming from squark decays (dashed histogram) should be clustered in the $M_h$ distributions with a resolution of 10 to 20 GeV depending on the squark mass. No significant deviation from SM expectation has been found. The systematic uncertainties on the SM expectation considered are explained in Sec. 4.7. At small squark masses the error due to the limited knowledge of the proton structure functions contributes most. At high masses the contribution from the uncertainty of the hadronic energy scale is most relevant but still smaller than the

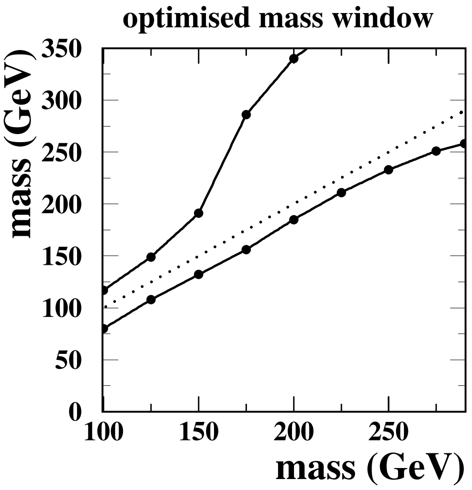


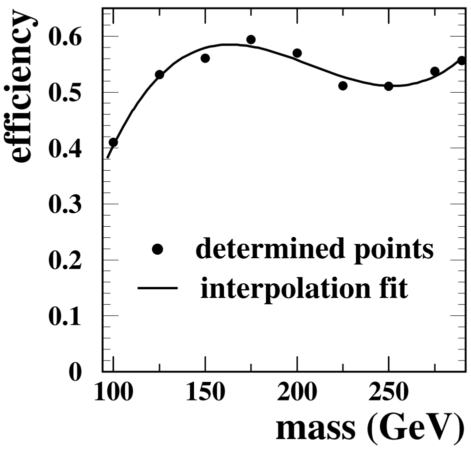


FIGURE 5.9: Optimal mass window (left) and signal efficiency for the $\nu q$ channel (right).

statistical errors (see Fig. 5.8).

### 5.2.2 Selection efficiencies

The SM background contribution for this final state is considerable. For this reason the sliding mass window method (cf. Sec. 5.1.2) is again used in the calculation of mass dependent exclusion limits. The mass window in which data, background and signal are integrated during the limit calculation has again been determined by optimising the expected limit as a function of the upper and lower mass cuts. The results of this optimisation procedure are shown in Fig. 5.9 (left). For low squark masses the optimal mass window is rather small, whereas for higher values it becomes very broad. Similarly to the behaviour of the mass window in the $eq$ channel (Fig. 5.6) for high squark masses the upper mass cut tends to high values and actually means no longer a restriction. A better limit can be achieved by including the full resonance peak in the mass window since the SM expectation for higher masses is low. In contrast, the lower mass cut is more restrictive since at lower masses the SM background is considerable.

To determine mass dependent efficiencies in the $\nu q$ channel, events from $\not{R}_p$ squark decays leading to $\nu + q$ have been generated with squark masses ranging from 100 GeV to 290 GeV and with an intrinsic squark width set to negligible values. The efficiency after the optimal mass window cut is shown in the right panel of Fig. 5.9 as a function of the squark mass. For very small squark masses the efficiency is around 40 %. Sensitivity is lost by the rather stringent cut on $p_{T,\text{miss}}$. For masses $\gtrsim$125 GeV the efficiency reaches higher values and it is rather constant at approximately 55 %. Since the lepton–quark channels contribute only at very high squark masses (i.e. at high values of $\lambda'$) the loss of efficiency for small squark masses is unimportant. The systematic uncertainties on the efficiencies for the $\nu q$ channel are identical to those considered for the $eq$ channel (Sec. 5.1.3).

# Chapter 6

# Channels with an Electron or Positron and Multiple Jets

In gauge decay modes the squark decays without $\not{R}_p$ into a quark and a gaugino (cf. Fig. 2.10 and Fig. 2.11). The latter decays either involving a second gaugino in the decay chain (cascade gauge decay, cf. Fig. 2.12) or violating $R_p$ into two SM quarks and a lepton of the first family (direct gauge decay, cf. Fig. 2.16 and Fig. 2.17). Thus, gauge decays lead to final states with multiple jets. In this chapter the results for all gauge decay modes leading to final states with an additional charged lepton of the first family are presented. As explained in Sec. 2.5.3, these topologies are most relevant (high branching ratios) in SUSY scenarios, where the lightest neutralino $\chi_1^0$ is predominantly photino-like.

In the first section a loose selection of events with an electron and multiple jets is presented. This sample allows tests of different models of QCD radiation in the Monte Carlo to be carried out. In the following parts the selection steps of a more restrictive preselection are described. The latter is used for the channels $e^+MJ$, $e^-MJ$, $\nu eMJ$, $e\mu MJ$ and $eeMJ$ in Tab. 2.6. Finally, these channels are separately discussed in more detail and the corresponding signal efficiencies are presented.

## 6.1 Preparatory analysis and common preselection

### 6.1.1 Loose selection of events with an electron and several jets

In the analysis of final states with electron and multiple jets an initial loose event selection has been carried out in both data sets ($e^+p$ and $e^-p$) separately:

- **At least two jets** must be found with transverse momentum $p_{T,\text{jet}} > 15\,\text{GeV}$. To ensure that the jets are well measured and well contained in the LAr, the polar angular range is restricted to $7^\circ < \theta_{\text{jet}} < 145^\circ$.

  Although all gauge decay modes lead to at least three quarks in the final state, only two jets are required. A higher number would significantly reduce the signal selection efficiencies because for mass configurations where all decay products are boosted in the forward direction (e.g. high squark mass and low gaugino masses) the jets are close to each other.

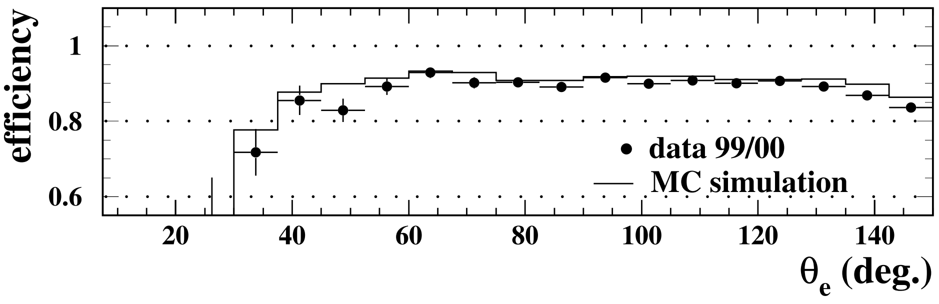


Figure 6.1: Track finding efficiency for tracks fulfilling the matching criterion of cluster and track energy measurement. Shown are the results in 1999/2000 data and MC simulation for a clean sample of high $Q^2$ NC DIS events as a function of the polar angle of the scattered electron. Results for 1998/1999 are found to be similar.

- **At least one electron** must be found with $p_{T,e} > 6\,\mathrm{GeV}$. It must be located in the angular range $5^\circ < \theta_e < 145^\circ$. The cut value chosen for $p_{T,e}$ is relatively small since for some SUSY mass configurations (e.g. small $\chi_1^0$ mass) it is possible that the electron gets a little energy. At small energies, however, the amount of hadronic background in the selection is substantial. To reduce it electrons must fulfill further quality criteria.

  – For **central electrons** ($\theta_e > 30^\circ$) a charged track in the central tracking system must be associated with an electromagnetic cluster having a DCA of less than 12 cm. For $e^+MJ$ and $e^-MJ$ the selection makes use of the charge measurement of the electron track in the CJC. Therefore electron tracks must fulfill additional quality criteria: the energy of the electromagnetic cluster and the energy measured from the curvature of the charged track in the jet chambers must match: The ratio of the transverse momentum of the track and that measured in the calorimeter must be greater than 0.5. These constraints strongly reduce the contribution of fake electrons from misidentified photons or hadrons.

    For the additional requirement of track and cluster energy matching, the track finding efficiency has been checked using the method described in Sec. 4.5.1. The results are explicitly shown in Fig. 6.1 for the 1999/2000 data period – for 1998/1999 the outcome is very similar. In the central part of the detector the track finding efficiencies are around 90 %. The differences between data and MC simulation are of the order of 3 %. They have been corrected for by applying $\theta_e$ dependent event weights to the MC events. For large polar angles the efficiency slightly degrades since the electron has only traversed a small distance in the sensitive detector volume of the CJCs. In the forward region ($\theta_e < 30^\circ$) the track finding efficiency is very low, due to the forward tracker problems already mentioned. For these reasons a charged track is required in the central region only, whereas in the forward part of the detector different methods must be applied to eliminate the background.

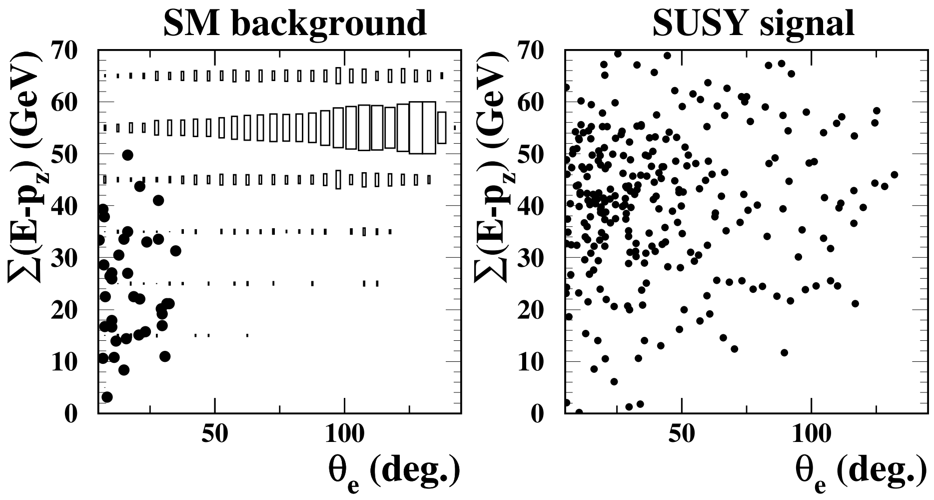


Figure 6.2: Distributions of MC events in the $(\sum(E-p_z), \theta_e)$-plane. In the left panel the SM background is shown: NC DIS (box histogram) and $\gamma p$ (dots, arb. norm.); The right panel illustrates the SUSY signal. Events with low $\sum(E-p_z)$ and electron candidates in the very forward direction are rejected. The SUSY signal is shown for squark decays leading to $\nu eMJ$ topologies where the cut should have the biggest effect.

– To discriminate against photoproduction background where hadrons faking **electrons in the forward region** ($\theta_e < 30^\circ$), electron candidates found in this region have to fulfill harsher isolation criteria[1] than normally used. In $\gamma p$ events, hadrons misidentified as electrons are usually located in a dense hadronic environment and can therefore be rejected.

  In addition, for events with a forward electron candidate, the total $\sum(E-p_z)$ of must be greater than 30 GeV. In Fig. 6.2 (left) the correlation of $\theta_e$ and $\sum(E-p_z)$ is shown for MC events before the latter cut. Events from NC DIS are nicely distributed around twice the energy of the incoming electron $\sum(E-p_z) = 2E_e^0 \approx 55\,\text{GeV}$. In contrast the bulk of faked electron candidates in $\gamma p$ events are located in the forward part of the detector and the total $\sum(E-p_z)$ of the events is low[2]. Roughly 50 % of the photoproduction background can be eliminated by this cut.

  The additional loss of signal efficiency by these cuts is very small for all channels to which this preselection is applied. Even for the $\nu eMJ$ topology the $\sum(E-p_z)$ is relatively high since the neutrino is usually emitted in the forward direction where the loss in $E-p_z$ is small. This is demonstrated in Fig. 6.2 (right) where the distribution of signal events from the $\nu eMJ$ topology is shown for a high squark mass configuration. As a result the electron is found at small values of

[1]The minimum distance in the $(\eta, \phi)$-plane of the electron candidate to the nearest calorimeter cluster with a transverse energy greater than 0.5 GeV must exceed 0.35.

[2]In $\gamma p$ events the *real* electron escapes through the beam pipe in the backward direction. This leads to an $\sum(E-p_z)$ loss since the $E-p_z$ of the electron is not measured.

$\theta_e$. For lower masses, the loss in $\sum(E - p_z)$ is increased, but on the other hand the electron is more central.

### 6.1.2 Test of QCD models and control of SM background

To describe QCD radiation and the production of jets in the MC two different models are commonly used. In the DJANGO generator [35] QCD radiation is based on the Colour Dipole Model (CDM) [37], whereas RAPGAP [38] relies on first order matrix elements and uses leading-log parton showers (MEPS) [39]. It is known that the Colour Dipole Model has problems describing the data of jet production in the particular phase space domain this analysis is dealing with [69]. Furthermore it has been observed in [72] and [73] that the matrix element and parton shower model underestimates the jet production rate by roughly 20 %. This can be corrected for by applying additional weighting factors to the MEPS Monte Carlo.

The performance of the two models is demonstrated in Fig. 6.3 showing several example control distributions for events fulfilling the loose selection of Sec. 6.1.1. Shown are the distributions of the polar angle $\theta$ (panels on the left) and the transverse momentum $p_T$ (panels on the right) of the objects in the 1999/2000 data set and the predictions of CDM (dashed histograms) and MEPS (globally weighted by 1.2, full histograms). The amount of photoproduction background has been evaluated using the PYTHIA [42] event generator, which is also based on matrix elements and uses leading-log parton showers and hence must be weighted by 1.2. The contribution of $\gamma p$ events is given by the hatched histograms.

The CDM has indeed problems describing the data distributions. In particular it underestimates the data at high values of the transverse momentum $p_{T,e}$ of the electron and at small values of the polar angle $\theta_{\mathrm{jet2}}$ of the second highest jet in $p_T$. In contrast the MEPS model gives a reasonable description of the data distributions throughout the full kinematic range. For this reason the MEPS model is used to simulate the NC DIS background in channels containing jets in the following.

The different performance of the two QCD radiation models is considered by assigning a model uncertainty of $\pm 10$ % on the predicted SM cross section for multijet final states. This value is estimated from the differences between MEPS and CDM and is of the same order of magnitude as assumed in [11] and [69].

The good description of the data distributions in Fig. 6.3 as well as others (e.g. Fig. 6.4) by the SM Monte Carlo gives confidence that the data are in general well understood in terms of NC DIS (MEPS) and photoproduction (PYTHIA) up to a normalisation factor of 20 %. Even the very forward region, where fake $\gamma p$ events are mainly located, is well simulated. After the loose selection of Sec. 6.1.1 we find 722 (171) events in the 1999/2000 (1998/1999) sample with $732 \pm 98$ ($169 \pm 23$) being expected from the SM (MEPS+PYTHIA).

### 6.1.3 Common preselection

To further reduce the SM background a more restrictive preselection for the channels $e^+MJ$, $e^-MJ$, $\nu eMJ$ , $e\mu MJ$ and $eeMJ$ in Tab. 2.6 has been carried out. In addition to the loose selection criteria presented in Sec. 6.1.1 further cuts are applied.

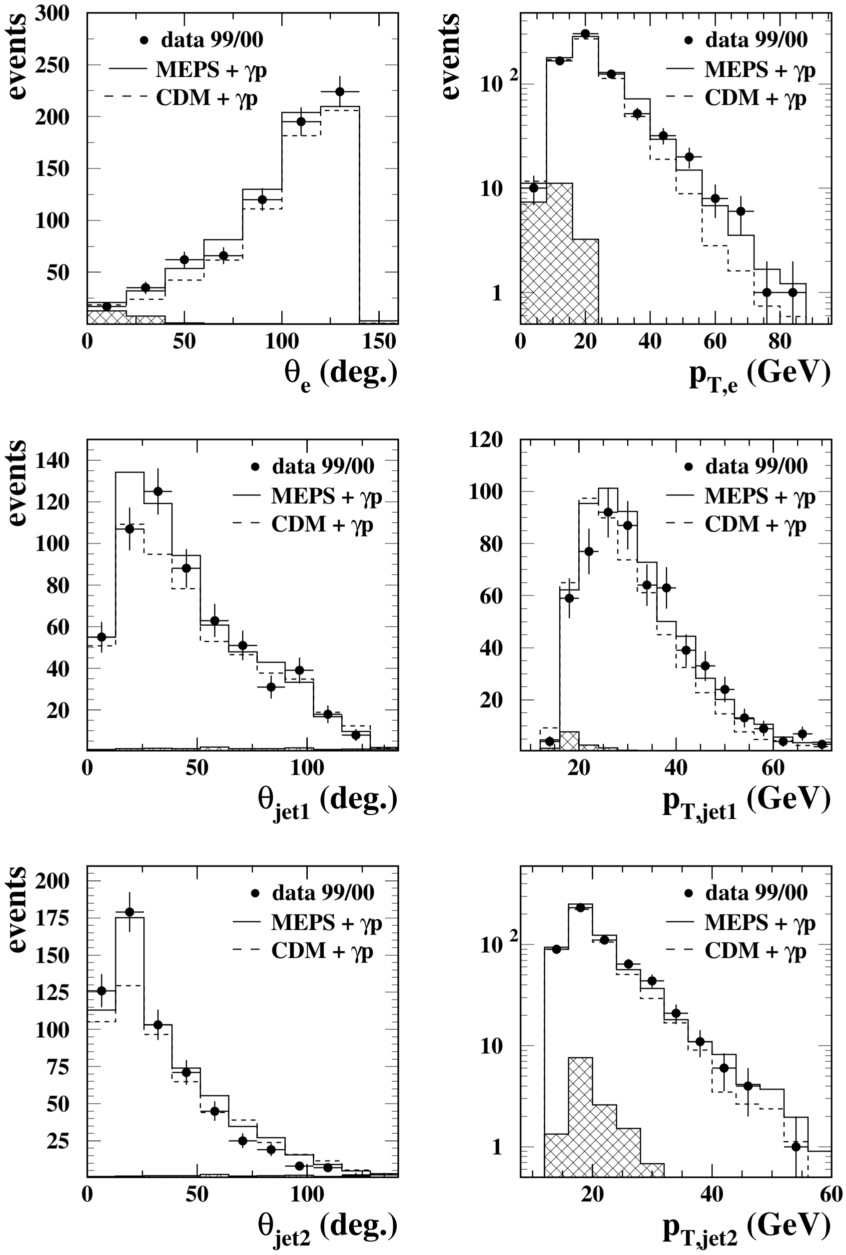


Figure 6.3: Test of MC QCD radiation models after the loose selection of Sec. 6.1.1 selecting events with an electron and two jets. Shown are the polar angle $\theta$ (left) and the transverse momentum $p_T$ (right) of the objects. The NC DIS background predicted by CDM and MEPS (weighted by 1.2) is illustrated by the dashed and full histograms, respectively. The contribution from photoproduction is given by the hatched histograms (PYTHIA, weighted by 1.2). The distributions are shown for 1999/2000 – results for 1998/1999 are similar.

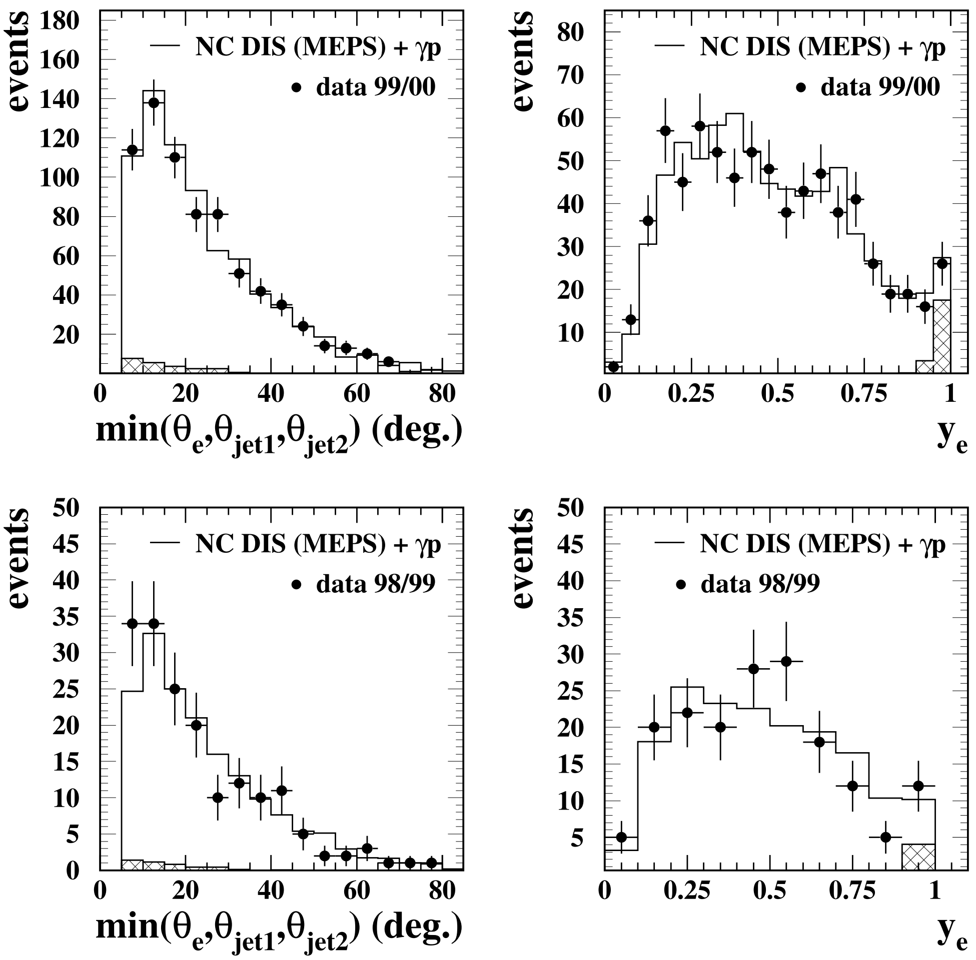


Figure 6.4: $\min(\theta_e, \theta_{\rm jet1}, \theta_{\rm jet2})$ (left) and $y_e$ (right) in 1999/2000 (top) and 1998/1999 (bottom) after the loose selection of Sec. 6.1.1.

- Since electrons from squark decays are generally emitted into the forward direction the polar angular range of the electron is restricted to the range $5^\circ < \theta_e < 110^\circ$ and $Q_e^2$ must exceed $1000\,\mathrm{GeV}^2$.

- The minimum of the polar angles of the highest $p_T$ electron and of the two jets with highest $p_T$ must fulfill $\min(\theta_{\rm e}, \theta_{\rm jet\,1}, \theta_{\rm jet\,2}) < 40^\circ$. This cut ensures that one of the squark decay products is emitted in forward direction since in general the decay products in squark decays are boosted forward. The distributions of this variable after the loose selection of Sec. 6.1.1 are shown in Fig. 6.4 (left) for events with exactly two jets. Data from $e^+p$ (top) and $e^-p$ (bottom) collisions are described by the SM background MC, which is evaluated using RAPGAP (MEPS) for NC DIS and PYTHIA for $\gamma p$ events – both weighted by a factor of 1.2.

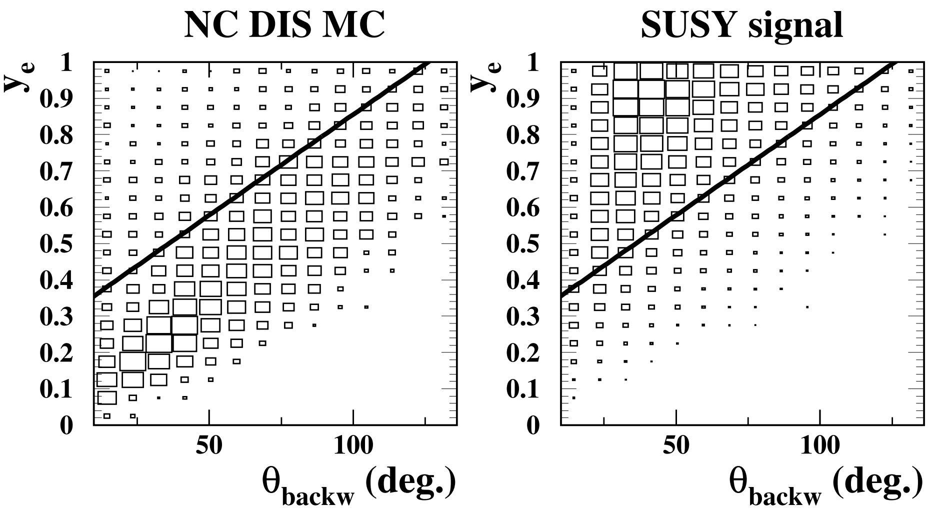


Figure 6.5: Distributions of events in the $(y_e, \theta_{\text{backw}})$-plane after the loose selection of Sec. 6.1.1. Shown are NC DIS Monte Carlo events (left) and SUSY Monte Carlo events (right) where a squark undergoes a gauge decay leading to $e+$ multijets$+X$ final states for a typical mass configuration of the SUSY particles. Only events above the diagonal line are selected.

- Of the two highest $p_T$ jets, the one with the larger polar angle $\theta_{\text{backw}}$ must satisfy $(y_e - 0.3) > (\theta_{\text{backw}}/\pi)$. The control distributions of $y_e$ after the loose selection of Sec. 6.1.1 are shown in Fig. 6.4 (right) for the 1999/2000 (top) and 1998/1999 (bottom) sample. The data are well described by the simulation of NC DIS and $\gamma p$ events – the latter clustered at high values of $y_e$ where the signal is also expected. The discriminating power of the cut is illustrated in Fig. 6.5, where the correlation between $y_e$ and $\theta_{\text{backw}}$ is shown for NC DIS events and events coming from squark decays, which fulfill the loose selection of Sec. 6.1.1. The SUSY signal corresponds to a typical mass configuration considered in this analysis. Events above the lines are selected. The cut allows an effective reduction of the SM background, while the efficiency loss is rather small.

Note that up to this stage of the selection, no criterion of balanced events ($p_{T,\text{miss}}$ or $\sum(E - p_z)$) is imposed since in some of the subchannels, treated with this common preselection, neutrinos are produced. In the following the individual selection cuts applied in the various subchannels, are described. These cuts ensure an exclusive selection: any given event (data, background or signal) can only contribute to a single selection channel.

## 6.2 'Wrong' and 'right' charge channel

As can be seen in Tab. 2.6 squarks decaying via a gauge decay chain can lead to final states with multiple jets and a charged lepton of the first family. This lepton could be either an electron or a positron. Both charges can appear in the decay chains of $\tilde{u}^j_L$, which could be produced in $e^+p$ collisions, and $\tilde{d}^k_R$, potentially produced in $e^-p$ collisions. The two channels are called 'wrong' or 'right' charge channels, if the charge of the identified lepton is identical or different from the charge of the initial beam. The 'wrong' charge channel is of particular interest since its investigation represents a striking test of lepton number violation. Therefore it is expected to be almost free of SM background.

The **selection** of both channels 'wrong' charge and 'right' charge) is based on the common preselection described in Sec. 6.1.3. Only jets and the charged lepton are expected in the event (see Tab. 2.6). Thus no particle with large $p_T$ should escape undetected. For this reason we ask for balanced events:

- $p_{T,\text{miss}} < 15\,\text{GeV}$;
- $40 < \sum(E - p_z) < 70\,\text{GeV}$.

To reach an exclusive selection with respect to the $eeMJ$ and $e\mu MJ$ selection channels, events with a second electron candidate with $p_{T,e} > 5\,\text{GeV}$ and $5^\circ < \theta_e < 110^\circ$ or a muon candidate with $p_{T,\mu} > 5\,\text{GeV}$ and $10^\circ < \theta_\mu < 110^\circ$ are rejected for both 'wrong' and 'right' charge channel. Further criteria are imposed separately for $e^+MJ$ and $e^-MJ$. These criteria concern the measurement of track charges in the central tracking system.

### 6.2.1 Charge measurement in the CJC

In H1 the charge of a track is measured from its curvature $\kappa$ in the Central Jet Chambers. This measurement is reliable only for polar angles with $\theta > 30^\circ$ where it is assured that the charged particle has traversed a sufficiently long part of the sensitive detector volume of the CJCs.

The description of the charge measurement by the simulation has been checked using the loose selection (Sec. 6.1.1) of events with an electron and multiple jets. For central electron tracks of this event sample the significance of the charge measurement $\frac{\kappa}{\Delta\kappa}$, coming from the H1 tracking system, is shown in Fig. 6.6. $\Delta\kappa$ denotes the error on the curvature measurement. Only the distributions for the 1999/2000 data taking period are shown explicitly – the results for 1998/1999 are very similar. The significance is multiplied by the charge of the track $Q_e$, so that only tracks with correctly[3] measured charge have positive values. The distributions reveal that the simulation of the CJC has problems exactly describing the charge measurement. At positive values of $(\frac{\kappa}{\Delta\kappa} \cdot Q_e)$ the data events are shifted to higher values than in the MC[4]. For wrongly measured electron tracks the statistics after the loose selection (Sec. 6.1.1) are already very limited. The tail towards negative values is described by the simulation within errors.

In this analysis only charge measurements with a significance greater than two standard deviations, $|\frac{\kappa}{\Delta\kappa} \cdot Q_e| > 2$, are accepted. In Fig. 6.6 the rejected region is indicated by the shaded area. With this cut the differences in data and MC have a negligible effect on correctly measured tracks. For wrongly measured electron tracks (negative values) the statistical uncertainty exceeds the systematic uncertainty of the charge measurement. In addition, in the final selection of the 'wrong' charge channel (cf. Sec. 6.2.3) no event is found in both data sets ($e^+p$ and $e^-p$). Thus, a possible underestimation of the SM

[3] with respect to the initial positron beam in 1999/2000

[4] The same behaviour has been found in the clean environment of inclusive high $Q^2$ NC events. This indicates that the shift is not a relict of the dense track environment in events with multiple jets.

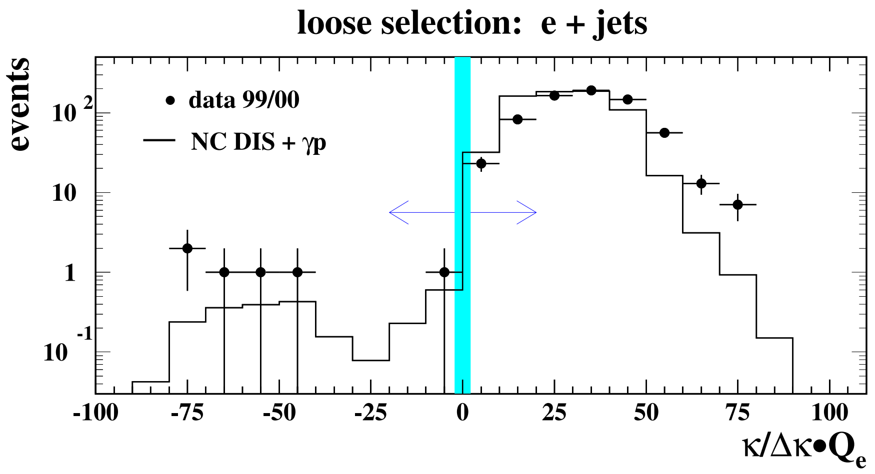


Figure 6.6: Charge measurement in the CJC. Shown is the significance of the curvature measurement times the electric charge ($\frac{\kappa}{\Delta\kappa} \cdot Q_e$) for central electron tracks ($\theta_e > 30°$) in events fulfilling the loose selection (Sec. 6.1.1) of events with an electron and multiple jets. The shaded area indicates the rejected region $|\frac{\kappa}{\Delta\kappa} \cdot Q_e| > 2$.

background for the 'wrong' charge channel has no consequences for the following steps (limit calculation). For these reasons an additional systematic error attributed to the uncertainty of the charge measurement is not taken into account.

### 6.2.2 'Right' charge channel

In the 'right' charge selection channel ($e^- MJ$ for $e^- p$ collision and $e^+ MJ$ for $e^+ p$ collision) events are accepted having either a central electron ($\theta_e > 30°$) with a charge measurement of the 'right' sign or an electron found in the forward direction ($\theta_e < 30°$). In the latter case the information from the charge measurement is ignored since it is not reliable.

Some example event distributions are shown in Fig. 6.7 for the two data sets. Shown is the polar angle of the electron/positron $\theta_e$ (left) and the invariant mass of the two jets with the highest transverse momentum $M_{1,2}$ (right) for events containing exactly two jets. For both data sets the distributions are well described by the MC which is mainly NC DIS using RAPGAP (MEPS) weighted by a factor of 1.2. The amount of remaining background from photoproduction is approximately 15 %. The contribution coming from the production of the heavy gauge bosons $Z^0$ and $W^{\pm}$ is around 1 %.

For events in this 'right' charge channel a mass $M_{\mathrm{inv}}$ is calculated which is a good estimator of the squark mass $M_{\tilde{q}}$:

$$M_{\tilde{q}} = \sqrt{4E_e^0 x E_p} \approx M_{\mathrm{inv}} = \sqrt{4E_e^0 \left( \sum_i E_i - E_e^0 \right)}. \tag{6.1}$$

Here the sum runs over all jets found in the event with $p_{T,\mathrm{jet}} > 5\,\mathrm{GeV}$ and all electrons thereby excluding the proton remnant. This reconstruction method yields a typical resolution of 7 to 10 GeV depending on the squark mass. This resolution is significantly smaller

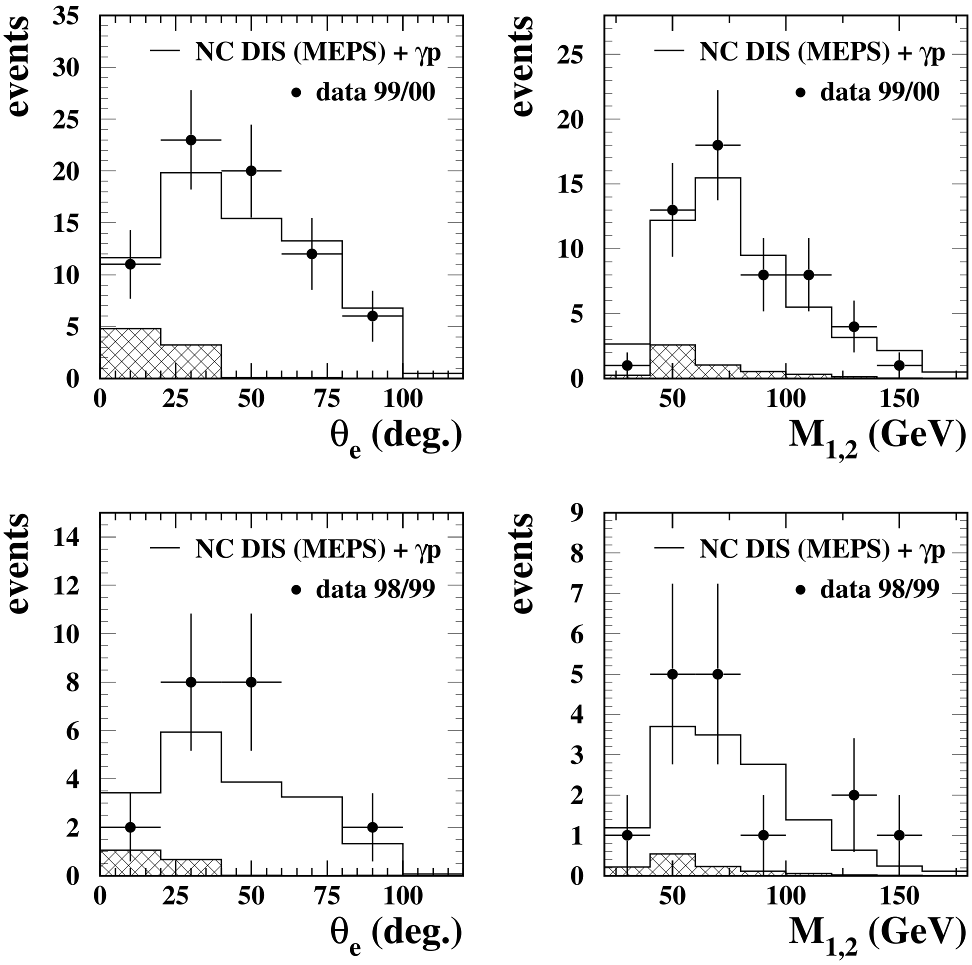


Figure 6.7: Example control distributions for the final $eMJ$ selection, 'right' charge. Shown are the polar angle $\theta_e$ (left) and the invariant mass of the two jets $M_{1,2}$ (right) in events with exactly two jets for the 1999/2000 (top) and 1998/1999 (bottom) sample.

than that obtained for a reconstruction method calculating the invariant mass of the jets and the electron/positron from their four-vectors.

The $M_{\rm inv}$ spectra for data and SM expectation of the 'right' charge channels $eMJ$ are shown in Fig. 6.8 for $e^+p$ (top) and $e^-p$ (bottom) collisions. No significant deviation from the SM has been observed. In particular no mass peak expected for potential squark production is visible in the data. The expected signal of a squark of 150 GeV (dashed histogram) is shown in arbitrary normalisation for demonstration purposes. The total number of selected data events in the 'right' charge channel is 72 in $e^+p$ collisions with $67.5 \pm 9.5$ predicted by the SM. In $e^-p$ collisions 20 events are found in total while $17.9 \pm 2.4$ are expected from the SM. The experimental and theoretical uncertainties on the SM background expectation outlined in Sec. 4.7 are considered. For this selection channel the uncertainty on the SM cross section for multijet final states (10 %) is most important.

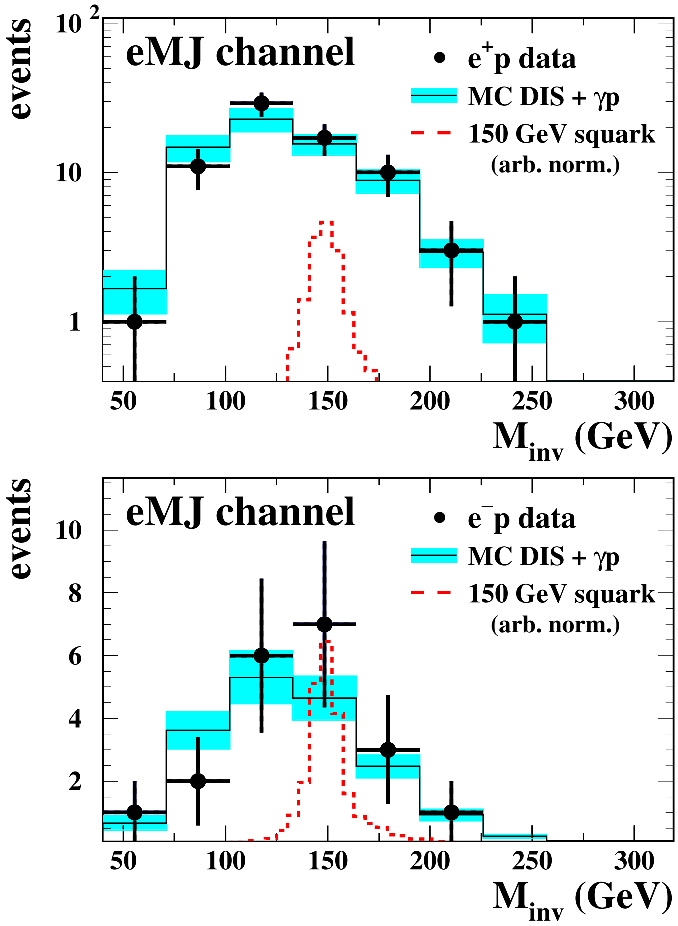


Figure 6.8: Invariant mass distributions in the $eMJ$ selection channel with 'right' charge for $e^+p$ collisions (top) and $e^-p$ collisions (bottom). The dashed histogram indicates the signal from a squark with a mass of 150 GeV using an arbitrary normalisation.

### 6.2.3 'Wrong' charge channel

Events are accepted in the channel having the 'wrong' charge lepton ($e^+MJ$ for $e^-p$ collision and $e^-MJ$ for $e^+p$ collision) if the electron/positron is found in the angular range $\theta_e > 30°$ and its charge is measured accordingly with $\frac{\kappa}{\Delta\kappa} > 2$. Events with an electron/positron in the forward region ($\theta_e < 30°$) are not accepted in order to keep this very striking selection channel for lepton flavour violation background free. All events with a forward electron are counted in the 'right' charge selection channel.

As expected the SM expectation in this channel is very low. In both data sets no event was selected while $0.20 \pm 0.14$ and $0.06 \pm 0.02$ are predicted by the SM for the $e^+p$ and $e^-p$ samples, respectively. Thus the data are in agreement with the SM and no hint for squark production has been observed. The dominant source of systematic uncertainty is the limited statistics of SM background MC. However, the errors are very small.

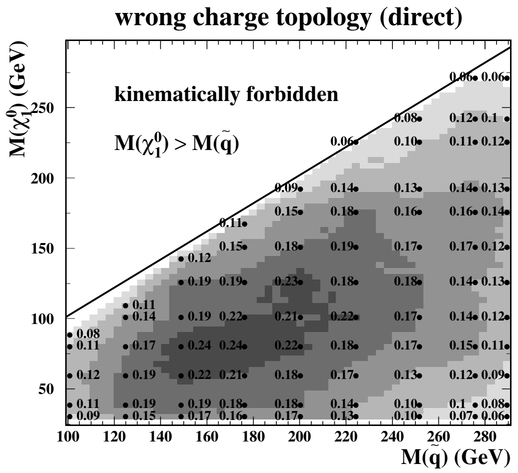


FIGURE 6.9: Selection efficiencies in the 'wrong' charge channel for direct gauge decays ($\tilde{q} \rightarrow q\chi_1^0 \rightarrow q\, e^{\pm}\bar{q}q$) as a function of the masses involved.

### 6.2.4 Selection efficiencies for 'right' and 'wrong' charge channel

As can be seen in Tab. 2.6, two different decay chains can lead to the event topologies of the 'right' and 'wrong' charge channels ($e^+MJ$ and $e^-MJ$). Both topologies can occur either in a direct squark decay (first line of the row "$e^{\pm}MJ$" in Tab. 2.6), which involves just one intermediate gaugino ($\tilde{q} \rightarrow qX \rightarrow q\, e\bar{q}q$), or in a cascade squark decay (second line), which involves two gauginos in the decay chain ($\tilde{q} \rightarrow qY \rightarrow q\, q\bar{q}X \rightarrow q\, q\bar{q}\, e\bar{q}q$) and usually has the highest BR.

To parameterise the selection efficiencies of the **direct decay channels** as a function of the masses the decay chain $\tilde{q} \rightarrow q\chi_1^0 \rightarrow q\, e\bar{q}q$ has been simulated with different combinations of squark and neutralino masses: the squark mass $M(\tilde{q})$ is varied between 100 GeV and 290 GeV in steps of typically 25 GeV. The neutralino masses range between 30 GeV and $M(\tilde{q})$ in steps of around 20 GeV. The latter mass restriction is given by kinematic constraints. The former is motivated by the exclusion domains resulting from $\chi$ searches in $\not{R}_p$ SUSY at LEP (e.g. [15]).

In Fig. 6.9 the selection efficiencies for the direct gauge decay chain leading to the 'wrong' charge channel are illustrated in the $(M(\tilde{q}), M(\chi_1^0))$-plane. The mass combinations considered allow a parameterisation of the efficiency in almost the entire kinematic range which is accessible at HERA. The rather small step size in mass allows a linear interpolation between the points that are explicitly generated (indicated by dots). In the small region which is not covered the efficiency is extrapolated very conservatively.

The efficiency reaches up to 25 % for intermediate squark and gaugino masses. In general, it is rather low since for this topology the selection is restricted to central electrons/positrons only in order to guarantee a reliable charge measurement. For lower squark and neutralino masses the efficiency degrades since the decay products (electron and jets) get little energy in the decay and are hard to detect. Towards high squark masses the selection efficiency decreases since for these cases the electrons are boosted into the forward direction and are not selected. For small mass differences $M(\tilde{q}) - M(\chi_1^0)$ one of the three

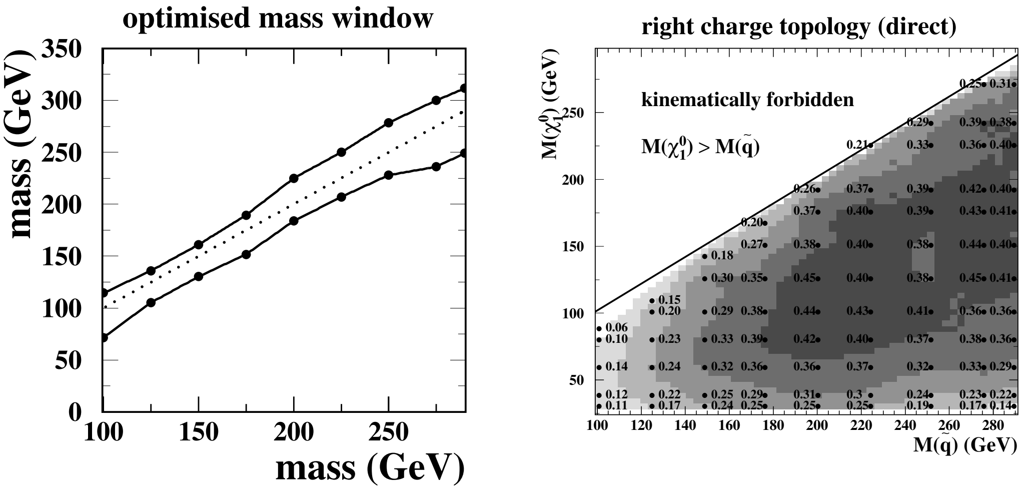


FIGURE 6.10: Optimal mass window (left) and selection efficiencies (right) for the $eMJ$ topology with 'right' charge in direct gauge decays ($\tilde{q} \rightarrow q\chi_1^0 \rightarrow q\,e^{\pm}\bar{q}q$) as a function of the masses involved.

quarks has small energy which leads to an efficiency loss.

The number of expected background events with 'wrong' charge is already very small. A further reduction by mass restrictions is not needed. In contrast the 'right' charge channel has a significant background contribution. To eliminate this background a sliding mass window method (Sec. 5.1.2) is applied. For a given squark mass the upper and lower mass cuts have been optimised using the signal and background distributions of 1999/2000. The optimal cut values are illustrated in Fig. 6.10 (left). The width of the optimal window increases since the mass resolution degrades for high masses. After applying this optimal mass cut the selection efficiencies entering the limit calculation can be determined and the results are shown in Fig. 6.10 (right). For small squark and neutralino masses the efficiencies are rather low, around 15 %. For these cases the squark decay products (electron and jets) get little energy in the decay and are hard to identify in the detector. However, the efficiency increases up to 45 % for higher masses. Towards the kinematic border, where $M(\tilde{q}) \approx M(\chi_1^0)$, the efficiency decreases because one jet has small energy.

To determine the mass dependent selection efficiencies of **cascade gauge decay** chains leading to the 'wrong' and 'right' charge topologies the particular process $\tilde{q} \rightarrow q\chi_1^{\pm} \rightarrow q\,q\bar{q}\chi_1^0 \rightarrow q\,q\bar{q}\,e^{\pm}\bar{q}q$ is used. The squark mass is again varied between 100 GeV and 290 GeV, $\chi_1^{\pm}$ masses range between 30 GeV and $M(\tilde{q})$, and $\chi_1^0$ masses are varied between roughly half of the $\chi_1^{\pm}$ mass and $M(\chi_1^{\pm})$. These mass combinations allow for an efficiency determination in the large part of the SUSY parameter space considered in this analysis. This is illustrated in Fig. 6.11 where the efficiencies for the 'wrong' charge channel (left) and the 'right' charge channel (right) are shown in the $(M(\chi_1^{\pm}), M(\chi_1^0))$-plane for an example squark mass of 225 GeV. Although kinematically allowed, the region of high $\chi_1^{\pm}$ mass and low $\chi_1^0$ mass is not covered and the efficiencies are set to zero. In the SUSY parameter space this analysis is dealing with, these mass configurations are not possible for the $\chi_1^{\pm}$ and $\chi_1^0$, which represent the by far most important combination of gauginos in cascade

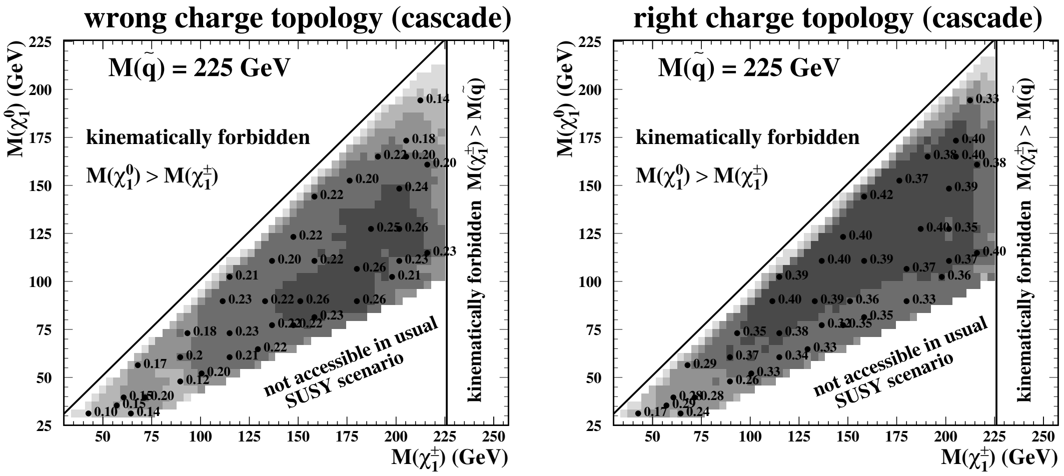


Figure 6.11: Selection efficiencies in cascade decays leading to the 'wrong' (left) and 'right' (right) charge topologies ($\tilde{q} \rightarrow q\chi_1^{\pm} \rightarrow q\,q\bar{q}\chi_1^0 \rightarrow q\,q\bar{q}\,e^{\pm}\bar{q}q$). Shown are the efficiencies for an example squark mass of 225 GeV.

decay chains.

For a particular squark mass of 225 GeV the efficiency in the cascade decay leading to the 'wrong' charge topology ranges between 15 % and 25 %. A similar behaviour of the efficiency has been observed for the other squark masses as well. Two squark mass dependent effects are important which nearly cancel. For high masses, electrons from the decay have more energy and are easier to detect. On the other hand they are emitted in the forward direction, where no charge information is available. For lower masses it is the other way round: the electrons have less energy, but are more central.

For the 'right' charge channel (right panel of Fig. 6.11) the dependence of the efficiency on $M(\tilde{q})$ and $M(\chi_1^{\pm})$ is rather small, but increases with higher $M(\chi_1^0)$ and ranges from 20 % to 45 %. High $\chi_1^0$ masses lead to electrons and jets of high energy and hence to higher selection efficiencies.

The systematic uncertainties on the selection efficiencies taken into account are identical to those discussed in Sec. 5.1.3.

## 6.3 Channels with additional charged leptons

As can be seen in Tab. 2.6, squarks decaying in cascade gauge decay modes (two intermediate gauginos) can lead to final state topologies containing charged leptons in addition to the electron/positron and multiple jets. For these multi-lepton final states the SM background is expected to be low. In this analysis we search for additional electrons/positrons and muons. Tau leptons are not explicitly searched for. The selection for the topologies $eeMJ$ and $e\mu MJ$ is based on the preselection presented in Sec. 6.1.3 where several control distributions demonstrate that the data are well understood. In addition, further cuts concerning the additional leptons are applied. It has been demonstrated in Sec. 4.5.1 and Sec. 4.5.2 that the identification of both electrons and muons is reliable.

| | $e^+p$ collisions | | $e^-p$ collisions | |
|---|---|---|---|---|
| final state | data | SM prediction | data | SM prediction |
| $eeMJ$ | 0 | $0.91 \pm 0.51$ | 0 | $0.13 \pm 0.03$ |
| $e\mu MJ$ | 0 | $0.91 \pm 0.38$ | 0 | $0.20 \pm 0.04$ |

TABLE 6.1: Numbers of observed and expected events in the $eeMJ$ and $e\mu MJ$ channel.

For some decay modes, which lead to the $elMJ$ topologies, neutrinos are involved in the final state. In particular the dominating cascade gauge decay of squarks to $\chi_1^\pm$ and its subsequent decay to $\chi_1^0$, contain a neutrino together with charged leptons ($\tilde{q} \to q\chi_1^\pm \to q\,\nu_l l\chi_1^0 \to q\,\nu_l l\, e\bar{q}q$). For this reason no restrictions on momentum balanced events can be imposed.

### 6.3.1 Selection for $eeMJ$ and $e\mu MJ$ topologies

The further selection steps for the two final state topologies with an additional charged lepton ($eeMJ$ and $e\mu MJ$) are very similar. For the latter we ask for an additional muon candidate following the identification criteria mentioned in Sec. 4.5.2 in the polar angular range $10° < \theta_\mu < 110°$. The transverse momentum of the muons must exceed 5 GeV. For the former we require that an additional electron/positron with the quality criteria described in the loose selection (Sec. 6.1.1) must be found in the polar angular range $5° < \theta_e < 110°$. Further cuts with little impact are applied to ensure an exclusive selection[5].

The numbers of events found in the data and which are expected from SM background processes are indeed very low. They are summarised in Tab. 6.1 for both topologies. In both data samples ($e^+p$ and $e^-p$) the data show no significant deviation from the SM expectation for $eeMJ$ and $e\mu MJ$. Thus, again there is no hint for squark production. NC DIS is the main background source for both topologies. The systematic uncertainties that we attribute to the SM background prediction are discussed in Sec. 4.7. The limited statistics of SM background MC is the dominant systematic error source.

### 6.3.2 Selection efficiencies for $eeMJ$ and $e\mu MJ$ topologies

For the topologies with an electron, at least two jets and an additional charged lepton, the background expectation from the SM is very small. For this reason no further mass restriction is applied. The sliding mass window method is not used in these cases, but the total number of events enters the limit calculation in Chap. 8.

There are three cascade gauge decay modes which could lead to a ***eeMJ* final state topology**. They are listed in the row "$eeMJ$" in Tab. 2.6. The first line represents the process with the highest BR since it can involve the $\chi_1^\pm$ and the $\chi_1^0$: $\tilde{q} \to q\chi_1^\pm \to q\,e\nu_e\chi_1^0 \to q\,e\nu_e\,e\bar{q}q$. A large variety of event samples with different mass combinations have been used to parameterise the efficiencies as a function of the masses. The results

[5]Events with a muon with $p_{T,\mu} > 5$ GeV and $10° < \theta_\mu < 110°$ are not accepted in $eeMJ$. Accordingly, events with an additional electron in the range $5° < \theta_e < 110°$ fulfilling the quality criteria described in the loose selection (Sec. 6.1.1) are not accepted in $e\mu MJ$.

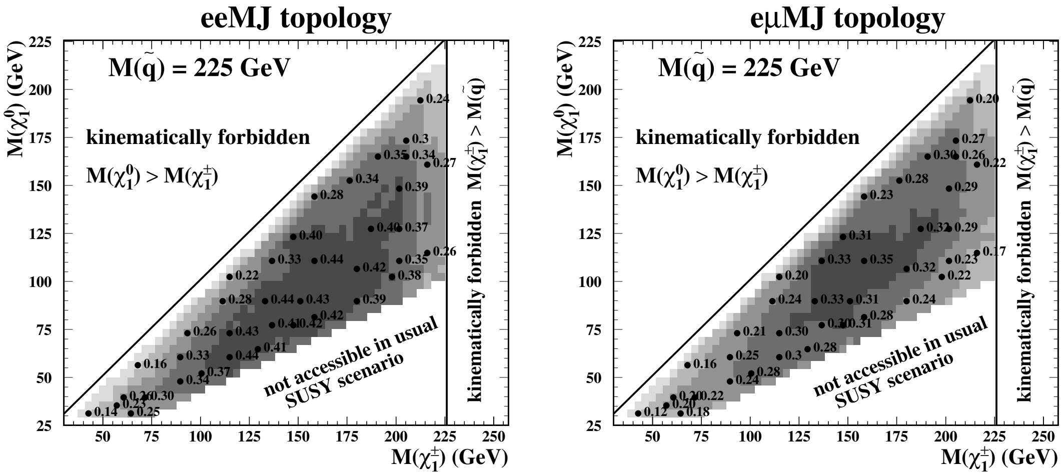


Figure 6.12: Selection efficiencies for final states with an additional charged lepton. Shown are the efficiencies for the $eeMJ$ topology (left) and the $e\mu MJ$ topology (right) for an example squark mass of 225 GeV which have been determined from the decay processes $\tilde{q} \to q\chi_1^{\pm} \to q\,\nu_e e\chi_1^0 \to q\,\nu_e e\,e\bar{q}q$ and $\tilde{q} \to q\chi_1^{\pm} \to q\,\nu_\mu \mu\chi_1^0 \to q\,\nu_\mu \mu\,e\bar{q}q$, respectively. Other decays chains leading to $eeMJ$ and $e\mu MJ$ with smaller branching ratios have been treated separately in the same manner.

are shown in Fig. 6.12 (left) for an example squark mass of 225 GeV. The selection of the $eeMJ$ topology leads to efficiencies rather constant with $M(\tilde{q})$. They range between 20 % and 50 % for all squark masses. The efficiency degrades at small mass differences $M(\chi_1^{\pm}) - M(\chi_1^0)$ and $M(\tilde{q}) - M(\chi_1^{\pm})$ since in these regions the electron or one quark have small energy.

The second decay chain leading to an $eeMJ$ topology is given in the second line in Tab. 2.6: $\tilde{q} \to qX \to q\,e^+e^-Y \to q\,e^+e^-\,e\bar{q}q$. This process usually has a small BR since it can only proceed via either two charginos or two neutralinos. The important $(\chi_1^{\pm}, \chi_1^0)$ combination is not possible due to charge conservation. Instead of the neutrino, a third electron occurs in the final state. Since in the selection no restriction of balanced or unbalanced events is imposed, the third electron leads to a higher selection efficiency of this decay chain compared to the one discussed before. Thus it is conservative to simply reuse the efficiency of the first decay chain with one neutrino and two electrons in the final state. It has been tested at a high number of example parameter space points that this simplification is indeed conservative.

The third decay chain leading to the $eeMJ$ topology $\tilde{q} \to qX \to q\,e^+e^-Y \to q\,e^+e^-\,\nu\bar{q}q$ has small BR as well, since again this decay cannot proceed via the important gaugino combination of $\chi_1^{\pm}$ and $\chi_1^0$, but e.g. via two neutralinos. Although in this case the particles in the final state are identical to those of the first decay chain leading to $eeMJ$ the kinematics are different. For this reason we explicitly determine the selection efficiency of the decay mode by simulating the decay involving $\chi_2^0$ and $\chi_1^0$ for various mass combinations of the three supersymmetric particles involved. The selection efficiency shows a similar behaviour as the first decay chain leading to $eeMJ$ and ranges between 20 % and 50 %.

As can be seen in Tab. 2.6 only two decay chains must be considered for the $\boldsymbol{e\mu MJ}$

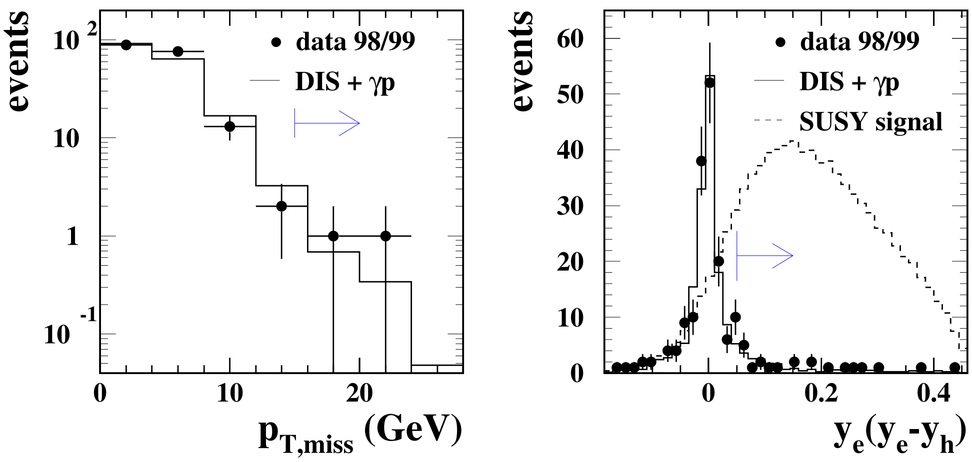


Figure 6.13: Distributions after the loose selection (Sec. 6.1.1) for the 1998/1999 data set. Shown are the total transverse momentum $p_{T,\rm miss}$ (left) and the combined variable $y_e(y_e - y_h)$ (right). The selection cuts for the $\nu eMJ$ topology are indicated by arrows. Distributions for 1999/2000 are very similar.

**final state topology**, leading to either one or two muons in the final state. The first one represents the important decay of a chargino to a neutralino. This decay chain is considered by simulating the process $\tilde{q} \to q\chi_1^{\pm} \to q\,\mu\nu_\mu\chi_1^0 \to q\,\mu\nu_\mu\, e\bar{q}q$ in a dense mass grid. The resulting efficiencies are illustrated in the right panel of Fig. 6.12 for an example squark mass of 225 GeV. It ranges from 15 % to 40 % and shows a similar behaviour to the dominant $eeMJ$ channel. The dependence on the squark mass is found to be low.

For the second decay chain leading to $e\mu MJ$ a simplification can be made which is similar to the approach for the $eeMJ$ topology. The efficiency of the dominating decay channel with one muon in the final state can be reused for the second decay chain $\tilde{q} \to qX \to q\,\mu^+\mu^- Y \to q\,\mu^+\mu^-\, e\bar{q}q$ since for this decay mode two muons occur in the final state. Thus the selection efficiency must be higher and the simplification gives a conservative estimate. This has been checked at various example mass configurations. The BRs for decay modes leading to two muons in the final state are low since they cannot proceed via a chargino–neutralino decay chain.

## 6.4 Channels with an additional neutrino

Cascade gauge decays of squarks could lead to final state topologies with multiple jets, an electron and an additional neutrino ($\nu eMJ$). Events of this topology are selected with the common preselection described in Sec. 6.1.3. In order to enhance the ratio of selected signal to SM background further selection cuts are applied:

- The total transverse momentum of the event must exceed 15 GeV since the neutrino escapes undetected. The $p_{T,\rm miss}$ distributions for the 1998/1999 data taking period after the loose selection of Sec. 6.1.1 are shown in Fig. 6.13 (left). The cut, indicated

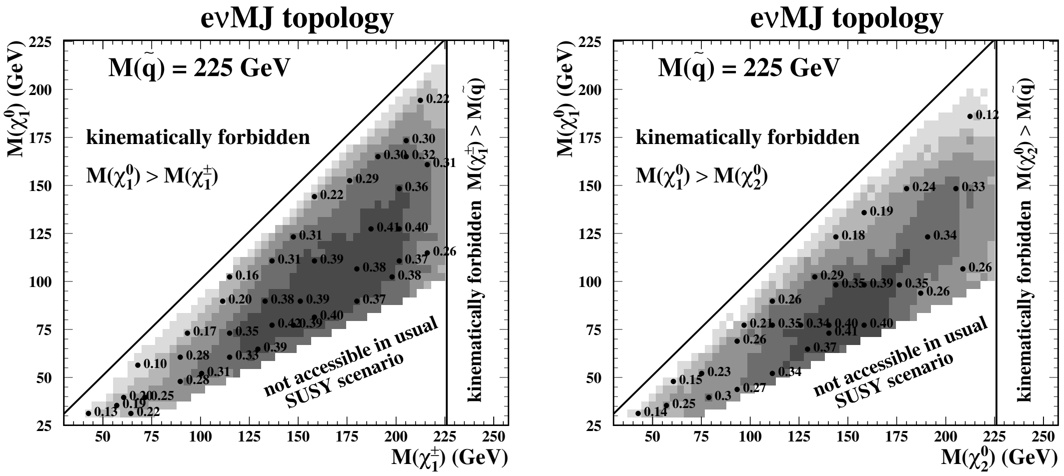


FIGURE 6.14: Efficiencies for the $\nu eMJ$ topology for a squark with a mass of 225 GeV. Shown are the results from the two decay processes leading to this topology: $\tilde{q} \to q\chi_1^\pm \to q\,\nu_e e\chi_1^0 \to q\,\nu_e e\,\nu\bar{q}q$ (left) and $\tilde{q} \to q\chi_2^0 \to q\,\nu\nu\chi_1^0 \to q\,\nu\bar{\nu}\,e\bar{q}q$ (right).

by an arrow, drastically reduces the amount of background.

- A cut on $y_e(y_e - y_h) > 0.04$ exploits the fact that, for events coming from a squark decaying into the $\nu eMJ$ channel, the escaping neutrino carries a non-negligible part of $\sum(E - p_z)$ and hence the variable $y_h$ is substantially smaller than $y_e$, while $y_e \sim y_h$ is expected for NC DIS events. The effect of this cut is illustrated in Fig. 6.13 (right), where the $y_e(y_e - y_h)$ distributions are shown for 1998/1999 data, SM background and for the signal from squarks decaying to $\nu eMJ$ final states after the loose selection of Sec. 6.1.1. The signal is normalised in arbitrary units. The cut indicated by an arrow clearly separates the SUSY signal from the SM background.

- To reach an exclusive selection with respect to the $eeMJ$ and $e\mu MJ$ selection channels, events with a second electron candidate with $p_{T,e} > 5$ GeV and $5° < \theta_e < 110°$ or a muon candidate with $p_{T,\mu} > 5$ GeV and $10° < \theta_\mu < 110°$ are rejected.

After this selection the standard model expectation is very low. No event is found in $e^+p$ collisions with $0.74 \pm 0.26$ predicted by the SM. In the $e^-p$ data set no event is selected and $0.21 \pm 0.07$ are expected from SM background processes. The main background source is NC DIS. The most relevant error on the SM expectation is the limited statistics of the SM MC.

### Signal efficiencies in the $\nu eMJ$ topology

For the $\nu eMJ$ topology two cascade decay chains could contribute. The first line of the row "$\nu eMJ$" in Tab. 2.6 represents the usually dominating one: $\tilde{q} \to q\chi_1^\pm \to q\,\nu_e e\chi_1^0 \to q\,\nu_e e\,\nu\bar{q}q$. This process is used to determine the efficiency of the selection as a function of the masses involved. The resulting efficiency is shown in Fig. 6.14 (left) for an example squark mass of 225 GeV. The behaviour of this efficiency is found to be similar for all squark masses. It degrades for small mass differences $M(\chi_1^\pm) - M(\chi_1^0)$ since the electron gets little energy in the decay of the $\chi_1^\pm$. For higher mass differences the missing transverse momentum is additionally increased by the second neutrino, which is present in the final state, resulting in a higher selection efficiency.

The second decay chain leading to the $\nu eMJ$ topology is represented by the second line in Tab. 2.6. These processes are usually suppressed. Nevertheless we determine the selection efficiencies as a function of the three masses involved. The results are shown in the right panel of Fig. 6.14 for an example squark mass of 225 GeV derived from the decay chain $\tilde{q} \to q\chi_2^0 \to q\,\nu\nu\chi_1^0 \to q\,\nu\bar{\nu}\,e\bar{q}q$. For this decay mode the dependence on the squark mass is again found to be low. The efficiency ranges between 15 % and 45 %. For high mass differences $M(\chi_1^\pm) - M(\chi_1^0)$, the two neutrinos lead to a significant $p_{T,\mathrm{miss}}$ since they carry high energy, and the selection efficiency is increased.

# Chapter 7

# Channels with Neutrino and Multiple Jets

In gauge decays of squarks via one or two gauginos (charginos, neutralinos or gluinos) the final state can consist of a neutrino and multiple jets. In particular, in cases where the lightest neutralino $\chi_1^0$ is zino-like, these final states contribute significantly since the $\chi_1^0$ predominantly decays into $\nu + \bar{q}q$. If the squark decay proceeds through a cascade gauge decay muons can be produced in addition. In this chapter the selection criteria for the final state topologies $\nu MJ$ and $\nu\mu MJ$ are presented and the corresponding signal efficiencies are derived. For both channels a common preselection has been carried out.

## 7.1 Common preselection

The following preselection is used for both final state topologies $\nu MJ$ and $\nu\mu MJ$:

- The **missing transverse momentum** of the events must exceed 26 GeV. In the decay chains of squarks considered here at least one neutrino is produced which escapes undetected. This neutrino carries transverse momentum, which is not measured. This harsh cut on $p_{T,\mathrm{miss}}$ reduces the amount of photoproduction background in the selection and ensures a high efficiency of the trigger[1] whose performance is discussed in more detail in Sec. 5.2.1. In the kinematic region considered here the efficiency of the CC trigger exceeds 90 % [54]. The corresponding small inefficiency has been corrected for as outlined in Sec. 5.2.1.
- **No electron candidate** with $p_{T,e} > 5$ GeV must be found in the events.
- The events must contain **at least two jets** with $p_{T,\mathrm{jet}} > 15$ GeV found in the angular range $7° < \theta < 145°$. The latter restriction ensures that the jets are well measured in the LAr. If the jet with the second highest $p_T$ is found in the vicinity of the most central calorimeter $z$-crack (CB2/CB3) the number of clusters in the jet must exceed four. This cut reduces the contamination of NC DIS events where the electron is scattered through the crack and is misidentified as a hadronic jet. The signal efficiency loss of this cut is negligible.

[1]ST66, ST67, ST71 and ST77

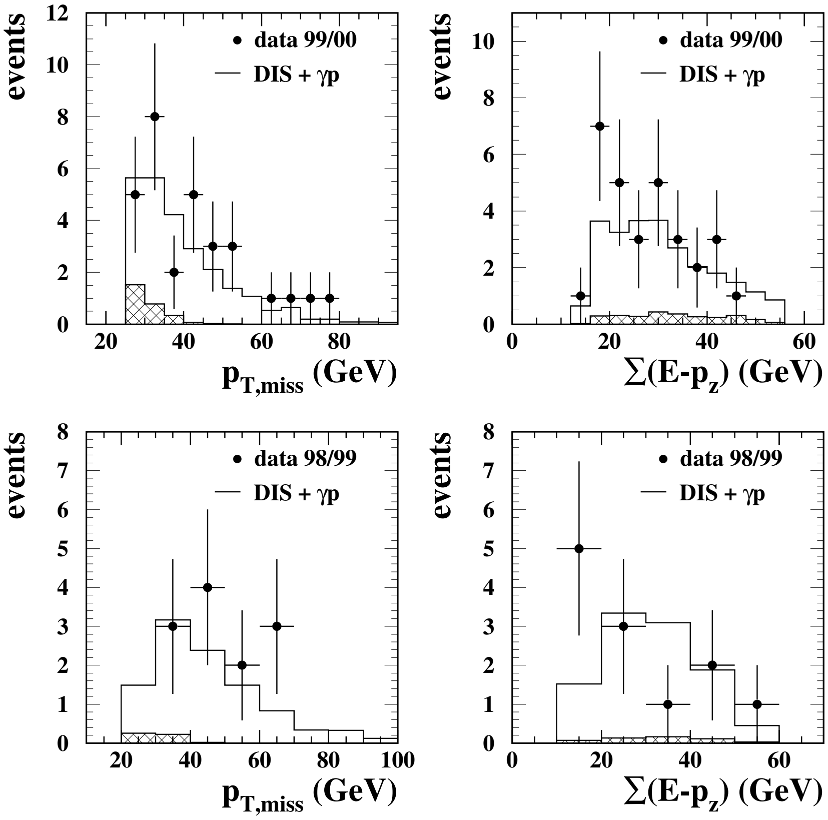


FIGURE 7.1: Control distributions after the $\nu MJ$ preselection in 1999/2000 (top) and 1998/1999 (bottom). Shown are the missing transverse momentum $p_{T,\mathrm{miss}}$ (left) and the momentum balance with respect to the direction of the incident electron $\sum(E-p_z)$ (right). The SM background includes NC DIS, CC DIS and photoproduction (hatched histograms).

After this preselection the event statistics are already very limited. In Fig. 7.1 two example distributions are shown for the 1999/2000 data taking period (top) and the 1998/1999 data taking period (bottom). The variables, $p_{T,\mathrm{miss}}$ (left) and $\sum(E-p_z)$ (right), concerning total event properties, are well described by the SM background Monte Carlo within errors. In Fig. 7.2 example distributions of variables related to the jets are shown for events with exactly two jets from both data samples: $e^+p$ (top, 1999/2000) and $e^-p$ (bottom, 1998/1999). Shown are the polar angle of the jet with highest $p_T$ and the invariant mass of the two jets $M_{12}$. The data are described by the SM prediction within errors.

The main source of SM background is CC DIS as determined by a simulation using the DJANGO generator with CTEQ5L structure functions. A remaining contribution of $\sim 7\,\%$ coming from NC DIS is still in the MC selection. The amount of photoproduction background is $\sim 10\,\%$ and is indicated in the figures by the hatched histograms. In addition a contribution of $1\,\%$ coming from the production of the heavy gauge bosons $Z^0$ and $W^\pm$ has been observed in the MC.

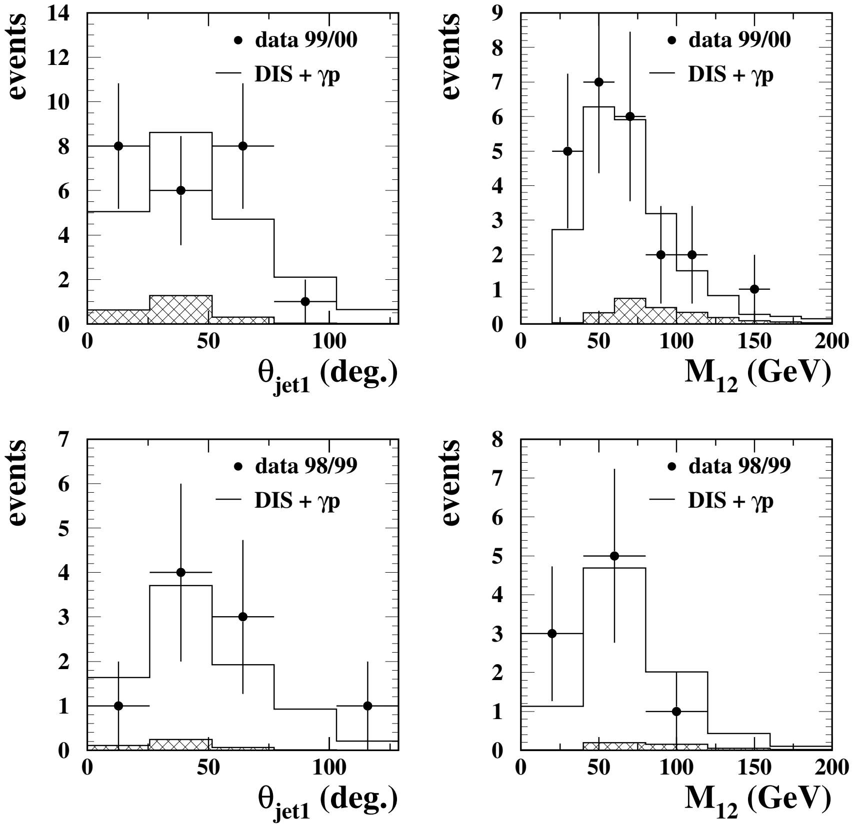


FIGURE 7.2: Example distributions after the $\nu MJ$ preselection: Polar angle $\theta_{\text{jet1}}$ of the jet with highest $p_T$ (left) in events with exactly 2 jets and the invariant mass $M_{12}$ of these jets (right) for 1999/2000 (top) and 1998/1999 (bottom). The hatched histograms indicate the contributions from photoproduction.

## 7.2 Channel $\nu MJ$

### 7.2.1 Event selection

In principle the selection for the $\nu MJ$ final state topology is finished after the preselection. In order to guarantee the exclusivity of the selection for the limit calculation a further cut must be applied having little impact on the selection:

- It is required that no muon candidate is found in the event. This cut assures that no event is counted in both channels $\nu MJ$ and $\nu\mu MJ$.

#### Invariant mass distributions

For events fulfilling the $\nu MJ$ selection criteria an invariant mass $M_{\text{inv}}$ can be calculated from $p_T$ and $E - p_z$ conservation assuming that only one neutrino is present in the event. For this method the four-momentum of the neutrino $p_\nu = (p_{x\nu}, p_{y\nu}, p_{z\nu}, E_\nu)$ must be

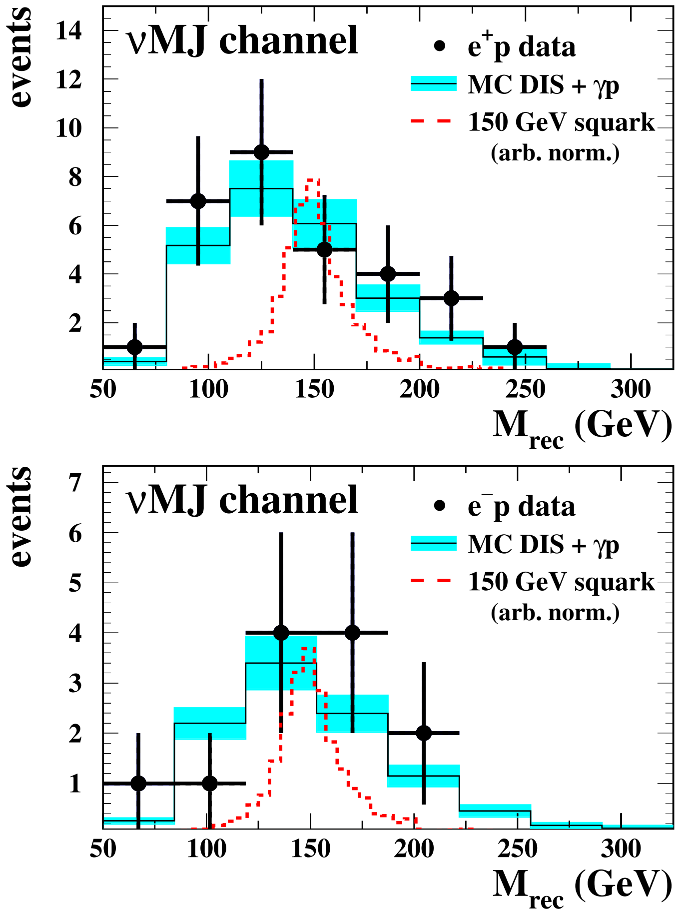


Figure 7.3: Invariant mass distributions in the $\nu MJ$ selection channel for $e^+p$ collisions (top) and $e^-p$ collisions (bottom). The hypothetical signal from a squark of 150 GeV is indicated by the dashed histogram in arbitrary normalisation.

calculated from the total four-momentum of the event $p_{\mathrm{tot}} = (p_{x\mathrm{tot}}, p_{y\mathrm{tot}}, p_{z\mathrm{tot}}, E_{\mathrm{tot}})$. Momentum conservation leads to

$$p_{T,\nu} = -p_{T,\mathrm{tot}} \qquad \text{and} \qquad (E - p_z)_\nu = 2E_e^0 - (E - p_z)_{\mathrm{tot}} \quad . \tag{7.1}$$

Neutrinos are assumed to be massless. This gives

$$E_\nu = \frac{p_{T,\nu}^2 + (E - p_z)_\nu^2}{2(E - p_z)_\nu} \quad . \tag{7.2}$$

The $z$ component of the muon momentum $p_{z,\nu}$ can be computed by combining Eq. 7.1 (right) and Eq. 7.2. Then the invariant mass $M_{\mathrm{inv}}$ can be calculated using Eq. 7.1 (left).

$$M_{\mathrm{inv}} = \sqrt{(E_{\mathrm{tot}} + E_\nu)^2 - (p_{z,\mathrm{tot}} + p_{z,\nu})^2} \quad . \tag{7.3}$$

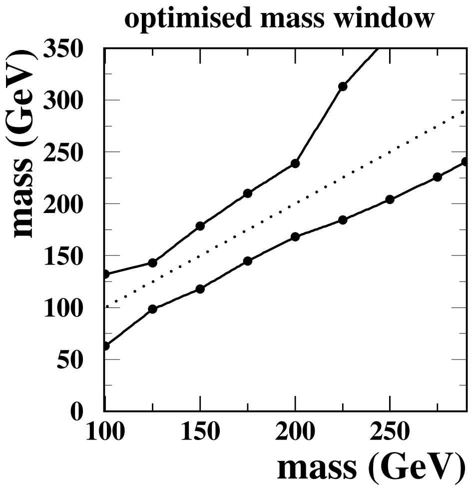


FIGURE 7.4: Optimal mass window for the $\nu MJ$ topology derived for a final state including one neutrino only.

This reconstruction method gives a good estimator of the squark mass, if indeed one neutrino is in the final state[2]. The mass resolution is found to vary between 12 GeV and 20 GeV depending on the squark mass.

In Fig. 7.3 the mass spectra of data and expected SM background are shown for $e^+p$ (top) and $e^-p$ (bottom) collisions. Both data samples are described by the SM prediction. 30 events are selected in the $e^+p$ data set while 24.3±3.6 are expected from SM background processes. For $e^-p$ collisions 12 events are selected in the data with $10.1 \pm 1.4$ predicted from the SM. Hence there is no hint of squarks. Systematic uncertainties on the SM background expectation are considered according to Sec. 4.7. The theoretical uncertainty on the SM cross section of multijet final states is found to be most important. In Fig. 7.3 the signal of a squark with a mass of 150 GeV decaying into final states with one neutrino and several jets is also given by the dashed histogram which demonstrates that the mass reconstruction method gives reasonable results.

### 7.2.2 Selection efficiencies

For the $\nu MJ$ topology again the sliding mass window method (Sec. 5.1.2) is used to reduce the SM background and enhance the SUSY signal for a given squark mass. The optimal mass window derived from the $M_{\text{inv}}$ distributions of the SM background in 1999/2000 and a SUSY signal channel with one neutrino in the final state is shown in Fig. 7.4. The width of the mass window increases due to the resolution degradation at high masses. Again the upper mass cut tends to high values since it is better to include the full squark mass peak of the signal and accept a limited additional background contribution from higher masses. The lower mass cut remains restrictive to exclude background from lower masses.

According to Tab. 2.6 three different gauge decay chains of squarks can lead to the

[2]In final states with more than one neutrino the masses are underestimated by 5 % to 15 %.

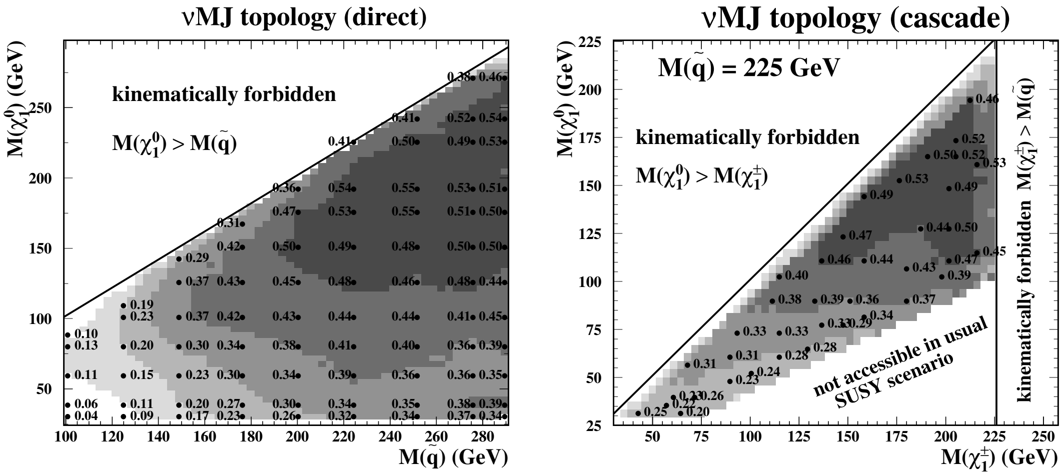


FIGURE 7.5: Signal efficiencies for the $\nu MJ$ topology. Shown are the results in the direct (left) and cascade decay modes (right) determined from the decay chain $\tilde{q} \to q\chi_1^0 \to q\,\nu\bar{q}q$ and $\tilde{q} \to q\chi_1^{\pm} \to q\,q\bar{q}\chi_1^0 \to q\,q\bar{q}\,\nu\bar{q}q$, respectively. The decay process $\tilde{q} \to q\chi_2^0 \to q\,\nu\bar{\nu}\chi_1^0 \to q\,\nu\bar{\nu}\,\nu\bar{q}q$ is treated in the same manner.

$\nu MJ$ topology. For the **direct gauge decay** (first line of the row "$\nu MJ$" in Tab. 2.6) the decay chain $\tilde{q} \to q\chi_1^0 \to q\,\nu\bar{q}q$ with varying squark and neutralino masses is used to parameterise the selection efficiencies. The results are shown in the left panel of Fig. 7.5. At low masses (squark and gaugino) the $p_{T,\mathrm{miss}}$ cut is often not fulfilled and the selection efficiency is rather low, around 10 %. For high masses the efficiency increases up to 55 %.

**Cascade decay chains** can also lead to the $\nu MJ$ final state with only one neutrino (second line of the row "$\nu MJ$" in Tab. 2.6). The process with the highest BR $\tilde{q} \to q\,\chi_1^{\pm} \to q\,q\bar{q}\chi_1^0 \to q\,q\bar{q}\,\nu\bar{q}q$ has been used to determine the efficiency. The results are shown in Fig. 7.5 (right) for an example squark mass of 225 GeV. In this decay mode the efficiency is found to be essentially independent of the squark mass and the mass of the first gaugino in the decay chain, but it strongly depends on the mass of the second gaugino ($\chi_1^0$) in the decay: for high $\chi_1^0$ masses the neutrino from the neutralino decay is highly energetic and the harsh $p_{T,\mathrm{miss}}$ requirement can be fulfilled.

The $\nu MJ$ topology can also be reached by a cascade gauge decay chain involving either two charginos or two neutralinos (third line of the row "$\nu MJ$" in Tab. 2.6). Then the final state consists of three neutrinos and the mass reconstruction method of Eq. 7.3 underestimates the generated mass. The efficiency of this decay chain is studied by simulating the process $\tilde{q} \to q\,\chi_2^0 \to q\,\nu\bar{\nu}\chi_1^0 \to q\,\nu\bar{\nu}\,\nu\bar{q}q$. The mass window cut in Fig. 7.4 leads to an efficiency loss since the window is optimized for channels with one neutrino only. The channels leading to more than one neutrino are of minor importance, as a "left" squark usually decays in a decay chain involving $\chi_1^{\pm}$ and $\chi_1^0$. For "right" squarks all cascade decay modes are suppressed anyway.

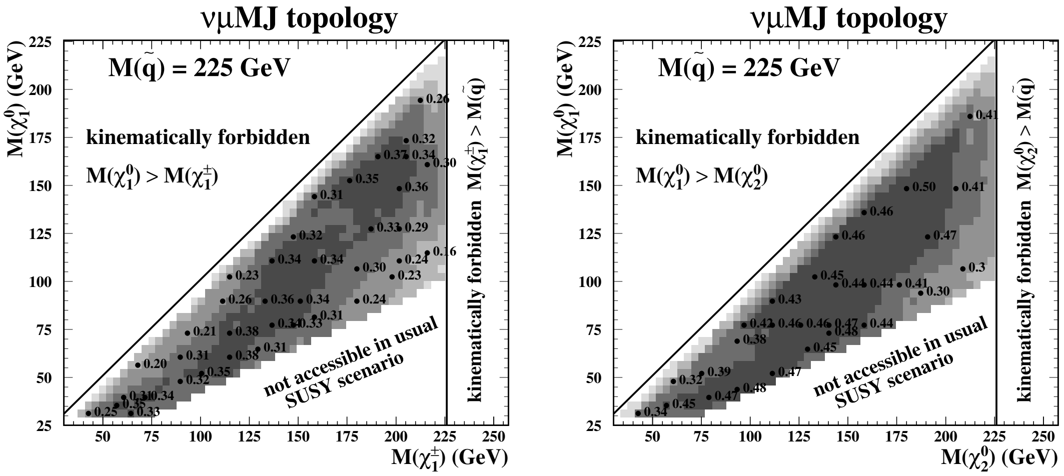


Figure 7.6: Signal efficiencies for $\nu\mu MJ$ final states. Shown are the results from the two decay chains leading to this topology for a squark mass of 225 GeV: $\tilde{q} \to q\chi_1^\pm \to q\,\nu_\mu\mu\chi_1^0 \to q\,\nu_\mu\mu\,\nu\bar{q}q$ (left) and $\tilde{q} \to q\chi_2^0 \to q\,\mu^+\mu^-\chi_1^0 \to q\,\mu^+\mu^-\,\nu\bar{q}q$ (right).

## 7.3 Channel with an additional muon

An additional muon can occur in the final state of cascade gauge decays of squarks. If the lightest neutralino is predominantly zino-like these decays can lead to the $\nu\mu MJ$ topology. In the decay of "right" squarks ($e^-p$) these decays are suppressed.

### 7.3.1 Event selection

In addition to the preselection presented in Sec. 7.1 for the $\nu\mu MJ$ topology it is required that:

- A muon candidate with $p_{T,\mu} > 5$ GeV must be found in the event. The polar angle of the muon candidate must satisfy $10^\circ < \theta_\mu < 110^\circ$. The identification of muons is reliable as demonstrated in Sec. 4.5.2.

With this selection, no event is selected in both 1999/2000 and 1998/1999 data. The prediction from the SM is $0.61 \pm 0.12$ and $0.16 \pm 0.03$ respectively. In this selection channel the uncertainties arising from the limited SM MC statistics, the hadronic energy scale and the theoretical uncertainty on multijet final states are important.

### 7.3.2 Signal efficiencies for $\nu\mu MJ$ final states

As can be seen in Tab. 2.6 there are two cascade gauge decay chains leading to the $\nu\mu MJ$ topology. For most parameter configurations the decay chain: $\tilde{q} \to q\chi_1^\pm \to q\,\nu_\mu\mu\chi_1^0 \to q\,\nu_\mu\mu\,\nu\bar{q}q$ is most important. For an example squark mass of 225 GeV the determined selection efficiencies of this decay chain are shown in Fig. 7.6 (left). Values between 20 % and 40 % have been determined for various gaugino mass combinations. The efficiencies are found to be rather independent of the squark mass.

The decay chains leading to two muons in the final state (third line of the row "$\nu MJ$" in Tab. 2.6) have usually lower BRs since they proceed either via two charginos or two neutralinos, e.g. $\tilde{q} \rightarrow q\chi_2^0 \rightarrow q\,\mu^+\mu^-\chi_1^0 \rightarrow q\,\mu^+\mu^-\,\nu\bar{q}q$. The mass dependent efficiencies are shown in Fig. 7.6 (right), again for an example squark mass of 225 GeV. The signal efficiency of this decay chain is found to be only weakly dependent on the gaugino masses and ranges between 30 % and 50 % for this squark mass. The corresponding efficiency is higher than in the decay leading to $\nu\mu MJ$ with only one muon shown in the left panel of Fig. 7.6 since if two muons are in the final state the probability of identifying at least one is greater.

# Chapter 8

# Interpretation

The investigation of the experimental squark signatures considered in the present analysis reveals no deviation from the SM for both data samples, $e^+p$ and $e^-p$ collisions. Thus, no hint for squark production is found in the data. Therefore the results of the selection are used to set exclusion limits on the parameters of various supersymmetric models.

In the first section of this chapter a summary of the selection is given. The following section describes a procedure which is applied to further improve the sensitivity to $\not{R}_p$ squark production: in the limit derivation the *cross talk* between decay and selection channels is taken into account. At high masses the squark can have a non-negligible intrinsic width. These cases must be carefully dealt since the ordinary Narrow Width Approximation (NWA) would give too optimistic exclusion limits. Taking this into account a new approach has been developed to properly calculate exclusion limits at high squark masses. The corresponding procedure is described in Sec 8.3. Finally the mathematical calculation method of the exclusion limits is presented and the results in the phenomenological MSSM with $\not{R}_p$ and the minimal Supergravity model (mSUGRA) with $\not{R}_p$ are discussed. The limits are compared to previous results from HERA and other experiments.

## 8.1 Selection summary

In the separate investigation of eight squark decay topologies in $64.3\,\mathrm{pb}^{-1}$ of $e^+p$ collision data and nine decay topologies in $13.5\,\mathrm{pb}^{-1}$ of $e^-p$ collision data no deviation from the SM prediction has been found. All decay channels resulting from $\not{R}_p$ and $R_p$ conserving decay modes are in agreement with the SM expectation. In Tab. 8.1 the total numbers of events selected in the data and the numbers expected from SM processes are summarised.

In both lepton–quark channels, $eq$ and $\nu q$, the data are described by the SM prediction. This is also true for the gauge decays, where the SM expectation is considerable – the channel $eMJ$ with 'right' charge and the $\nu MJ$ channel. In these channels the differential comparison of mass spectra in data and SM MC gives no indication for the resonant production of squarks. Even the very striking topologies with multiple leptons or with a 'wrong' charge electron/positron which are almost free of SM background are in agreement with the expectation. The selection of the decay channels is carried out in such a way, that it leads to a fully exclusive selection, i.e. any given event (data, background or signal) can contribute to one selection channel only.

| final state | $e^+p$ collisions data | SM prediction | $e^-p$ collisions data | SM prediction |
|---|---|---|---|---|
| $eq$ | 632 | $628.0 \pm 45.7$ | 204 | $191.6 \pm 14.0$ |
| $\nu q$ | — | — | 261 | $268.5 \pm 20.8$ |
| $e^-MJ$ | 0 | $0.20 \pm 0.14$ | 20 | $17.9 \pm 2.4$ |
| $e^+MJ$ | 72 | $67.5 \pm 9.5$ | 0 | $0.06 \pm 0.02$ |
| $eeMJ$ | 0 | $0.91 \pm 0.51$ | 0 | $0.13 \pm 0.03$ |
| $e\mu MJ$ | 0 | $0.91 \pm 0.38$ | 0 | $0.20 \pm 0.04$ |
| $\nu eMJ$ | 0 | $0.74 \pm 0.26$ | 0 | $0.21 \pm 0.07$ |
| $\nu MJ$ | 30 | $24.3 \pm 3.6$ | 12 | $10.1 \pm 1.4$ |
| $\nu\mu MJ$ | 0 | $0.61 \pm 0.12$ | 0 | $0.16 \pm 0.03$ |

Table 8.1: Total numbers of selected events for the squark decay channels considered in $e^+p$ (left) and in $e^-p$ collisions (right).

## 8.2 Cross talk between decay and selection channels

The selection efficiencies described in the previous chapters consider the selection of signal events from a certain decay mode only in the corresponding selection topology according to Tab. 2.6. For example in the determination of the selection efficiency of the decay mode $\tilde{q} \to q\chi_1^\pm \to q\,\nu_\mu\mu\chi_1^0 \to q\,\nu_\mu\mu\,\nu\bar{q}q$ only the $\nu\mu MJ$ selection is investigated. However, signal events from this decay mode could be selected in a different decay channel. If for instance the muon is not found, the events are not selected in $\nu\mu MJ$. Nevertheless these events have such a spectacular signature that they are unlikely to be missed since the criteria of a different selection channel, e.g. $\nu MJ$, can be fulfilled.

Thus there is an additional sensitivity to the decay chain $\tilde{q} \to q\chi_1^\pm \to q\,\nu_\mu\mu\chi_1^0 \to q\,\nu_\mu\mu\,\nu\bar{q}q$ in the $\nu MJ$ selection. The corresponding efficiencies are shown in the left panel of Fig. 8.1 for an example squark mass of 225 GeV in a dense grid of $\chi_1^\pm$ and $\chi_1^0$ masses. It reaches values up to about 30 % for cases where the $\chi_1^\pm$ and $\chi_1^0$ have similar masses. In these cases the muons get little energy in the $\chi_1^\pm$ decay and events are often not selected in $\nu\mu MJ$ but in $\nu MJ$. Thus the selection efficiency in $\nu MJ$ is higher for these mass configurations.

By including this *cross talk* between several decay channel and selection channels the sensitivity for squark production can be increased. For all combinations of decay and selection channels the amount of cross talk has been checked. For the most important combinations the additional efficiency is taken into account in the limit calculation. As a further example, the efficiency of the $\nu eMJ$ selection for the decay chain $\tilde{q} \to q\chi_1^\pm \to q\,e\nu_e\chi_1^0 \to q\,e\nu_e\,e\bar{q}q$ and a squark mass of 225 GeV is shown in Fig 8.1 (right). In Tab. 2.6 this decay chain is attributed to the $eeMJ$ selection channel. Events not fulfilling the $eeMJ$ selection criteria, but the $\nu eMJ$ selection lead to additional efficiencies up to 20 %.

For a given decay mode the combined efficiency taking into account all selection channels never exceeds 100 % since the selection is exclusive. With this method the limits on the Yukawa coupling $\lambda'$ (see Sec. 8.6) are improved by 5 to 20 % depending on the squark mass and the SUSY parameter set.

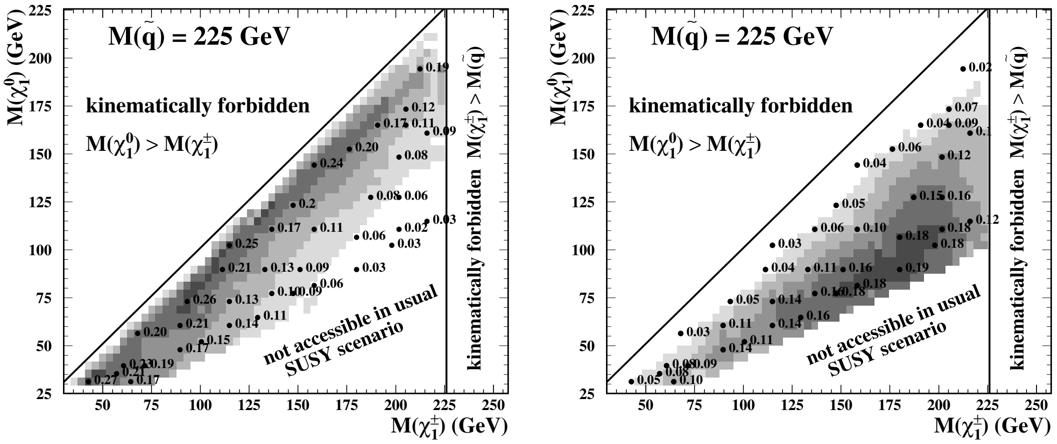


FIGURE 8.1: Cross talk between decay channel and selection channel. Shown are the efficiencies for events from the decay chain $\tilde{q} \to q\chi_1^\pm \to q\,\nu_\mu\mu\chi_1^0 \to q\,\nu_\mu\mu\,\nu\bar{q}q$ in the selection channel $\nu MJ$ for an example squark mass of 225 GeV(left). The right panel illustrates the efficiency for $\tilde{q} \to q\chi_1^\pm \to q\,e\nu_e\chi_1^0 \to q\,e\nu_e\,e\bar{q}q$ in the $\nu eMJ$ selection.

## 8.3 Corrections at very high squark masses

The kinematic border of resonant squark production at HERA is given by the centre of mass energy of $\sqrt{s} = 320$ GeV. Already at smaller masses squarks can have an intrinsic width $\Gamma_{\tilde{q}}$ of the order of 1 GeV reaching up to 5 GeV in some SUSY configurations. There are three reasons why squarks produced in $ep$ collisions become broad at high masses.

- Following from the HERA sensitivity to the Yukawa coupling $\lambda'$, shown for example in Fig. 2.14, only high values of $\lambda'$ can be tested at high squark masses. A large value of $\lambda'$ leads to a large partial decay width $\Gamma_{\not{R}_p}$ for the $\not{R}_p$ lepton–quark decays as can be seen from Eq. 2.49. Assuming a Yukawa coupling of 0.5 a hypothetical squark of 290 GeV mass has $\Gamma_{\not{R}_p} = 1.5$ GeV. At high masses these decay channels have the highest BRs. Thus the squark becomes broader.

- At high squark masses it is more likely that the neutralinos or charginos have smaller masses and the squark decay into them is kinematically allowed. Hence more decay channels are open.

- For squarks with high masses the kinematic phase space of the decay products is enlarged.

The resulting intrinsic squark width is still very small compared to the experimental mass resolution of all reconstruction methods used. Nevertheless, for squark masses $\gtrsim 270$ GeV a squark width of a few GeV can have interesting kinematic consequences for the production of squarks in $e^\pm p$ collisions resulting from the steeply falling parton densities of the proton. This is a result of the convolution of the squark Breit-Wigner curve with the proton PDF in the cross section formula. For a high squark width the long tail of the Breit-Wigner curve

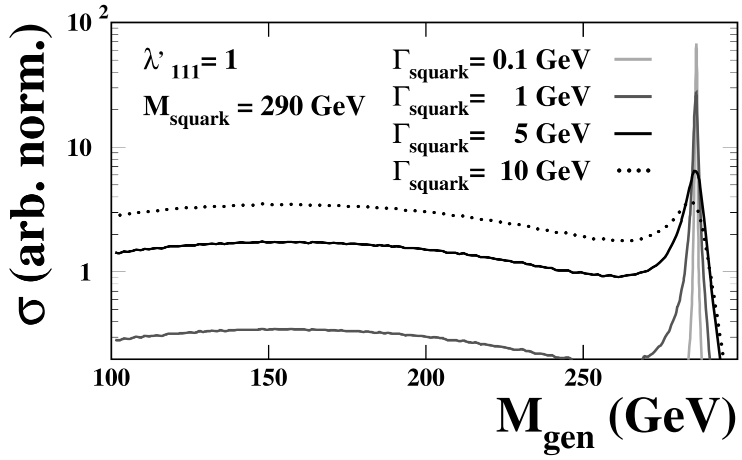


FIGURE 8.2: Squark production cross section for various squark widths.

towards lower squark masses 'sees' a high valence quark density since the latter strongly increases towards low masses (or low $x$, cf. Eq. 2.46) reaching a maximum around $x \approx 0.2$. The kinematic effects are illustrated in Fig. 8.2 where the cross section $\sigma$ for the $\not{R}_p$ $s$-channel production of a $\tilde{u}_L^j$ in $e^+p$ collisions and the directly $\not{R}_p$ squark decay into $e^+d$ is shown for various squark widths. The Feynman diagram corresponding to this process is shown in Fig. 2.15 (left). In Fig. 8.2 the results of the calculations using the CompHEP package [74] are shown as a function of the invariant mass $M_{\rm gen}$ of the two decay products $e^+ + d$ for a hypothetical squark with a mass of 290 GeV. For a small squark width of 0.1 GeV the cross section has a narrow peak around the nominal squark mass – the NWA is a good approximation in this case. However, for higher squark widths this peak decreases and a tail at low squark masses becomes more important. For a huge squark width of 10 GeV the resonance peak at high masses is suppressed and the main contribution to the total cross section of the $s$-channel squark production comes from lower masses[1]. Therefore special attention must be paid at high squark masses to the determination of production cross sections and selection efficiencies. The cross section calculation using the Narrow Width Approximation (NWA) of Eq. 2.47 and Eq. 2.48 must be corrected.

In the simulation of signal events the squark decay products are generated with invariant masses according to the cross section shown in Fig. 8.2. Thus the generated squark mass spectrum in $ep$ collisions is distorted in cases where the squark width is not negligible, leading to a dependence of the selection efficiency for a given selection channel on the squark width. The generation of signal events for various squarks widths $\Gamma_{\tilde{q}}$ can be avoided by determining the efficiency for a negligible width and afterwards correcting it. For a selection channel $i$ we calculate the corrected efficiency $\varepsilon_i(\Gamma_{\tilde{q}})$ by reducing the efficiency determined for a negligible squark width $\varepsilon_i(\Gamma_{\tilde{q}} = \text{negl.})$. The correction formula considers

[1] $\Gamma_{\tilde{q}}$ never reaches such high values in the supersymmetric parameter space dealt with in this analysis. The results for $\Gamma_{\tilde{q}} = 10\,\text{GeV}$ are shown for demonstration purposes.

the fraction of events generated at lower masses and the reduction of the resonance peak:

$$\varepsilon_i(\Gamma_{\tilde{q}}) = \frac{\int_{m_d^i}^{m_u^i} \sigma(M_{\text{gen}}, \Gamma_{\tilde{q}})\ dM_{\text{gen}}}{\int_0^{\sqrt{s}} \sigma(M_{\text{gen}}, \Gamma_{\tilde{q}} = \text{negl.})\ dM_{\text{gen}}} \cdot \varepsilon_i(\Gamma_{\tilde{q}} = \text{negl.}). \tag{8.1}$$

Here $m_d^i$ and $m_u^i$ denote the lower and upper values of a mass window around the nominal squark mass which is chosen individually for each selection channel: In channels for which the sliding mass window method is applied the optimal mass window is taken. For the other channels we use a mass window of $\pm 20\,\text{GeV}$ around the nominal squark mass.

With this method the analysis is restricted to the peak region where the efficiencies of all selection channels are known. The hypothetical signal at low reconstructed squark masses is neglected although the events could have been selected. Thus, this approach leads to conservative selection efficiencies.

## 8.4 The modified frequentist approach

The problem of combining the results of several search channels for new particles is very complex. In the present analysis a modified frequentist approach based on the Likelihood Ratio is used. This method was used in the searches for the SM Higgs and MSSM Higgs bosons at LEP [18, 75]. In this analysis the implementation described in [76] is used. In the following only the basic concepts are summarised.

### The test statistic: Likelihood Ratio

In order to discriminate signal-like outcomes from background-like outcomes of a search with $n$ independent channels, one may define a test statistic $X$. It has been shown [75, 77–79] that a good choice for the test statistic is the Likelihood Ratio. For each selection channel, the Likelihood Ratio is defined as the ratio of the probabilities for observing exactly that outcome, assuming a signal + background ($s + b$) hypothesis and the background-only hypothesis. If $N$ is the total number of signal events, the expected number of signal events in the selection channel $i$ is given by $s_i = N \cdot (\varepsilon\beta)_i$, where $(\varepsilon\beta)_i$ is the total visible branching ratio of the selection channel[2]. With $b_i$ being the estimated background, and $d_i$ being the number of candidate events, the Likelihood Ratio of this selection channel is given by

$$X_i = \frac{e^{-(s_i+b_i)}(s_i + b_i)^{d_i}}{d_i!} \Bigg/ \frac{e^{-b_i} b_i^{d_i}}{d_i!} \quad . \tag{8.2}$$

For a set of $n$ channels the Likelihood Ratio is given by the product of the ratios of the independent channels:

$$X = \prod_{i=1}^{n} X_i \ . \tag{8.3}$$

[2]The total visible branching ratio $(\varepsilon\beta)_i$ of a selection channel $i$ is given by $(\varepsilon\beta)_i = \sum_k \varepsilon_{i,k}\beta_k$, where $\beta_k$ is the branching ratio of the squark decay mode $k$ and $\varepsilon_{i,k}$ is the corresponding efficiency in the selection channel $i$. The sum runs over all decay modes $k$ considered in this selection channel. With this definition the cross talk of Sec. 8.2 is taken into account.

This choice of the test statistic can be used to determine confidence levels (CL).

**Confidence levels in the modified frequentist approach**

By definition the CL for excluding the possibility of simultaneous presence of signal and background is the probability that the test statistic would be less than or equal to that observed in the data. This probability is given by a sum of Poisson probabilities [75]

$$CL_{s+b} = P_{s+b}(X \leq X_{obs}) = \sum_{X(\{d'_i\}) \leq X(\{d_i\})} \prod_{i=1}^{n} \frac{e^{-(s_i+b_i)}(s_i+b_i)^{d'_i}}{d'_i!} \quad , \tag{8.4}$$

where $X(\{d_i\})$ is the test statistic for the observed set of candidates in each channel $\{d_i\}$. The sum runs over all possible final outcomes $\{d'_i\}$ which lead to a test statistic less than or equal to the observed one. To quote exclusion limits $1 - CL_{s+b}$ could be used, but it has the disturbing property that a search with downward fluctuating background will set strong exclusion limits, simply because the observed outcome was determined to be unlikely in any case.

To correct for this effect the CL for the background alone must be calculated. It is given by [75]

$$CL_b = P_b(X \leq X_{obs}) \; , \tag{8.5}$$

where the probability sum is computed assuming the presence of the background only. This CL expresses the probability that background processes would give fewer than or equal to the number of candidates observed. Then the CL of the modified frequentist approach can be computed by

$$CL_s = CL_{s+b}/CL_b \; . \tag{8.6}$$

This CL is used to set exclusions limits. An upper limit $N_{\text{lim}}$ on the number of signal events is set such that $CL_s \leq 0.05$ for $N \geq N_{\text{lim}}$.

The task of summing the terms in Eq. 8.4 can be enormous. For $n$ channels each with $m$ possible outcomes there are $\mathcal{O}(n^m)$ terms to compute. The sum is carried out using the probability distribution functions for the test statistic. Systematic uncertainties on signal and background are taken into account by averaging over possible values of the signal and background assuming a Gaussian distribution, with the lower tail cut off at zero. For more details of the computation see [76].

## 8.5 Derivation of exclusion limits

The various selection channels are combined separately for the $e^+p$ and $e^-p$ data samples to set constraints on $\not{R}_p$ SUSY models. For a given set of parameters in a certain supersymmetric model the full supersymmetric mass spectrum (in particular the squark masses) and the BRs of all squark decay modes are calculated using the SUSYGEN package [46,47]. Then an upper limit $N_{\text{lim}}$ on the number of events coming from squark production can be calculated at a given CL using the modified frequentist approach. The following quantities enter this limit calculation.

- The numbers of events observed in the data of all selection channels. For the channels $eq$, $\nu q$, $eMJ$ with 'right' charge and $\nu MJ$ the numbers of data events are integrated within a mass bin around the calculated squark mass. For the channels $eMJ$ with 'wrong' charge, $e\ell MJ$ and $\nu\ell MJ$ no mass restriction is imposed.
- The corresponding numbers of events expected from SM background processes.
- The errors on the numbers of expected events considering the experimental as well as theoretical uncertainties of Sec. 4.7.
- The signal efficiency for all squark decay modes in all selection channels corrected for a non-negligible width (Sec. 8.3). The uncorrected efficiencies are retrieved from the calculated masses using the mass dependent parameterisation of the efficiencies.
- The uncertainties on the signal efficiencies considering the error sources listed in Sec. 5.1.3.
- The calculated branching ratios of all squark decay modes.

$N_{\mathrm{lim}}$ is then translated into a bound on the squark production cross section $\sigma_{\mathrm{lim}}$. The set of model parameters is excluded if $\sigma_{\mathrm{lim}}$ is smaller than the signal cross section. The theoretical uncertainties on the latter are included in the systematic errors of the signal efficiencies (cf. Sec. 5.1.3).

For non-vanishing Yukawa couplings $\lambda'_{131}$ or $\lambda'_{113}$ allowing for the resonant production of stop and sbottom squarks, the corresponding squark masses cannot be neglected in the calculation of the BRs. Thus these cases are treated separately. In addition, for $\lambda'_{131} \neq 0$ a top quark can be produced in gauge decays. The top quark always decays via $t \to bW$ leading to angular distributions of the decay products different to that of the first two generations for which the efficiencies have been determined. Conservatively, diagrams which lead to a top in the final state are thus not taken into account in the calculation of the BRs. Nevertheless, most of the stop decays are in fact covered by this analysis and would have been visible in the mass distribution.

## 8.6 Exclusion limits in the 'phenomenological' MSSM

Here a version of the MSSM is considered in which the couplings between two SUSY particles and a standard fermion/boson are determined by the usual MSSM parameters: the mass term $\mu$ which mixes the Higgs superfields, the SUSY soft-breaking mass parameters $M_1$, $M_2$ and $M_3$ for $U(1)$, $SU(2)$ and $SU(3)$ gauginos, and the ratio $\tan\beta$ of the vacuum expectation values of the two neutral scalar Higgs fields. These parameters are defined at the electroweak scale. It is assumed that the gaugino mass terms unify at the GUT scale leading to the usual relation between $M_1$, $M_2$ and $M_3$ given in Eq. 2.43.

The parameters $\mu$, $M_2$ and $\tan\beta$ are used to determine the masses and couplings of the neutralinos and charginos as explained in Sec. 2.4.1. The mass of the gluino $\tilde{g}$ is approximated by the value of $M_3$ at the EW scale. The sfermion (slepton and squark) masses are free parameters in this 'unconstrained' or 'phenomenological' MSSM. In order to reduce the number of free parameters in this model any possible mixing between sfermions is neglected and it is assumed that all squark states are degenerate in mass. This assumption enters in the calculation of BRs of the gauginos.

### 8.6.1 Particular supersymmetric scenarios

For particular settings of the MSSM parameters exclusion limits at 95 % CL have been derived on $\lambda'_{1j1}(j = 1, 2)$ and $\lambda'_{11k}(k = 1, 2)$ dependent on the squark mass. The results on $\lambda'_{1j1}$ follow from the analysis of $e^+p$ collisions, whereas the analysis of $e^-p$ collisions gives sensitivity to $\lambda'_{11k}$. For both cases the parameters are chosen such that the lightest neutralino is dominated either by its $\tilde{\gamma}$ component or by its $\tilde{Z}$ component (see Fig. 2.6).

#### Limits on $\lambda'_{1j1}(j = 1, 2)$ for a photino- and zino-like $\chi_1^0$

Example upper limits on $\lambda'_{1j1}$ for $j = 1, 2$ are shown in Fig. 8.3 (top) as a function of the squark mass. The case of a $\chi_1^0$ dominated by its $\tilde{\gamma}$ component is shown in the left panel of Fig. 8.3. The results for a zino-like $\chi_1^0$ are shown on the right side. The exclusion limits are calculated under certain assumptions for the slepton masses. The full curves represent cases where sleptons and squarks are degenerate in mass. The dashed curves indicate the limits for slepton masses fixed at 90 GeV close to the lowest mass bound from sfermion searches at LEP. For all four cases the gluino mass is large (due to the large values for $M_2$ and hence $M_3$) and squark decays to a $\tilde{g}$ are kinematically forbidden.

The HERA sensitivity allows tests of $\not{R}_p$ Yukawa couplings $\lambda'$ down to around $10^{-2}$ for squark masses around 100 GeV. For high squark mass values the sensitivity degrades since the production cross section decreases. For a squark mass of 290 GeV Yukawa couplings $\lambda'_{1j1}$ larger than 0.6 are ruled out. The limits for a zino-like $\chi_1^0$ (right panel) are slightly weaker at low squark masses, compared to the photino-like case because channels with a $\nu$ in the final state dominate whose efficiencies are low at small squark masses.

The relative contribution of all channels calculated for a $\lambda'$ value exactly at the exclusion limit are illustrated in the middle and the bottom panel of Fig. 8.3. In each case the total branching ratio covered is above 75 % and generally close to 100 %. Decay patterns involving more than two gauginos[3] or decay pattern which lead to tau leptons in the final state are not covered; they have only small BRs. In this sense, the analysis presented here cannot be improved by including other channels.

At large squark masses a large Yukawa coupling is necessary to allow squark production. As a result the decay channel $eq$ proceeding directly via $\not{R}_p$ becomes important[4]. For smaller masses the dominant channels in the case of a photino-like $\chi_1^0$ are those with an $e^\pm$ and several jets in the final state. In contrast, for a zino-like $\chi_1^0$ the $\nu$ channels dominate. This is a result of the dominant decay of the $\chi_1^0$.

The relative contribution of the gauge decay channels strongly depends on the slepton mass. For the case of a light slepton ($M_{\text{slepton}} = 90$ GeV) the decays of a $\chi_1^+$ into a lepton-slepton pair are kinematically allowed since for the two given MSSM parameter sets the

[3]Gauge decays with more than two gauginos are kinematically suppressed.

[4]The partial decay width of the lepton–quark decays of squarks is strongly dependent on $\lambda'$. This is nicely demonstrated by the strong correlation of the BR for $eq$ and the limit on $\lambda'$ in Fig 8.3. Note that the BRs are calculated exactly at the $\lambda'$ limit.

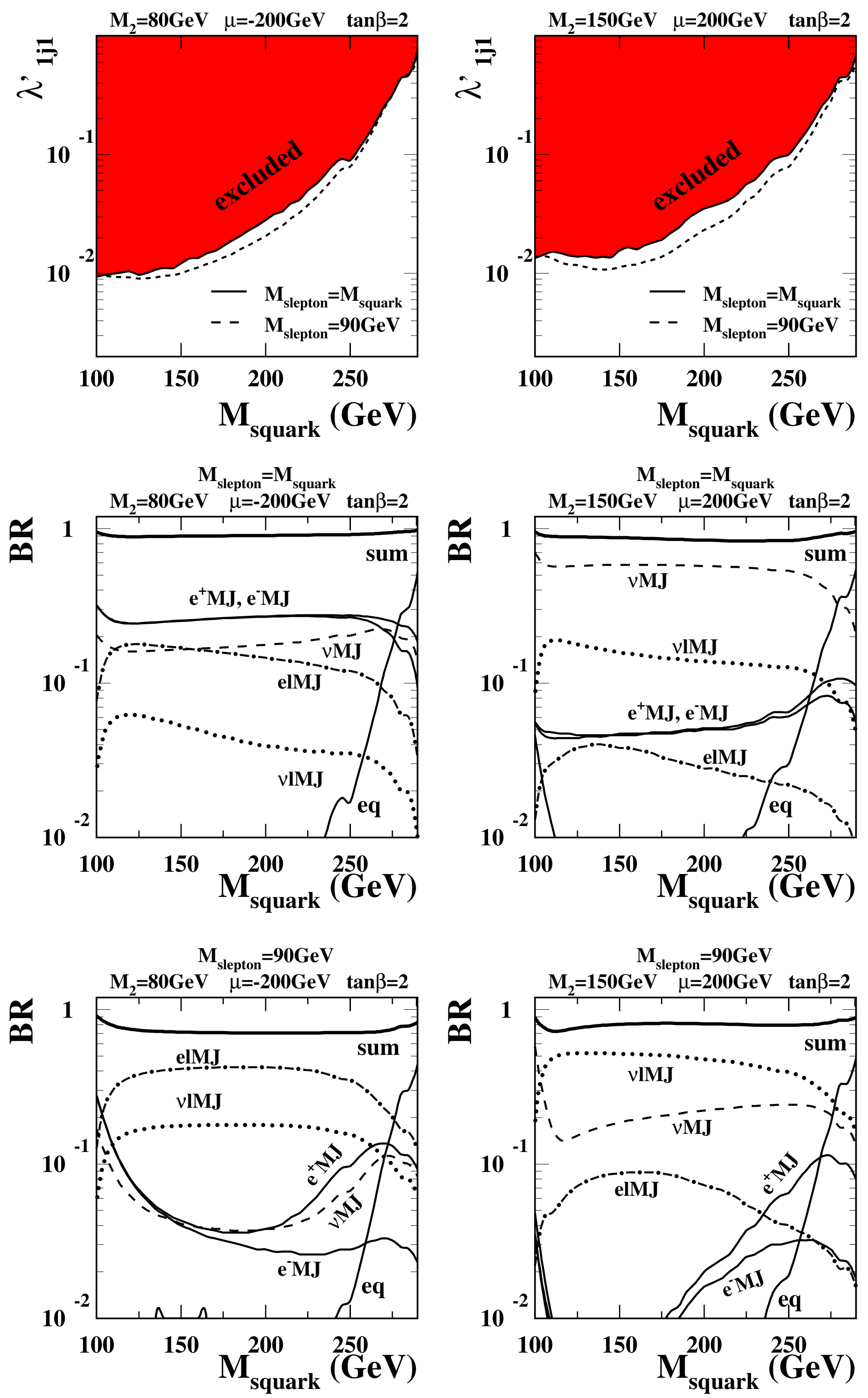


Figure 8.3: Exclusion limits (95 % CL) on $\lambda'_{1j1}$ with $j = 1, 2$ and the BRs of all channels for $\lambda'$ values just at the shown exclusion limit. Shown are the results for MSSM parameters leading to a $\chi_1^0$ dominated by its $\tilde{\gamma}$ component ($\mu = -200\,\text{GeV}$) (left) and by its $\tilde{Z}$ component ($\mu = 200\,\text{GeV}$) (right) when sleptons and squarks are assumed to be degenerate and for a slepton mass of 90 GeV.

$\chi_1^+$ has masses around 95 GeV. Thus cascade decays are possible leading to enhanced contributions of the channels $elMJ$ and $\nu lMJ$. On the other hand the dependence of the $\lambda'$ limit on the slepton mass is rather small since the sensitivity of all selection channels are quite similar.

#### Limits on $\lambda'_{11k}(k = 1, 2)$ for a photino- and zino-like $\chi_1^0$

The limits on $\lambda'_{11k}(k = 1, 2)$ derived from $e^-p$ collisions are shown in Fig. 8.4 as a function of the $\tilde{d}_R^k$ mass. Again the limits have been derived for MSSM parameters leading to a photino-like $\chi_1^0$ (left) or a zino-like $\chi_1^0$ (right) assuming either sleptons of 90 GeV (dashed curve) or sleptons and squarks to be degenerate in mass (full curve).

Although the amount of $e^+p$ data is five times bigger compared to $e^-p$ data, the limits on $\lambda'_{11k}$ derived from $e^-p$ are similar to the limits on $\lambda'_{1j1}$ derived from $e^+p$ collisions since the cross section for $\tilde{d}_R^k$ production is higher due to its coupling to an $u$ valence quark from the proton. The 'harder' $u$ density even leads to stronger limits at high masses. With the $e^-p$ data set Yukawa couplings of about 0.3 are excluded at a squark mass of 290 GeV.

The relative contributions of the selection channels calculated for $\lambda'$ values exactly at the limit are shown in the middle and lower parts of Fig. 8.4. For all cases the total branching ratio covered is very close to 100 %. Again the lepton–quark channels $eq$ and $\nu q$ are most relevant at high squark masses and high couplings. For lower masses the final states with several jets and an electron or positron dominate in the case of a photino-like $\chi_1^0$ resulting from the dominant decay of the latter. In contrast the case of a $\chi_1^0$ dominated by its zino component leads to an enhanced contribution of final states including a neutrino and several jets. The decay of a $\tilde{d}_R^k$ into a chargino is forbidden for $k = 1, 2$. Thus, the cascade decays of squarks are suppressed, but they can proceed via the $\chi_2^0$. As can be seen in Fig. 8.4 the relative contribution of $elMJ$ and $\nu lMJ$ is always very small even for cases where the slepton mass is low ($M_{\text{slepton}} = 90$ GeV). The relative contributions of the decay channels depend only weakly on the slepton mass. The same is true for the limits on $\lambda'_{11k}$.

### 8.6.2 Comparison with previous HERA results

There are previous results on the production of squarks in $\not{R}_p$ supersymmetry from HERA using H1 data from $e^-p$ collisions taken at a centre of mass energy of $\sqrt{s} = 296$ GeV [10] and from $e^+p$ collisions at $\sqrt{s} = 300$ GeV [11]. The $e^-p$ data were recorded in the starting phase of HERA in 1992/1993 and correspond to a rather small integrated luminosity of 420 nb$^{-1}$. Thus in the analysis presented here the amount of analysed data is increased by a factor of about 30. The $e^+p$ data taken in 1994–1997 correspond to an integrated luminosity of 37 pb$^{-1}$. With the present work the amount of data analysed is roughly doubled. The centre of mass energy of both $e^-p$ and $e^+p$ was increased by roughly 20 GeV compared to the previous results.

In [10] limits on the Yukawa coupling $\lambda'_{11k}$ have been derived for a photino-like $\chi_1^0$ with a mass of around 40 GeV. The particular parameter set $M_2 = 80$ GeV, $\mu = -200$ GeV and $\tan\beta = 2$ leads to such a configuration. In Fig. 8.5 (left) the limits from [10] and the limits derived in the present analysis are shown as a function of the squark mass. The enormous increase of integrated luminosity and more sophisticated analysis methods lead

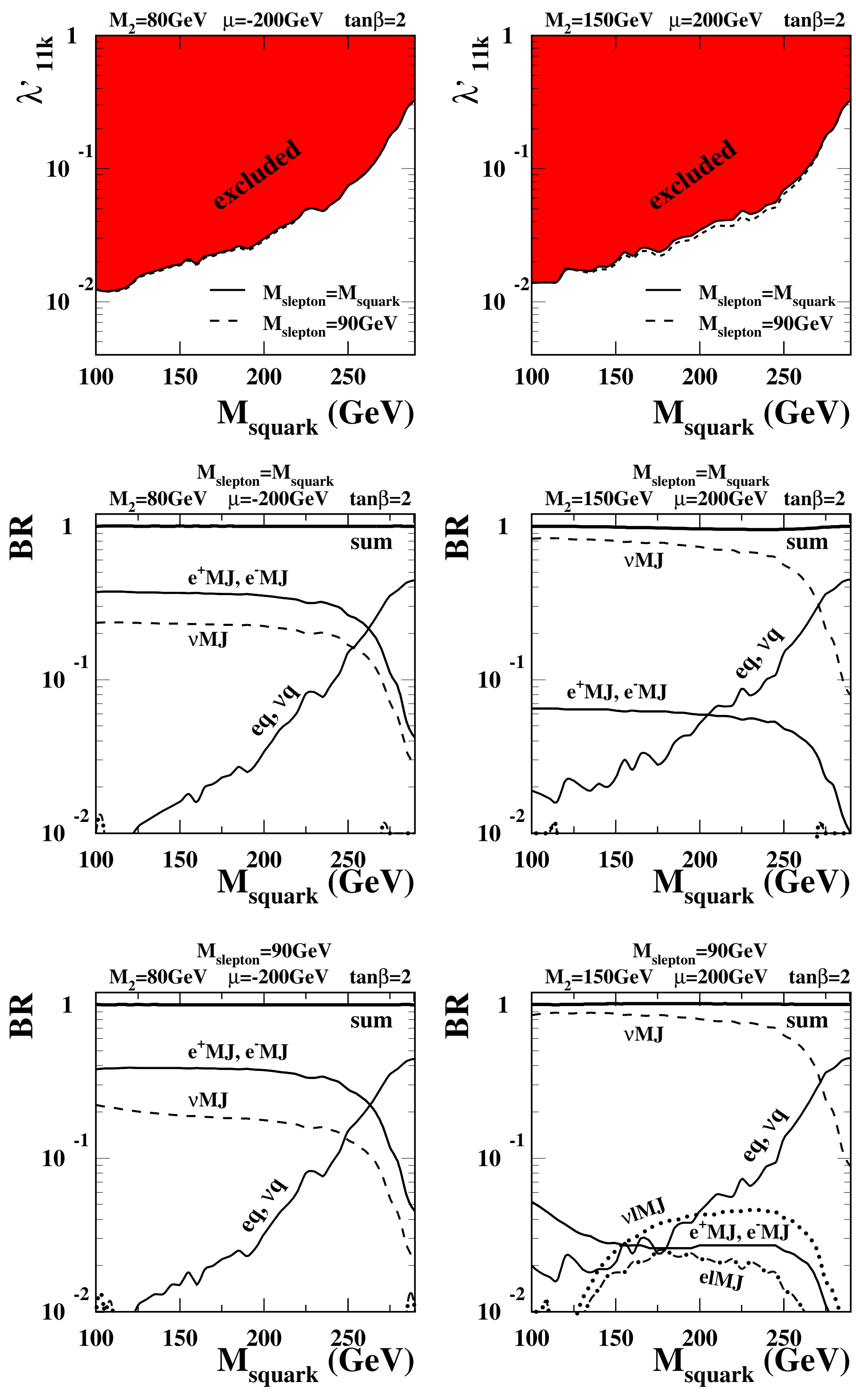


FIGURE 8.4: Exclusion limits (95 % CL) on $\lambda'_{11k}$ with $k = 1, 2$ and the BRs of all channels for $\lambda'$ values just at the shown exclusion limit. Shown are the results for MSSM parameters leading to a $\chi^0_1$ dominated by its $\tilde{\gamma}$ component ($\mu = -200\,\text{GeV}$) (left) and by its $\tilde{Z}$ component ($\mu = 200\,\text{GeV}$) (right) when sleptons and squarks are assumed to be degenerate and for a slepton mass of 90 GeV.

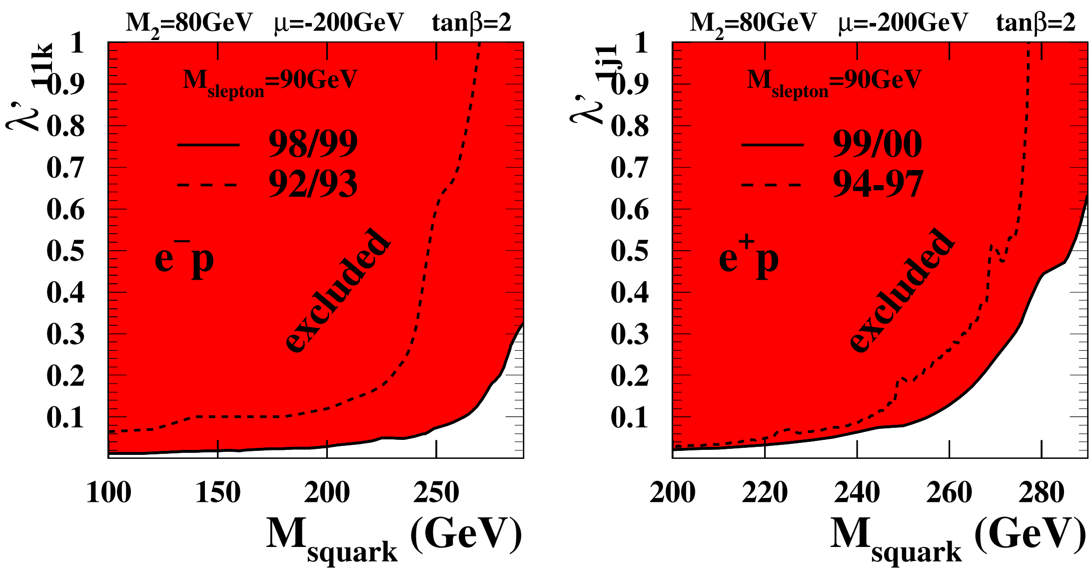


FIGURE 8.5: Comparison with previous HERA results [10, 11]. Shown are the limits on $\lambda'_{11k}$ ($k = 1, 2$) (left) derived from $e^-p$ collisions and the limits on $\lambda'_{1j1}$ ($j = 1, 2$) (right) derived from $e^+p$ collisions for MSSM parameters leading to a photino-like $\chi_1^0$ of 40 GeV.

to an improvement of the exclusion limits throughout the full mass range of more than a factor of four. In addition the increase of centre of mass energy allows extending the search towards larger squark masses. For $\lambda'_{11k} = 0.3$ the old limit covers mass values up to $\sim 240$ GeV. Now squark masses up to 290 GeV can be tested. A new kinematic window has been opened.

This is also true for $\tilde{u}_L^j$ production. In the right panel of Fig. 8.5 the limits from [11] for $M_2 = 80$ GeV, $\mu = -200$ GeV, $\tan\beta = 2$ and $M_{\text{slepton}} = M_{\text{squark}}$ are illustrated by the dashed line. The new limits are given by the full line. In particular at high squark masses the limits on $\lambda'_{1j1}$ are drastically improved. At low squark masses the limits are improved by a few percent. Note that the limit calculation tools have been revised in comparison to the analysis presented in [11].

### 8.6.3 Scan of the supersymmetric parameter space

In order to systematically investigate the sensitivity dependence on the supersymmetric parameters, a scan of the parameters $M_2$ and $\mu$ is performed for two values of $\tan\beta$ ($\tan\beta = 2$ and $\tan\beta = 6$). Again, sleptons are assumed to be degenerate, and their mass $M_{\tilde{l}}$ is set to a fixed value of 90 GeV. Other values would however lead to very similar results as can be seen in Fig. 8.3 and Fig. 8.4. The parameters $M_2$ and $\mu$ are varied in the range $70\,\text{GeV} < \text{M}_2 < 350\,\text{GeV}$ and $-300\,\text{GeV} < \mu < 300\,\text{GeV}$. Parameter points which lead to a scalar LSP or to LSP masses below 30 GeV are not considered. This latter restriction, as well as the lower value for $M_2$, are motivated by the exclusion domains resulting from

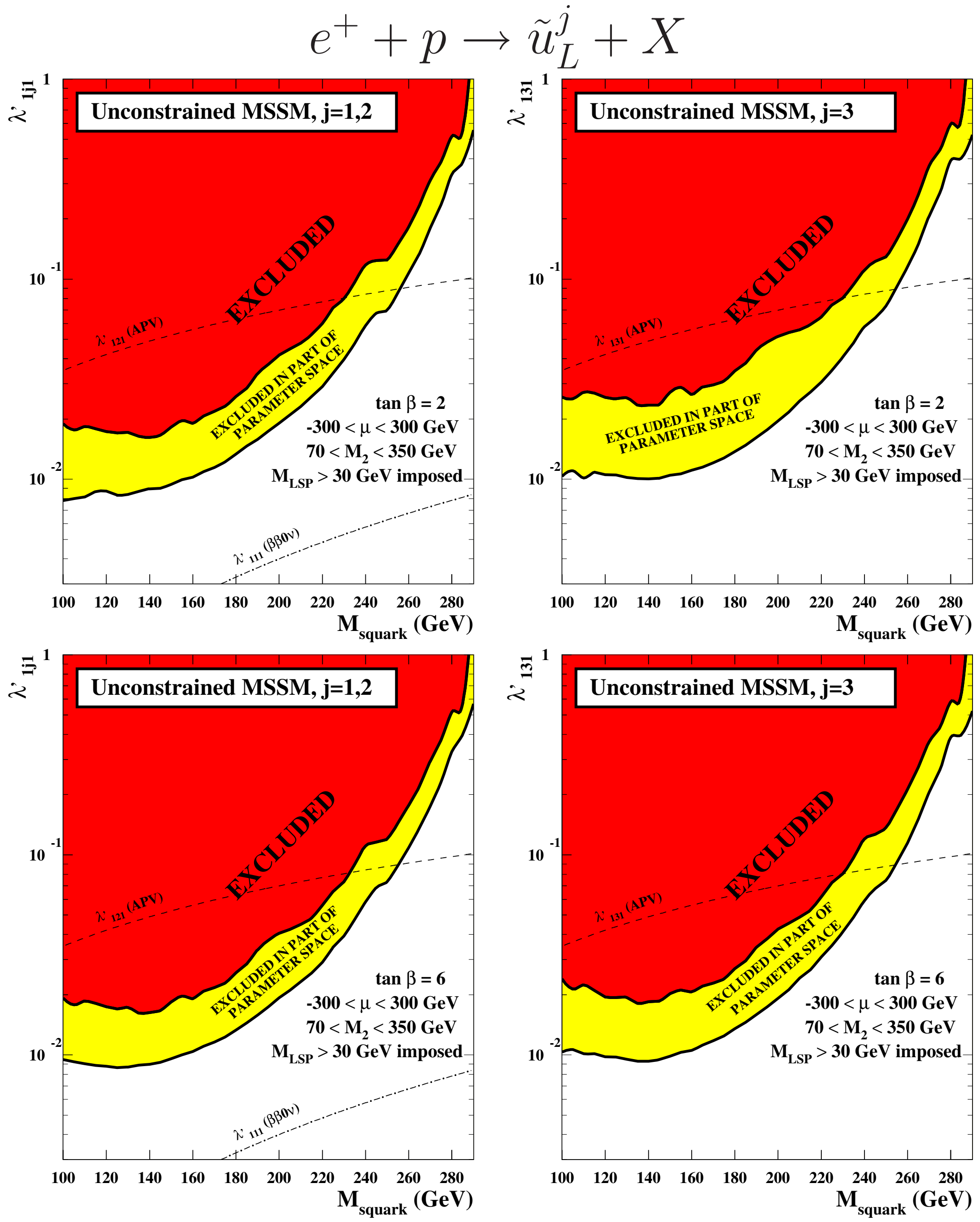


Figure 8.6: Exclusion limits (95 % CL) on $\lambda'_{1j1}$ for $j = 1, 2$ (left) and $j = 3$ (right) as a function of the squark mass for $\tan\beta = 2$ (top) and for $\tan\beta = 6$ (bottom) from a scan of the MSSM parameter space as indicated in the figures. The two full curves indicate the strongest and the weakest limits on $\lambda'$ in the parameter space investigated. Indirect limits from neutrinoless double beta decay experiments ($\beta\beta 0\nu$) [12] and atomic parity violation (APV) [13, 14] are also shown.

$\chi$ searches in $\not R_p$ SUSY at LEP (e.g. [15]). For each point in this $(\mu, M_2)$-plane the upper bounds $\lambda'_{\text{lim}}$ on the coupling $\lambda'_{1j1}$ and $\lambda'_{11k}$ are obtained. As explained above the case of non-vanishing coupling $\lambda'_{131}$ and $\lambda'_{113}$ must be treated separately.

Fig. 8.6 shows the results for $\lambda'_{1j1}$ $(j = 1, 2)$ (left) and $\lambda'_{131}$ (right) coming from the analysis of $e^+p$ data. The exclusion limits for $\tan\beta = 2$ are shown in the top panels; the lower panels give the corresponding results for $\tan\beta = 6$. The two full curves in each of these figures indicate the maximal and minimal values obtained for $\lambda'_{\text{lim}}$ within the parameter space investigated. Thus they represent the strongest and the weakest limit on $\lambda'$, i.e. the red region is excluded in the full parameter space, whereas the yellow region is ruled out in parts of the SUSY parameter space only.

The limits on both $\lambda'_{1j1}$ and $\lambda'_{131}$ are widely independent of the SUSY parameters as can be seen from the narrow region that is excluded only in parts of the parameter space in each plot and from the small differences of the results for $\tan\beta = 2$ and 6. For a Yukawa coupling of electromagnetic strength, $(\lambda'_{1j1} = 0.3)$ $\tilde{u}_L$, $\tilde{c}_L$ and $\tilde{t}_L$ squarks with masses below $\sim 275$ GeV are excluded at 95% CL.

Fig. 8.7 shows the corresponding exclusion limits on $\lambda'_{11k}$ $(k = 1, 2)$ (left) and $\lambda'_{113}$ (right) resulting from the analysis of the $e^-p$ collision data set. $\tilde{d}_R$, $\tilde{s}_R$ and $\tilde{b}_R$ squarks with masses below $\sim 280$ GeV are excluded at 95% CL for a Yukawa coupling of electromagnetic strength $(\lambda'_{11k} = 0.3)$. The dependence of the exclusion limits on the MSSM parameters is again found to be small.

**Comparison with low-energy experiments**

The direct HERA results compete with indirect limits from low energy experiments [14]. The available indirect limits are indicated in Fig. 8.6 and Fig. 8.7 by dashed and dotted lines. The production of squarks via a $\lambda'_{111}$ coupling is severely constrained by the non-observation of neutrinoless double beta decay [12]. However, this limit[5] is obtained indirectly. The best indirect limit on the couplings $\lambda'_{121}$ and $\lambda'_{131}$ which could allow the production of $\tilde{c}$ and $\tilde{t}$ squarks comes from atomic parity violation (APV) measurements [13, 14]. By the analysis presented here these indirect limits on $\tilde{c}$ and $\tilde{t}$ squarks $(\lambda'_{121} \neq 0,\ \lambda'_{131} \neq 0)$ are extended for masses up to $\sim 240$ GeV. The best indirect limit on the coupling $\lambda'_{112}$ $(\lambda'_{113})$ which could allow the production of $\tilde{s}$ $(\tilde{b})$ squarks results from charge current universality (CCU) [14]. The HERA limits extend the excluded region for squarks of the second and third family $(\lambda'_{112} \neq 0,\ \lambda'_{113} \neq 0)$ for masses up to $\sim 240$ GeV in part of the parameter space.

## 8.7 Exclusion limits in the Minimal Supergravity Model

In this section exclusion limits are derived on parameters of the more constrained minimal Supergravity Model (mSUGRA) [32] (see Sec. 2.4.2). The model assumes a universal mass parameter $m_0$ $(m_{1/2})$ for all sfermions (gauginos) at the GUT scale. With the assumption of Radiative Electroweak Symmetry Breaking (REWSB) the model is completely determined by five free parameters: $m_0$, $m_{1/2}$, $A_0$, $\tan\beta$, and the sign of $\mu$. In contrast to the

[5]The limits from double beta decay experiments in Fig. 8.6 are given assuming a gluino mass of 1 TeV.

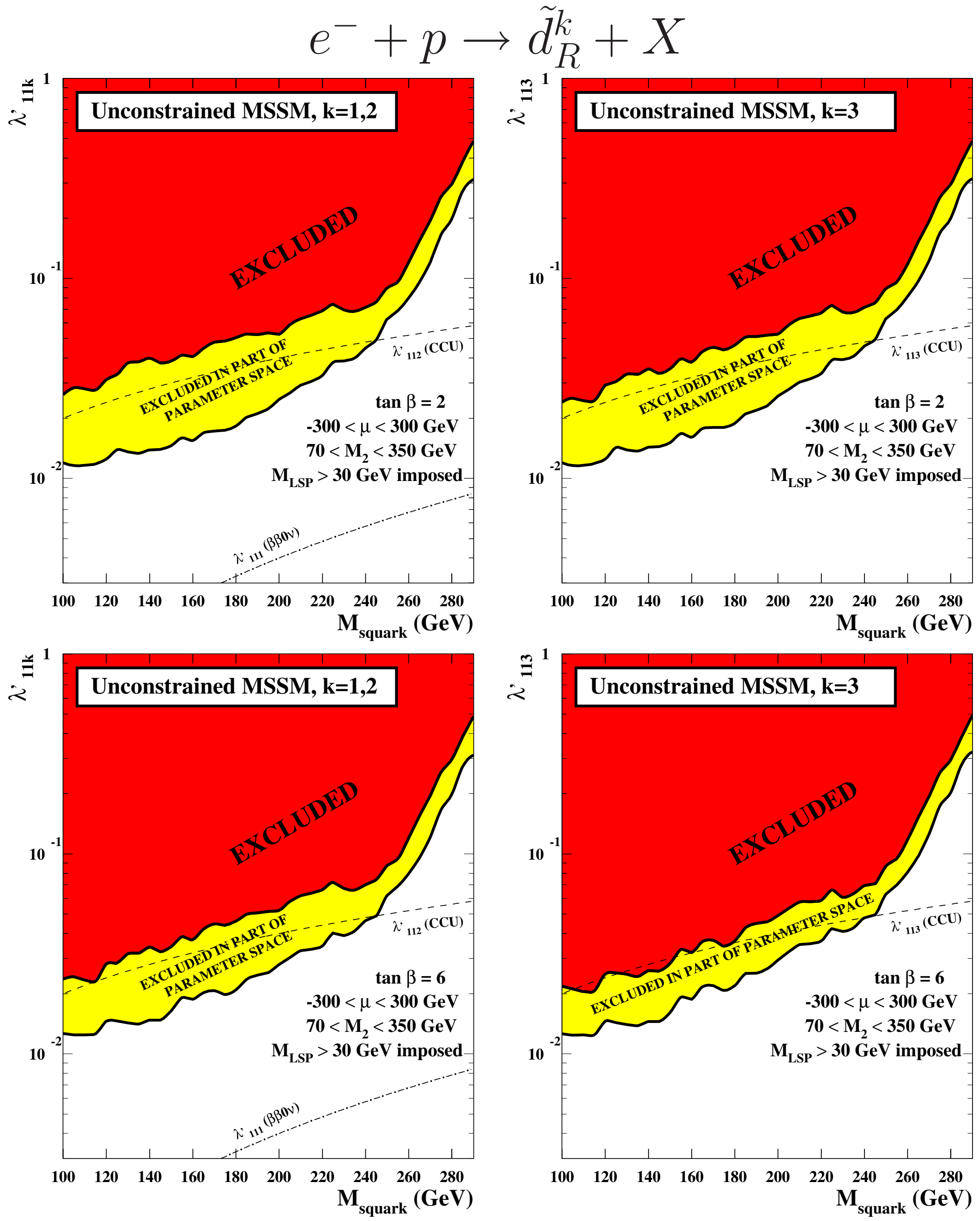


Figure 8.7: Exclusion limits (95 % CL) on $\lambda'_{11k}$ for $k = 1, 2$ (left) and $k = 3$ (right) as a function of the squark mass for $\tan\beta = 2$ (top) and for $\tan\beta = 6$ (bottom) from a scan of the MSSM parameter space as indicated in the figures. The two full curves indicate the strongest and the weakest limits on $\lambda'$ in the parameter space investigated. Indirect limits from neutrinoless double beta decay experiments ($\beta\beta0\nu$) [12] and charged current universality (CCU) [14] are also shown.

phenomenological MSSM the sfermion masses at the electroweak scale are related to each other and to the parameters determining the gaugino sector.

For a given set of mSUGRA parameters the masses of all supersymmetric particles (including squarks) and the BRs of all squark decay modes are calculated using SUSYGEN which is based on SUSPECT 2.1 [80]. Assuming a fixed value for the $\not{R}_p$ couplings $\lambda'_{1j1}$ or $\lambda'_{11k}$, constraints on the mSUGRA parameters can be set; for example on $(m_0, m_{1/2})$ when $\tan\beta$, $A_0$, and the sign of $\mu$ are fixed. $A_0$ enters only marginally in the interpretation of the results and is set to zero.

Parameter values leading to a LSP lighter than 30 GeV have not been excluded here. Conservatively a vanishing efficiency has been assumed for squarks undergoing a gauge decay ending in a $\chi$ or $\tilde{g}$ lighter than 30 GeV since the parameterisation of the efficiencies is not valid in this domain.

### 8.7.1 Results for the first and second squark family

For $\mu < 0$, exclusions limits at 95 % CL obtained for a Yukawa coupling $\lambda'_{1j1} = 0.3$ $(j = 1, 2)$ in the $(m_0, m_{1/2})$-plane are shown in Fig. 8.8 (panels on the left) for three values of $\tan\beta = 2, 6$ and 10. The corresponding results for $\lambda'_{11k} = 0.3$ $(k = 1, 2)$ derived from $e^-p$ data are shown in Fig. 8.9 (panels on the left). The dark domains at low $m_0$ and $m_{1/2}$ correspond to values of the parameters where REWSB is not possible or where the LSP is a sfermion.

The constraints on $(m_0, m_{1/2})$ are very similar for all values of $\tan\beta$ and both $\not{R}_p$ coupling types, $\lambda'_{1j1}$ and $\lambda'_{11k}$, since the mixing of the squark states is very small for $j = 1, 2$ and $k = 1, 2$. The excluded regions follow approximately curves of equal squark masses. For $\lambda'_{1j1} = 0.3$ the parameter space where $M_{\tilde{q}} < 275$ GeV is nearly fully excluded. For $\lambda'_{11k} = 0.3$ the squark mass limit is slightly higher, around 280 GeV. For the latter, more stringent limits are achieved because of the higher squark production cross section in $e^-p$ collisions.

For both $\lambda'_{1j1} = 0.3$ and $\lambda'_{11k} = 0.3$ the sensitivity slightly decreases for lower values of $m_{1/2}$ since the gaugino masses become smaller leading to smaller selection efficiencies in gauge decay channels. If the mass of a certain gaugino falls below 30 GeV the sensitivity slightly drops since the selection efficiencies of the corresponding gauge decay channels are conservatively set to zero as mentioned above. At very low $m_{1/2}$ values the lightest $\chi$'s and even the gluino have masses below 30 GeV. The sensitivity on the squark mass drops strongly in this case since all gauge decay channels are conservatively not considered as mentioned above. Only the lepton–quark channel $eq$ – and in the case of $\lambda'_{11k} = 0.3$ the $\nu q$ channel – still contributes.

In addition limits on $(m_0, m_{1/2})$ have been derived for $\tan\beta = 2$ and a lower $\not{R}_p$ coupling: $\lambda'_{1j1} = 0.1$ $(j = 1, 2)$. The excluded domain is indicated in Fig. 8.8 (upper left panel) by the hatched area and is smaller than that obtained for $\lambda' = 0.3$. The parameter space leading to $M_{\tilde{q}} < 260$ GeV is ruled out at low $m_0$. For high $m_0$ this limit is reduced to $M_{\tilde{q}} < 200$ GeV because of the effects related to the gaugino masses previously mentioned.

$$e^+ + p \longrightarrow \tilde{u}_L^j + X$$

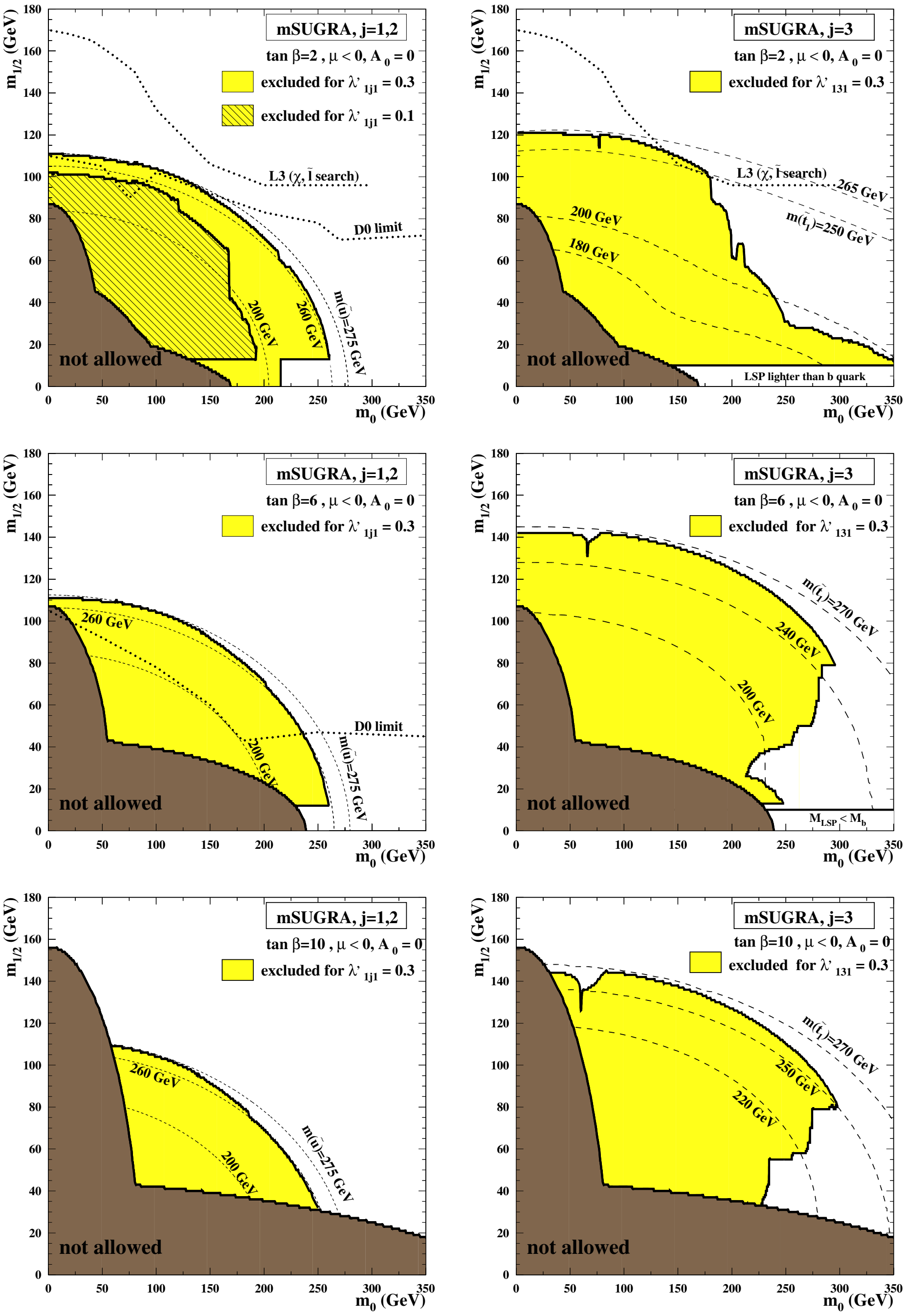


FIGURE 8.8: Exclusion limits (95 % CL) in mSUGRA with $\tan\beta = 2, 6$ and 10 for $\lambda'_{1j1} = 0.3$ ($j = 1, 2$) (left), i.e. $\tilde{u}$ and $\tilde{c}$ production, and for $\lambda'_{131} = 0.3$ (right), i.e. $\tilde{t}$ production. The dark region corresponds to values of the parameters where REWSB is not possible or where the LSP is a sfermion. The dashed lines indicate the curves of constant squark mass. The limits from LEP and TeVatron are given by the dotted lines.

**Comparison with LEP and TeVatron**

Results from the D0 experiment [16] from searches for $\not{R}_p$ supersymmetry are also shown in Fig 8.8 and Fig 8.9 as dotted lines. The analysis considers the production of two supersymmetric particles which decay violating $R_p$ via $\lambda'$ into electrons leading to di-electron event signatures. Resultingly the limits are independent of $\lambda'$. In the low $m_0$ region the D0 limit follows a curve of constant squark mass since here the pair production of squarks contributes most to the di-electron signal. At high values of $m_0$ the main process leading to the di-electron topology at the TeVatron is the production of gluinos, $\chi_1^\pm$ and $\chi_2^0$. The masses of these particles, as well as their production cross sections, do not change much with the variation of $m_0$ leading to a small dependence of the D0 exclusion limit on $m_0$. For large values of $\tan\beta$, the lightest neutralino is dominated by its zino component and its decay into $e^\pm$ is suppressed. As a result the sensitivity of the di-electron D0 analysis decreases for $\tan\beta = 6$.

For $\tan\beta = 2$ the limits obtained with the present analysis are competitive with or more stringent than the D0 results for low values of $m_0$. In the case of $\tan\beta = 6$ the domain excluded by the present analysis extends considerably beyond the region ruled out by the D0 experiment for $m_0 \lesssim 250\,\mathrm{GeV}$ since the dominant squark decay mode in the case of zino-like $\chi_1^0$ is still observable in the analysis presented here via the $\nu MJ$ and $\nu\ell MJ$ channels. At high $m_0$ the TeVatron analysis has higher sensitivity to $\not{R}_p$ mSUGRA for both $\tan\beta = 2$ and $\tan\beta = 6$.

The mSUGRA parameter space is still more constrained by the searches for pair produced $\chi^\pm$'s, $\chi^0$'s and sleptons at LEP [15] which give limits independent of $\lambda'$. They are indicated in the upper left panels of Fig. 8.8 and Fig. 8.9 by dotted curves. The $\not{R}_p$ decay of these supersymmetric particles via couplings $\lambda'$ leads to experimental signatures with several jets and leptons. Although $\tan\beta = 2$ is the only $\tan\beta$ value considered in [15] results for higher values are expected to be similar.

### 8.7.2 Results on stop and sbottom production

A non-vanishing coupling $\lambda'_{131}$ could lead to the production of a stop squark. The weak stop eigenstates $\tilde{t}_L$ and $\tilde{t}_R$ mix through an angle $\theta_t$ as shown in Eq. 2.32 to form the mass eigenstates $t_1$ and $t_2$, whose production cross sections scale as $\lambda'^2_{131}\cos^2\theta_t$ and $\lambda'^2_{131}\sin^2\theta_t$, respectively. Thus the lighter state does not necessarily have the largest production cross section. Similarly, for a non-vanishing $\lambda'_{113}$ sbottom production could be possible. The weak sbottom states $(\tilde{b}_L, \tilde{b}_R)$ mix to form the mass eigenstates $\tilde{b}_1$ and $\tilde{b}_2$ and the production cross section for $\tilde{b}_1$ $(\tilde{b}_2)$ scales as $\lambda'^2_{113}\sin^2\theta_b$ $(\lambda'^2_{113}\cos^2\theta_b)$. The treatment of stop production is explicitly described in the following. The sbottom mixing is treated in the same way.

For the channels where the signal is integrated over the whole mass range the fraction of the visible signal in a given selection channel, $k$, is

$$\sum_{i=1,2} (\beta\varepsilon)_{k,i}\sigma_i/\sigma_{\mathrm{tot}}, \tag{8.7}$$

where $(\beta\varepsilon)_{k,i}$ is the total visible BR of the selection channel $k$ for the state $\tilde{t}_i$, $\sigma_i$ is the production cross section of $\tilde{t}_i$, and $\sigma_{\mathrm{tot}} = \sigma_1 + \sigma_2$ is the total signal cross section. For the

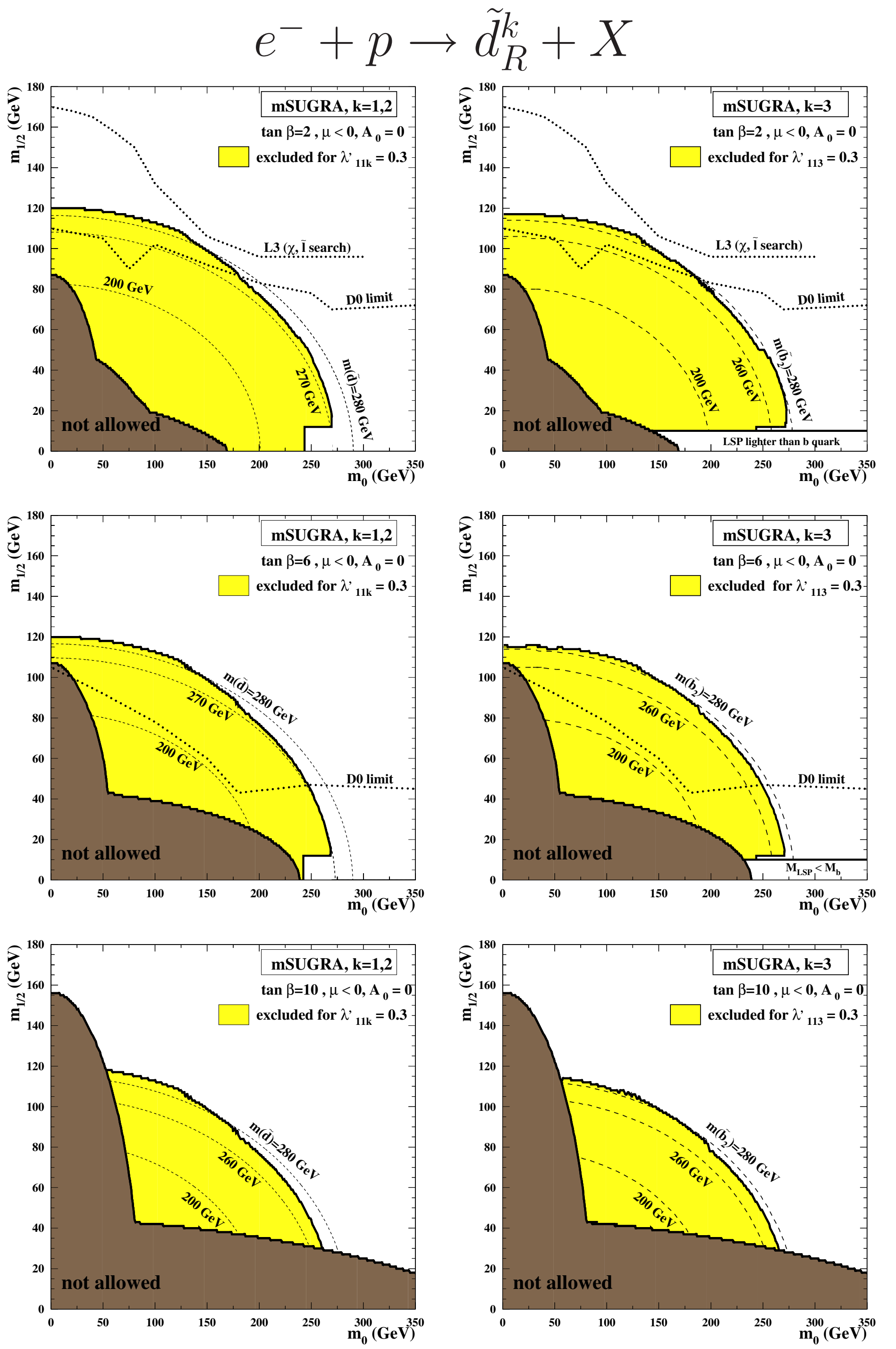


FIGURE 8.9: Exclusion limits (95 % CL) in mSUGRA with $\tan\beta = 2, 6$ and 10 for $\lambda'_{11k} = 0.3$ with $(k = 1, 2)$ (left), i.e. $\tilde{d}$ and $\tilde{s}$ production, and for $\lambda'_{113} = 0.3$ (right), i.e. $\tilde{b}$ production. The dark region corresponds to values of the parameters where REWSB is not possible or where the LSP is a sfermion. The dashed lines indicate the curves of constant squark mass. The limits from LEP and TeVatron are given by the dotted lines.

channels where the signal is integrated over a sliding mass bin only the contribution of the state $\tilde{t}_i$ for which the sensitivity is maximal, i.e. which maximises $\sigma_i(\sum_k(\beta\varepsilon)_{k,i})$, is taken into account in the summation above. The numbers of observed and expected events are then integrated in the mass bin corresponding to the state $\tilde{t}_i$ only.

This simplified method avoids the problems related to the exclusivity of selection channels which would occur in an analysis considering simultaneously the production of both states. Only the state with the highest sensitivity is considered in the limit derivation.

Using this procedure for both, the stop and the sbottom case, exclusion limits have been derived for $A_0 = 0$, $\mu < 0$ and $\tan\beta = 2, 6$ and 10. The excluded regions in the $(m_0, m_{1/2})$-plane for $\lambda'_{131} = 0.3$ (stop) and $\lambda'_{113} = 0.3$ (sbottom) are shown in Fig. 8.8 (panels on the right) and Fig. 8.9 (panels on the right), respectively. The domain below the line $m_{1/2} \lesssim 10\,\mathrm{GeV}$ is not considered since it corresponds to cases where the only allowed LSP decay into $\nu b\bar{d}$ is kinematically forbidden.

In the case of stop production (Fig. 8.8, panels on the right) the excluded domain is larger than that ruled out previously for $\lambda'_{1j1} = 0.3$ $(j = 1, 2)$ since the mixing of the stop states leads to $\tilde{t}_1$ masses smaller than the masses of the other $\tilde{u}^j_L$ squarks. For this reason particularly large values of $m_0$ are ruled out for $\tan\beta = 2$. The HERA sensitivity follows curves of equal $\tilde{t}_1$ masses as long as $m_{1/2}$ is large enough to ensure that the masses of the gauginos are above 30 GeV. When the $\chi^0_1$ becomes too light, the efficiencies for the channels involving a $\chi^0_1$ (in particular the process $\chi^+_1 \to \chi^0_1$) are set to zero, and the sensitivity to the signal is only provided by the $eq$ channel or by the decays $\tilde{t} \to b\chi^+_1$ followed by a $\not{R}_p$ decay of the chargino. For even smaller $m_{1/2}$, if the mass of the $\chi^+_1$ is below 30 GeV only the $eq$ channel contributes. As a result, for all values of $\tan\beta$ there are two steps in the excluded domain. For $\tan\beta = 2$ $(6, 10)$ $\tilde{t}_1$ masses up to 265 GeV (270 GeV) are excluded for $\lambda'_{131} = 0.3$. These masses are smaller than the maximal sensitivity reached for the same coupling value for $j = 1, 2$ because of the $\cos^2\theta_t$ reduction of the $\tilde{t}_1$ cross section. The narrow domains at $m_0 \sim 70\,\mathrm{GeV}$ and high $m_{1/2}$, which are not excluded, are related to decay modes involving more than two intermediate gauginos which open since the masses of certain sneutrino states become small in this region.

In the case of sbottom production (Fig. 8.9, panels on the right) the limits are similar to those obtained for $k = 1, 2$ since the mixing in the sbottom sector is small at these values of $\tan\beta$. The sensitivity follows curves of equal $\tilde{b}_2$ masses because the production cross section for this state is much higher than for $\tilde{b}_1$ if the mixing angle is small. The parameter space leading to $\tilde{b}_2$ masses up to $\sim 280\,\mathrm{GeV}$ is ruled out.

### Comparison with LEP and TeVatron

For $\tan\beta = 2$ and $\lambda'_{131} = 0.3$ the limits obtained by the present analysis are comparable to the L3 sensitivity in $\chi$ and slepton searches at intermediate values of $m_0$. In the same part of the parameter space the present limits extend considerably beyond the LEP sensitivity which is expected for higher values of $\tan\beta$. The excluded domain for sbottom production with $\lambda'_{113} = 0.3$ extends considerably beyond the reach of the TeVatron for $m_0 \lesssim 250\,\mathrm{GeV}$ and is comparable to the LEP sensitivity for intermediate $m_0$.

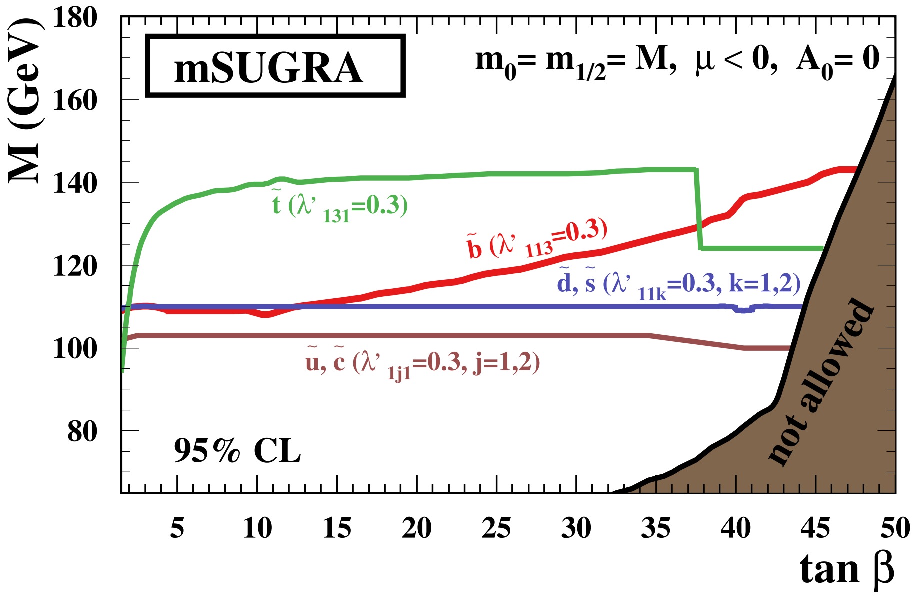


Figure 8.10: Exclusion limits for $m_0 = m_{1/2} = M$ in mSUGRA as a function of $\tan\beta$. Shown are the 95 % CL exclusion limits for $\lambda'_{1jk} = 0.3$. The areas below the curves are excluded. The dark region corresponds to values of the parameters where REWSB is not possible or where the LSP is a sfermion.

### 8.7.3 Dependence of the results on $\tan\beta$

Searches for the MSSM Higgs boson at LEP exclude a large part of the parameter space for small values of $\tan\beta$ (e.g. [81]). In order to enlarge the tested parameter space to larger values of $\tan\beta$, the dependence of the present analysis on $\tan\beta$ has been analysed by a scan of this parameter. The number of free parameters is reduced by setting the masses $m_0$ and $m_{1/2}$ to a common value called $M$. Thus it is assumed that both gaugino and sfermion masses unify at the GUT scale to the common value $M$.

The limits on $M$ are shown in Fig. 8.10 as a function of $\tan\beta$ for a fixed value of $\lambda'_{1jk} = 0.3$. Using the results from $e^+p$ and $e^-p$ collisions the production of all six squark flavours are considered. $M$ values below the curves are excluded at 95 % CL. For the first two families the exclusion curves are rather flat since mixing effects are very small as outlined in Sec. 2.4.1. Assuming equal $R\!\!\!/_p$ couplings a larger part of the parameter space is excluded for $\tilde{d}$ and $\tilde{s}$ production (shown in blue) than for $\tilde{u}$ and $\tilde{c}$ production (dark red) because of the higher squark production cross section in $e^-p$ collisions.

For squarks of the third family mixing effects are important. With high values of $\tan\beta$ the increase of the mixing angle $\theta_b$ results in an improvement of the sbottom limit (shown in red) since it leads to a smaller $\tilde{b}_1$ mass giving a higher $\tilde{b}_1$ production cross section. As mentioned in Sec. 2.4.1 the mixing in the sbottom sector becomes important for $\tan\beta \gtrsim 10$. At lower values the sensitivity is mainly provided by the state $\tilde{b}_2$ as discussed in the previous section for the particular cases $\tan\beta = 2, 6, 10$.

The mixing effects are largest in the stop sector leading to very stringent limits on $M$ (shown in green). For very low values of $\tan\beta$ the $\cos^2\theta_t$ reduction of the $\tilde{t}_1$ production cross section is important. For values of $\tan\beta \gtrsim 37$ the mixing of the two stau ($\tilde{\tau}$) states opens decay chains involving staus which result in final states including $\tau$ leptons. These channels are not searched for explicitly. Thus in this region of the parameter space the limit on stop production becomes less restrictive.

# Chapter 9

# Summary and Outlook

In this thesis a search for squarks in $\not{R}_p$ supersymmetric models is presented. The most general supersymmetric extension of the Standard Model violates the conservation of $R_p$. Additional vertices between two ordinary SM particles and one SUSY particle are then allowed which imply the resonant production of supersymmetric particles at colliders. At HERA the $\not{R}_p$ superpotential term $\lambda' LQ\overline{D}$ is of particular interest since it allows single squarks to be produced in $e^{\pm}p$ collisions. By investigating both $e^-p$ and $e^+p$ collisions, the squark production of all six flavours can be tested. In the present analysis $13.5\,\mathrm{pb}^{-1}$ of $e^-p$ and $64.3\,\mathrm{pb}^{-1}$ of $e^+p$ collisions, which were recorded at a centre of mass energy of $\sqrt{s} = 320\,\mathrm{GeV}$, have been studied.

In $\not{R}_p$ supersymmetry the *golden signature* of $R_p$ conserving SUSY (missing energy) is lost. In contrast squarks can decay in a large variety of decay modes involving several intermediate supersymmetric particles. This leads to a large number of different signatures in the final state. In this analysis nine (eight) decay topologies have been studied in $e^-p$ ($e^+p$) collisions. They rely on the number of charged leptons, hadronic jets and missing energy in the event. For almost all SUSY scenarios the sum of the BRs of these channels is close to one.

In none of the channels is a significant deviation from the Standard Model prediction found. The final states of lepton–quark decay modes, where production and decay proceeds via the $\not{R}_p$ coupling, are in agreement with the SM. The same is true for the final states of the gauge decays with multiple jets. Even very striking topologies which are almost free of SM background like multiple lepton final states and channels with a 'wrong' charged electron or positron are described by the SM. Thus no hint for squark production is found in the data.

The results in the decay channels have been used to restrict the parameter space of various supersymmetric models. These exclusion limits have been derived with a confidence level of 95 % using a modified frequentist approach which is based on Likelihood Ratios.

In the phenomenological MSSM with $\not{R}_p$ the masses of the scalar particles (sleptons and squarks) are free and the supersymmetric parameters $\mu$, $M_2$ and $\tan\beta$ are used to calculate the gaugino masses. Limits on the $\not{R}_p$ coupling constants $\lambda'_{1jk}$ have been derived as a function of the squark mass. These limits extend beyond the limits on squark production previously determined at HERA: Because of the enormous enlargement of the $e^-p$

data sample and more sophisticated analysis techniques, the limits on $\lambda'_{11k}$ are drastically improved throughout the complete mass domain. For both data sets, $e^+p$ and $e^-p$, the increase of the centre of mass energy leads to a strong improvement of the exclusion limits on $\lambda'_{1j1}$ and $\lambda'_{11k}$ in particular at high squark masses. A new kinematic domain has been opened. Assuming Yukawa couplings of electromagnetic strength ($\lambda'_{1jk} = 0.3$) squarks of all six flavours are ruled out with masses up to 275 GeV. This result extends beyond the reach of other collider experiments. The direct limits of this analysis compete with indirect limits from low energy experiments. For some squark flavours the presented results improve these indirect limits for masses up to 240 GeV.

Exclusion limits are also derived in a more restricted SUSY model. The minimal Supergravity model (mSUGRA) has only five free parameters which determine the full supersymmetric mass spectrum. For a given value of $\lambda'$ the HERA sensitivity strongly depends on the squark mass. The exclusion limits presented here extend beyond the constraints obtained at the TeVatron collider or at LEP in part of the parameter space. For the first time mSUGRA limits for a non-vanishing $\lambda'_{11k}$ have been derived using data from $e^-p$ collisions.

To summarise, the results presented in this thesis represent the strongest limits on squark production from HERA so far. They are competitive and complementary to those derived from searches at LEP and TeVatron. However, the present schedule of HERA II envisages further operation until 2006/2007. An further increase of the centre of mass energy is not foreseen. Nevertheless, an considerable increase of statistics will lead to a further improvement of exclusion limits. In particular, with substantially more luminosity of $e^-p$ collisions the reach on $\lambda'_{11k}$ will be improved.

Furthermore, the other high energy colliders can look for squarks and supersymmetry in general in coming years. Since the LEP collaborations have analyzed basically all their data, in the near future the collaborations at the TeVatron will have the greatest potential to find the first hints of this promising theory. If still no sign of supersymmetry is found, searches up to much higher energies will be made at the Large Hadron Collider (LHC), which is currently being build at CERN. This machine will be able to collide protons with beam energies around 7 TeV. The energy available in the collisions between the constituents of the protons will reach the TeV range. Below this scale the masses of supersymmetric particles must be found to solve the hierarchy problem of the Standard Model. Thus, the search for supersymmetry will be a major topic at this collider.

For the precise measurements of the particle properties the clean environment of a lepton collider is needed. The next major project of experimental particle physics is expected to be the Next Linear Collider (NLC). At the moment three different proposals for machines of this kind are discussed. Among them, the TESLA project, planned at DESY, is most advanced.

Hence, the hunt for supersymmetry continues ...

# List of Figures

# List of Tables

# Bibliography


[1] S. L. Glashow, Nucl. Phys. 20 (1961) 579;
A. Salam, in Elemantary Particle Theory, ed. N.Svartholm (1968);
S. Weinberg, Phys. Rev. Lett. 19 (1967) 1264;
G. 't Hooft, M. Veltmann, Nucl. Phys. B44 (1972) 189.

[2] Y. Gol'fand and E. Likhtarn, JETP Lett. 13 (1971) 323;
D. Volkov and V. Akulov, Phys. Lett. B46 (1973) 109;
J. Wess and B. Zumino, Nucl. Phys. B70 (1974) 39;
For a review on supersymmetry see:
J. Wess and J. Bagger,
*Supersymmetry and Supergravity*,
Princeton Series in Physics.

[3] For reviews on the MSSM see:
H. P. Nilles, Phys. Rept. 110 (1984) 1;
H. E. Haber and G. L. Kane, Phys. Rept. 117 (1985) 75.

[4] E. J. Weinberg *et al.* [Particle Data Group],
*Review of particle physics*,
Phys. Rev. D66 (2002) 1 .

[5] Y. Fukada *et al.* [Super–Kamiokande Collaboration],
*Evidence for oscillation of atmospheric neutrinos*,
Phys. Rev. Lett. 81 (1998) 1562, [hep-ex/9807003].

[6] Q. R. Ahmad *et al.* [SNO Collaboration],
*Direct Evidence for Neutrino Flavor Transformation from Neutral-Current Interactions in the Sudbury Neutrino Observatory*,
Phys. Rev. Lett. 89 (2002) 011301, [nucl-ex/0204008].

[7] M. Hirsch *et al.*,
*Neutrino masses and mixings from supersymmetry with bilinear R-parity violation: A theory for solar and atmospheric neutrino oscillations*,
Phys. Rev. D62 (2000) 113008.

[8] J. Butterworth and H. Dreiner,
*R-Parity Violation at HERA*,
Nucl. Phys. B397 (1993) 3, [hep-ph/9211204], and references therein.

[9] H1 Collaboration,
*Searches for Squark Production in R-Parity Violating Supersymmetry at HERA,*
contributed paper, Abstract 101, Session 13, EPS 2003 (Aachen),
contributed paper, Abstract 182, LP 2003 (Fermilab).

[10] T. Ahmed *et al.* [H1 Collaboration],
*A Search for Leptoquarks and Squarks at HERA* ,
Z. Phys. C64 (1994) 545.

[11] C. Adloff *et al.* [H1 Collaboration],
*Searches at HERA for Squarks in R-Parity Violating Supersymmetry* ,
Eur. Phys. J. C20 (2001) 639, [hep-ex/0102050].

[12] R. N. Mohapatra, Phys. Rev. D34 (1986) 3457;
J. D. Vergados, Phys. Lett. B184 (1987) 55;
M. Hirsch, H. V. Klapdor-Kleingrothaus, S. G. Kovalenko, Phys. Lett. B352 (1995) 1, [hep-ph/9502315];
M. Hirsch, H. V. Klapdor-Kleingrothaus, S. G. Kovalenko, Phys. Rev. Lett. 75 (1995) 17;
M. Hirsch, H. V. Klapdor-Kleingrothaus, S. G. Kovalenko, Phys. Rev. D53 (1996) 1329, [hep-ph/9502385].

[13] P. Langacker,
*Parity violation in muonic atoms and cesium*,
Phys. Lett. B256 (1991) 277.

[14] H. Dreiner,
*An Introduction to Explicit R-Parity Violation*,
published in *Perspectives on Supersymmetry*,
Ed. G.L. Kane, World Scientific (1997) 462, [hep-ph/9707435].

[15] M. Acciarri *et al.* [L3 Collaboration],
*Search for R-parity Violating Decays of Supersymmetric Particles in e+e- Collisions at* $\sqrt{s}$*=189 GeV*,
Eur. Phys. J. C19 (2001) 397 , [hep-ex/0011087].

[16] B. Abbott *et al.* [D0 Collaboration],
*Search for R-parity Violating Supersymmetry in the Dielectron Channel*,
Phys. Rev. Lett. 83 (1999) 4476, [hep-ex/9907019].

[17] O. Nachtmann,
*Elemantarteilchenphysik, Phänomene und Konzepte*,
Vieweg, Braunschweig 1987.

[18] The LEP Working Group for Higgs Boson Searches,
*Search for the Standard Model Higgs Boson at LEP*,
submitted to Phys. Lett. B, CERN-EP/2003-011 (2003).

[19] R. P. Feynman,
*Very high-energy collisions of hadrons*,
Phys. Rev. Lett. 23 (1969) 1415.

[20] C. Callan and D. Gross,
*High-energy electroproduction and the constitution of the electric current*,
Phys. Rev. Lett. 22 (1969) 156.

[21] For reviews on GUT see:
G. G. Ross,
*Grand Unified Thoeries*,
Benjamin & Cummings, 1985.

[22] S. Weinberg, Phys. Rev. D13 (1976) 974;
L. Susskind, Phys. Rev. D20 (1979) 2619.

[23] U. Amaldi, W. de Boer, H. Fürstenau,
*Comparison of grand unified theories with electroweak and strong coupling constants measured at LEP*,
Phys. Lett. B260 (1991) 447.

[24] S. P. Martin,
*A supersymmetry primer*,
published in *Perspectives on Supersymmetry*,
Ed. G.L. Kane, World Scientific, (1997) 1., [hep-ph/9709356].

[25] S. R. Coleman and J. Mandula,
*All possible symmetries of the S Matrix*,
Phys. Rev. 159 (1967) 1251.

[26] P. Fayet,
*Supersymmetry and Weak, Electromagnetic and Strong Interactions*,
Phys. Lett. B64 (1976) 159.

[27] A. Bartl, H. Fraas, W. Majerotto, N. Oshimo,
*The Neutralino Mass Matrix in the Minimal Supersymmtric Model*,
Phys. Rev. D40 (1989) 1594.

[28] E. Perez,
*Recherche de Particules Supersymetriques dans l'experience H1*,
Dissertation, Paris, France (1996).

[29] S. Aid *et al.* [H1 Collaboration],
*A Search for Selectrons and Squarks at HERA*,
Phys. Lett. B380 (1996) 461, [hep-ex/9605002].

[30] J. Breitweg *et al.* [ZEUS Collaboration],
*Search for Selectron and Squark Production in e+p Collisions at HERA*,
Phys. Lett. B434 (1998) 214, [hep-ex/9806019].

[31] M. Dine, A. Nelson, Y. Shirman,
*Dynamical Supersymmetry Breaking Simplified*,
Phys. Rev. D51 (1995) 1362, [hep-ph/9408384].

[32] M. Drees and M. M. Nojiri, Nucl. Phys. B369 (1992) 54;
H. Baer and X. Tata, Phys. Rev. D47 (1993) 2739;
G. L. Kane, C. Kolda, L. Roszkowski, J. D. Wells, Phys. Rev. D49 (1994) 6173, [hep-ph/9312272].

[33] W. Buchmüller, R. Rückl, D. Wyler,
*Leptoquarks in lepton-quark collisions*,
Phys. Lett. B191 (1987) 442 and *Erratum* Phys. Lett. B448 (1999) 320.

[34] T. Plehn, H. Spiesberger, M. Spira, P. M. Zerwas,
*Formation and Decay of Scalar Leptoquarks/Squarks in ep collisions*,
Z. Phys. C74 (1997) 611, [hep-ph/9703433].

[35] G. A. Schuler and H. Spiesberger,
*DJANGO: the interface for the event generators HERACLES and LEPTO*,
in proceedings of the Workshop *Physics at HERA*, vol. 3, 1419, (1991).

[36] L. Lönnblad,
*ARIADNE version 4 – A program for simulation of QDC cascades implementing the colour dipole model*,
Comput. Phys. Commun. 71 (1992) 15.

[37] G. Gustafson and U. Pettersson,
Nucl. Phys. B306 (1988) 746;
*idem*, *addendum* Lund University preprint LU-TP-87-19, (October 1987) 4pp.;
B. Andersson, G. Gustafson, L. Lönnblad, U. Pettersson,
Z. Phys. C43 (1989) 625.

[38] H. Jung,
*Hard diffractive scattering in high energy ep collisions and the Monte Carlo Generator RAPGAP*,
Comput. Phys. Commun. 86 (1995) 147.

[39] V. N. Gribov and L. N. Lipatov, Sov. J. Nucl. Phys. 15 (1972) 438;
G. Altarelli and G. Parisi, Nucl. Phys. B126 (1977) 298;
Y. L. Dokshitzer, Sov. Phys. JETP 46 (1977) 641.

[40] H.-L. Lai *et al.*
*New Generation of Parton Distributions with Uncertainties from Global QCD Analysis*,
Eur. Phys. J. C12 (2000) 375, [hep-ph/0201195].

[41] T. Sjöstrand,
*PYTHIA 5.7 and JETSET 7.4 Physics and Manual*,
Lund Univ. preprint LU-TP-95-20 (1995) 321;
*idem*, CERN TH-7112 (1993), [hep-ph/9508391].

[42] T. Sjöstrand,
*High-energy-physics event generation with PYTHIA 5.7 and JETSET 7.4*,
Comput. Phys. Commun. 82 (1994) 74.

[43] M. Glück, E. Reya, A. Vogt,
*Photonic parton distributions*,
Phys. Rev. D46 (1992) 1973.

[44] U. Baur, J. A. Vermaseren, D. Zeppenfeld,
*Electroweak vector boson production in high-energy ep collisions*,
Nucl. Phys. B375 (1992) 3.

[45] K. Rosenbauer,
*Suche nach Leptoquarks und Leptogluonen im H1-Experiment bei HERA*,
Dissertation, RWTH Aachen, Germany (1995).

[46] S. Katsanevas and P. Morawitz,
*SUSYGEN 2.2 - A Monte Carlo Event Generator for MSSM Sparticle Production at e+ e- Colliders*,
Comput. Phys. Commun. 112 (1998) 227, [hep-ph/9711417].

[47] N. Ghodbane, S. Katsanevas, P. Morawitz, E. Perez,
*SUSYGEN 3, an Event Generator for Linear Colliders*,
[hep-ph/9909499].

[48] I. Abt *et al.* [H1 Collaboration],
*The H1 detector at HERA*,
Nucl. Instrum. Meth. A386 (1997) 310.

[49] B. Andrieu *et al.* [H1 Calorimeter Group],
*Beam tests and calibration of the H1 liquid argon calorimeter with electrons*,
Nucl. Instrum. Meth. A350 (1994) 57;
B. Andrieu *et al.* [H1 Calorimeter Group],
*Results from pion calibration runs for the H1 liquid argon calorimeter and comparisons with simulations*,
Nucl. Instrum. Meth. A336 (1993) 499.

[50] R. Brun and F. Carminati,
*GEANT Detector description and Simulation Tool*,
Cern Programm Library W5013 (1993).

[51] E. Chabert, C. Diaconu, S. Kermiche, I. Negri, C. Vallee,
*QBGFMAR, An updated PHAN package for cosmic and halo muon topological rejection in high $P_T$ physics analysis*,
H1 note, H1-IN/98-556.

[52] P. Bruel,
*Recherches d'interactions au-dela du Modele Standard a HERA*,
Dissertation, Orsay, France (1998).

[53] C. Adloff *et al.* [H1 Collaboration],
*Measurement of Neutral and Charged Current Cross-Sections in Positron-Proton Collisions at Large Momentum Transfer* ,
Eur. Phys. J. C13 (2000) 609, [hep-ex/9908059].

[54] C. Adloff *et al.* [H1 Collaboration],
*Measurement and QCD Analysis of Neutral and Charged Current Cross Sections at HERA*,
DESY-03-038, submitted to Eur. Phys. J. C (2003), [hep-ex/0304003].

[55] B. Heinemann,
*Measurement of Charged Current and Neutral Current Cross Sections in Positron-Proton Collisions at* $\sqrt{s} = 300\,\mathrm{GeV}$,
Dissertation, Hamburg, Germany (1999).

[56] B. Andrieu *et al.* [H1 Calorimeter Group],
*The H1 liquid argon calorimeter system*,
Nucl. Instrum. Meth. A336 (1993) 460.

[57] C. Adloff *et al.* [H1 Collaboration],
*Measurement of Charged and Neutral Current Cross Sections in Electron-Proton Collisions at high* $Q^2$,
Eur. Phys. J. C19 (2001) 269, [hep-ex/0012052].

[58] S. Bentvelsen *et al.*,
*Reconstruction of* $(x, Q^2)$ *and extraction of structure functions in neutral current scattering at HERA*,
in proceedings of the Workshop *Physics at HERA*, vol. 1, (1991) 23.

[59] U. Bassler and G. Bernardi,
*Some properties of the very high* $Q^2$ *events of HERA*,
Z. Phys. C76 (1997) 223.

[60] L. West,
*How to use the Heavy Flavour Working Group Track, Muon and Electron Selection Code*,
`https://www-h1.desy.de/icas/imanuals/h1phan/track_manual30106.ps`.

[61] A. Schwank,
*Effizienzbestimmung von Detektorkomponenten des H1-Experiments mit Hilfe kosmischer Strahlung*,
Diploma Thesis, Hamburg, Germany (1998).

[62] B. Leissner,
*Muon Pair Production in Electron-Proton Collisions*,
Dissertation, RWTH Aachen, Germany (2002).

[63] J. Marks,
*HFS - a software package to cope with the Hadronic Final State*,
`https://www-h1.desy.de/iwork/iescale/hfs/hfs.html` (2001).

[64] F. Abe*et al.* [CDF Collaboration],
*Topology of three-jet events in $p\bar{p}$ collisions at $\sqrt{s} = 1.8\,TeV$*,
Phys. Rev. D45 (1992) 1448.

[65] R. Akers *et al.* [OPAL Collaboration],
*QCD Studies Using a Cone-based Jet Finding Algorithm for e+e- Collisions at LEP*,
Zeit. f. Phys. C63 (1994) 197.

[66] M. H. Seymour,
*Searches for new particles using cone and cluster jet algorithms: a comparative study*,
Z. Phys. C62 (1994) 127.

[67] J. Marks and M. Ellerbrock,
*private communication*,
Hamburg, 2003.

[68] C. Adloff *et al.* [H1 Collaboration],
*A Search for Leptoquark Bosons in $e^-p$ Collisions at HERA*,
Phys. Lett. B523 (2001) 234, [hep-ex/0107038].

[69] C. Adloff *et al.* [H1 Collaboration],
*A Search for Excited Fermions at HERA*,
Eur. Phys. J. C17 (2000) 567, [hep-ex/0007035].

[70] C. Adloff *et al.* [H1 Collaboration],
*Search for new Physics in $e^{\pm}q$ contact interactions at HERA*,
DESY-03-052, accepted by Phys. Lett. B (2003), [hep-ex/0305015].

[71] A. Blondel and F. Jacquet,
Proceedings of the *Study of an ep Facility in Europe*,
DESY 79/48 (1979) 391.

[72] C. Adloff *et al.* [H1 Collaboration],
*Measurement of inclusive jet cross sections in photoproduction at HERA*,
accepted by Eur. Phys. J. [hep-ex/0302034].

[73] A. Aktas *et al.* [H1 Collaboration],
*Search for Single Top Quark Production in ep Collisions at HERA*,
to be submitted to Phys. Lett. B (2003).

[74] A. Pukhov, E. Boos, M. Dubinin, V. Edneral, V. Ilyin, D. Kovalenko, A. Kryukov, V. Savrin, S. Shichanin, A. Semenov,
*CompHEP - a package for evaluation of Feynman diagrams and integration over multi-particle phase space – User's manual for version 33.*
Preprint INP MSU 98-41/542, [hep-ph/9908288].

[75] A. L. Read
*Optimal Statistical Analysis of Search Results based on the Likelihood Ratio and its Application to the Search for the MSM Higgs Boson at $\sqrt{s} = 161$ and 172 GeV*,
DELPHI 97-158 PHYS 737, 1997.

[76] T. Junk,
*Confidence Level Computation for Combining Searches with Small Statistics*,
Nucl. Instrum. Meth. A434 (1999) 435.

[77] A. G. Frodesen, O. Skeggestad, H. Tøfte,
*Probability and Statistics in Particle Physics*,
Universitetsforlaget (1979).

[78] W. T. Eadie, D. Dryard, F. E. James, M. Roos, B. Sadoulet,
*Statistical Methods in Experimental Physics*,
North-Holland, (1971).

[79] M. G. Kendall, A. Stuart,
*The Advanced Theory of Statistics*,
Charles Griffen & Company Limited, London (1967).

[80] SUSPECT 2.1, code written by A. Djouadi, J.L. Kneur and G. Moultaka.

[81] J. Abdallah *et al.* [DELPHI Collaboration],
*Final results from DELPHI on the searches for SM and MSSM Neutral Higgs bosons*,
Submitted to Eur. Phys. J. C (2003).

# Acknowledgement

At this point I want to express my sincere gratitude to all those I was working with and I could profit from during the past three years. My special thanks go to:

- My supervisor Prof. Peter Schleper for his excellent support. His experience, guidance and enthusiasm in many discussions was very motivating for me. I appreciate his commitment and interest in my work.
- Prof. Karlheinz Meier for his willingness to act as second referee of this thesis.
- Prof. Franz Eisele for offering me the opportunity to work as a Ph.D. student at the H1 experiment.
- Emmanuelle Perez for all the help and many discussions we had about details of the analysis and supersymmetry in general.
- Stefan Schmitt. This analysis benefited a lot from his help concerning all aspects of particle physics.
- My colleagues of the H1 collaboration. I enjoyed the friendly and professional atmosphere. The last years have been a great experience for me. In particular I would like to say thank you to Eram Rizvi, Jörg Gayler and Andre Schöning. The style of this thesis benefited a lot from the help of Nick Malden concerning English grammar. My special thanks go to Linus Lindfeld, Lars Finke and Christian Schwanenberger for the friendship that I appreciate a lot.
- The H1 group Heidelberg for their good team work, especially Jörg Marks, Jochen Dingfelder, Frank-Peter Schilling and Malte Ellerbrock.
- Jan Becker, Carlo Duprel, Carsten Schmitz and Max Urban for making the time at DESY that pleasant and amazing.
- Ansgar Reiners for the careful reading of the manuscript and for our friendship.
- Daniela for the beautiful times that we have had and those which are yet to come.
- My family, in particular my parents for all the support they gave me and for always being there for me.

Vielen Dank!